

GROWTH AND CHARACTERIZATION OF GROUP III-  
NITRIDES BY MIGRATION-ENHANCED AFTERGLOW  
EPITAXY

by

Rositsa Gergova

Department of Chemistry, Lakehead University,

Thunder Bay, Ontario

May-2014

A dissertation submitted to the Faculty of Science and  
Environmental Studies in partial fulfillment of the requirements of  
the degree of Doctor of Philosophy

©2014, Rositsa Gergova

Growth and characterization of group III-nitrides by migration enhanced afterglow epitaxy

Rositsa Gergova

Thesis supervisors: Dr. Dimiter Alexandrov, Dr. Alla Reznik

ABSTRACT

The work presented in this thesis investigates the growth and properties of group III-nitride semiconductors that were grown using the Migration Enhanced Afterglow Epitaxy (MEAgrow) method. This work was to enhance the understanding of the MEAgrow growth process towards the improvement of quality of the layers grown using this technique. The MEAgrow technique applies the migration enhanced epitaxy method in a low pressure plasma-based CVD reactor, which has a potential of producing high quality epitaxial group III-nitride layers at relatively low growth temperatures on large deposition areas.

The low temperature pulse growth in metal-rich regime, comprising the MME method was employed under growth pressures between 500 mTorr and 3000 mTorr. As the MME method up to this point has been used only for MBE systems, study of the impact of the growth pressure on the materials properties was necessary. In this work the pressure dependence was mapped to an existing surface phase diagram for MBE systems by calculating the number of nitrogen gas phase collisions and the metalorganic bombardment rate, for the specific to the prototype reactor parameters, to a first approximation. This was done in order to achieve an intermediate regime free of metal droplets for growth in metal-rich regime.

High quality epitaxial InN layers were accomplished on extremely thin and smooth Ga<sub>2</sub>O<sub>3</sub> buffer layers. These results indicate a potential for the application of Ga<sub>2</sub>O<sub>3</sub> buffers in InN growth. The MEAgrow InN layers were further optimized for growth on commercially available GaN buffer layers and excellent two-dimensional growth was achieved for layers grown under metal-rich conditions at 512 °C. Post-growth annealing studies were carried out for InN layers grown at temperatures below 400 °C to study the limiting processes of the removal of excess nitrogen, believed to be a dominant defect in InN films grown in plasma-based systems at very low temperatures.

Variations in GaN stoichiometry under certain growth conditions and the effect of similar growth conditions on MEAgrow grown InGaN were also examined. The growth of MEAgrow InGaN samples on sapphire substrates was optimized to reduce the indium surface segregation and phase separation of the material.

## TABLE OF CONTENTS

ABSTRACT.....	I
LIST OF FIGURES .....	VI
LIST OF TABLES .....	XI
LIST OF APPENDIX TABLES AND FIGURES.....	XII
ACKNOWLEDGMENTS .....	XIII
CHAPTER 1. INTRODUCTION .....	1
1.1 Group III-nitrides materials system and applications .....	1
1.2 Thesis objectives.....	6
1.3 Thesis outline .....	6
CHAPTER 2. OVERVIEW OF THE MAIN GROWTH TECHNIQUES AND THE MEAGLOW TECHNOLOGY .....	7
2.1 Growth techniques used for group III-nitrides.....	7
2.1.1 MOCVD.....	8
2.1.2 MBE .....	9
2.1.3 HVPE .....	11
2.1.4 ALD .....	11
2.2 Description of the MEAglow growth technique.....	12
2.2.1 Method .....	12
2.2.1.1 MEE .....	13

2.2.1.2	MME.....	13
2.2.2	The MEAglow System.....	14
CHAPTER 3. CHARACTERIZATION METHODS.....		20
3.1	X-ray Photoelectron Spectroscopy (XPS) .....	20
3.2	Secondary Ion Mass Spectroscopy (SIMS) .....	21
3.3	X-ray Diffraction (XRD) .....	22
3.4	Optical transmission spectroscopy.....	24
3.5	Atomic Force Microscopy (AFM) .....	26
3.6	Scanning Electron Microscopy (SEM).....	27
3.7	Hall Effect.....	29
CHAPTER 4. MEAGLOW GROWN GAN.....		31
4.1	Preliminary experiments .....	31
4.1.1	Growth conditions.....	31
4.1.2	Results and analysis .....	33
4.2	The effect of chamber pressure on the growth of GaN.....	47
4.2.1	Growth conditions.....	48
4.2.2	Analysis.....	49
4.3	Study of the growth rate limiting processes for MME MEAglow grown GaN.....	62

4.4	Improvement of GaN MEAglow polycrystalline films after annealing .....	66
CHAPTER 5. GROWTH OF INN BY MEAGLOW .....		70
5.1	Introduction.....	70
5.2	InN grown by MEAglow .....	70
5.2.1	Substrate preparation and growth conditions.....	71
5.2.2	InN grown on Ga <sub>2</sub> O <sub>3</sub> buffer layer .....	73
5.2.3	InN grown on MOCVD GaN templates and sapphire substrates .....	79
5.3	Post-growth annealing studies on MEAglow grown nitrogen rich InN .....	84
CHAPTER 6. GROWTH OF INGAN BY MEAGLOW.....		98
6.1	Growth in metal rich regime.....	99
6.2	The effect of metal pulse length.....	106
6.3	The effect of growth temperature .....	111
6.4	InGaN grown on GaN buffer layers as compared to the growth of InN on GaN under similar conditions.....	120
CHAPTER 7. CONCLUSION.....		123
APPENDIX A XPS FITTING PROCEDURE AND RESULTS .....		126
REFERENCES.....		130

## LIST OF FIGURES

Figure 2.1 The MEAglow growth system.....	15
Figure 2.2 Scheme of the MEAglow hollow-cathode plasma source, as it was presented in [69] by Butcher et al. ....	16
Figure 3.1 Illustration of x-ray diffraction from crystal planes according to Bragg's law.	23
Figure 3.2 The Hitachi SU-70 SEM as shown in the Hitachi commercial brochure.....	28
Figure 3.3 InN cross-sectional high resolution image taken with the Hitachi SU-70 SEM. .....	29
Figure 4.1 Optical transmission spectra for Sample 1 and Run 1 of Sample 3. ....	34
Figure 4.2 Optical absorption for Sample 1 and Run 1 of Sample 3.....	34
Figure 4.3 Optical absorption spectrum for Sample 2, for which no linear part of the spectrum was found to extrapolate with the x-axis.....	35
Figure 4.4 Optical transmission spectra for a) the three growth runs of Sample 3, b) stoichiometric commercial GaN template .....	36
Figure 4.5 High resolution XPS spectra of Carbon 1s for a) Sample 3 and b) Sample 4..	40
Figure 4.6 High resolution XPS spectrum of N1s for Sample 3.....	42
Figure 4.7 High resolution XPS spectrum of N1s for Sample 4.....	42
Figure 4.8 High resolution XPS spectrum of N 1s for Sample 5B.....	44
Figure 4.9 SIMS data for an early sample having high concentration of background impurities (Sample A).....	45
Figure 4.10 SIMS data for more stoichiometric MEAglow GaN layer (Sample B).....	46
Figure 4.11 a) An early-grown MEAglow sample, b) stoichiometric MEAglow sample.	46
Figure 4.12 Surface phase diagram for MME growth in MBE systems - Phys. Status Solidi C 6, S788 (2009). ....	48

Figure 4.13 Dependence of the GaN layer deposition per cycle on the number of nitrogen gas collisions, with the derived three growth regimes.....	51
Figure 4.14 RMS surface roughness dependency on pressure. The data points are connected with line just for better following of the trend. The connecting lines are drawn only to show the trend.....	53
Figure 4.15 AFM surface images for the samples grown under 1.2, 1.7, 1.8, and 1.9 Torr. The RMS surface roughness corresponding to the sample grown at particular chamber pressure, is shown below each image. ....	54
Figure 4.16 AFM surface images of the samples grown under 2.0, 2.1, 2.2, and 2.8 Torr. The RMS corresponding to the sample grown at particular chamber pressure, is shown below each image. ....	55
Figure 4.17 TMG bombardment rate dependence of pressure. ....	56
Figure 4.18 GaN grown under a) 2.8 Torr chamber pressure and b) 1.2 Torr chamber pressure .....	57
Figure 4.19 The non-uniformity of the GaN layer grown at 2.8 Torr is evident from the optical transmission spectrum.....	58
Figure 4.20 X-ray diffraction spectra of the studied samples.....	59
Figure 4.21 The Energy bandgaps of the GaN samples grown at various chamber pressures versus the c lattice constant.....	61
Figure 4.22 The dependence of c lattice constant versus the absorption edge for Ga-rich MEAgrow GaN.....	62
Figure 4.23 The determined duty cycle for growth in the intermediate regime showing increased growth rate.....	66

Figure 4.24 a) A comparison between the X-ray diffraction spectra after each annealing procedure, and b) comparison between the optical absorption spectra. ....	68
Figure 5.1 AFM surface images of: a) the surface of the InN layer grown on top of Ga <sub>2</sub> O <sub>3</sub> . The RMS surface roughness is 4.7 nm; b) the surface of the Ga <sub>2</sub> O <sub>3</sub> layer. The RMS surface roughness is 0.5 nm. ....	74
Figure 5.2 SEM micrographs of InN grown on top of the thin Ga <sub>2</sub> O <sub>3</sub> buffer layer, showing: a) surface image, and b) cross-section of the 170 nm thick InN layer grown on the Ga <sub>2</sub> O <sub>3</sub> buffer layer. ....	75
Figure 5.3 X-ray diffraction $\omega$ -2 $\theta$ scan for InN grown on the Ga <sub>2</sub> O <sub>3</sub> layer, showing no evidence of In metal peak at 33.1 °. ....	75
Figure 5.4 a) Optical absorption and b) Optical transmission spectra for InN/Ga <sub>2</sub> O <sub>3</sub> . ....	77
Figure 5.5 Optical absorption spectrum of the thin Ga <sub>2</sub> O <sub>3</sub> buffer layer showing a sharp absorption edge at 5.59 eV. ....	78
Figure 5.6 SEM surface image of InN grown on top of 20 nm rough Ga <sub>2</sub> O <sub>3</sub> thin layer. ..	79
Figure 5.7 SEM micrographs of a) InN grown on a MOCVD GaN template, and b) the sister sample, grown directly on sapphire substrate. ....	81
Figure 5.8 X-ray diffraction for the InN layer grown on GaN template and its sister sample grown on sapphire, corresponding to the samples presented on Figure 5.7. ..	81
Figure 5.9 Optical absorption spectra for InN films produced by MEAgrow under similar growth conditions. A comparison is made among the layers grown on different substrates. ....	82
Figure 5.10 SEM surface image showing excellent 2D growth of an InN layer, produced by MEAgrow on commercial GaN template after optimized growth conditions. ....	83

Figure 5.11 Activation energies calculated for indium rich growth conditions for zincblende polytype of InN. The picture is as shown in reference [117] from Stampfl et. al.....	86
Figure 5.12 The formation energies for native defects for wurtzite polytype of InN under nitrogen rich and indium rich conditions, as presented in reference [118] from Duan and Stampfl.....	87
Figure 5.13 The growth temperature dependence on the nitrogen to indium ratio of RPECVD grown InN as it was presented in reference [121] by Butcher et al. ....	89
Figure 5.14 XRD spectra for the 4 annealed samples grown at temperatures between 300 °C and 400 °C. ....	92
Figure 5.15 Optical absorption spectra for the four annealed samples grown between 300 °C and 400 °C. ....	93
Figure 5.16 SEM cross-sectional image of the sample grown at 290 °C. The columnar structure is evident from the micrograph, showing small grain size less than 200 nm. ....	95
Figure 6.1 XRD of samples grown with (samples 2 and 3) and without (Sample 1) metalorganic flushing step. ....	103
Figure 6.2 Optical absorption of Sample 1 showing two linear regions of the optical density squared. ....	104
Figure 6.3 Optical absorption spectrum of Sample 2. ....	105
Figure 6.4 Comparison between $\omega$ -2 $\theta$ and grazing incidence scan of Sample 3.....	106
Figure 6.5 Optical absorption edge of Sample 3.....	106

Figure 6.6 a) XRD spectra showing the variable composition with varying the time for the metalorganic pulse, and b) XRD of the sister sample of Sample C grown on GaN, showing a single InGaN peak at $34^\circ$ and a GaN substrate peak at $34.6^\circ$ . .....	107
Figure 6.7 TEM cross-sectional image of a 100 nm thick InGaN grown on sapphire ....	109
Figure 6.8 a) The variation of the optical bandgap with the MO pulse length, and b) optical transmission for Sample D.....	111
Figure 6.9 X-ray diffraction of InGaN grown at $405^\circ\text{C}$ on sapphire.....	113
Figure 6.10 Temperature dependence of the InGaN composition as a function of the absorption edge for MEAglow InGaN.....	114
Figure 6.11 Variation of the FWHM with the composition for samples grown at $405^\circ\text{C}$ . .....	114
Figure 6.12 Absorption edge for MEAglow GaN sample containing high level of background carbon impurities (Sample A, Chapter 4), compared to stoichiometric MEAglow GaN (Sample B, Chapter 4). .....	117
Figure 6.13 The variation of the carrier concentration for samples grown at $405$ and $540^\circ\text{C}$ with composition. ....	120
Figure 6.14 Surfaces of a) InN grown metal rich at $540^\circ\text{C}$ , and b) InGaN grown under similar conditions.....	121
Figure 6.15 Cross-sectional images of a) metal rich InN grown on sapphire and b) InGaN grown on sapphire under similar conditions at $540^\circ\text{C}$ .....	122

## LIST OF TABLES

Table 1.1 Some fundamental properties of wurtzite GaN, InN, and AlN .....	3
Table 4.1 Variable growth parameters.....	32
Table 4.2 Thickness and energy bandgap comparison from the optical absorption spectra for samples 1-3. The performed measurements after each 45x4 cycles for the three runs of Sample 3 are denoted as 3a, 3b, and 3c. ....	35
Table 4.3 Growth parameters for the two additional samples grown under less Ga-rich conditions.....	38
Table 4.4 Growth Conditions.....	49
Table 4.5 Energy Bandgap obtained by optical transmission.....	60
Table 4.6 Variable growth conditions.....	63
Table 4.7 Properties of the GaN layers grown under the conditions listed in Table 4.6 ...	64
Table 5.1 Growth conditions for Samples A, B, C, and D .....	88
Table 5.2 Results from InN post-growth annealing.....	94
Table 5.3 Properties of the annealed samples. ....	96
Table 6.1 Hall Effect data for Samples A, B, C, and D.....	110

## LIST OF APPENDIX TABLES AND FIGURES

Table A.1 Relative atomic percentages for the main elements present on the surface of the studied samples.....	126
Figure A.1 High resolution XPS spectrum of C 1s core level for Sample 5A.....	127
Figure A.2 High resolution XPS spectrum of C 1s core level for Sample 5B.....	127
Figure A.3 High resolution XPS spectrum of C 1s core level for Sample 6.....	127
Figure A.4 High resolution XPS spectrum of C 1s core level for Sample 3.....	127
Figure A.5 High resolution XPS spectrum of C 1s core level for Sample 4.....	128
Figure A.6 High resolution XPS spectrum of N 1s core level for Sample 4.....	128
Figure A.7 High resolution XPS spectrum of N 1s core level for Sample 5A.....	128
Figure A.8 High resolution XPS spectrum of N 1s core level for Sample 5B.....	128
Figure A.9 High resolution XPS spectrum of C 1s core level for Sample 3.....	129
Figure A.10 High resolution XPS spectrum of C 1s core level for Sample 6.....	129

## ACKNOWLEDGMENTS

I would like to thank Dr. Scott Butcher who supervised me for almost three years for his guidance and discussions, for his great patience and continuous support. I would like to express my gratitude to Dr. Butcher for sharing his knowledge and experience, and for his encouragement. I really enjoyed the work with Dr. Butcher and the time spent in lab.

I also greatly acknowledge the support of my supervisors Dr. Dimiter Alexandrov, Dr. Alla Reznik, and Dr. Oleg Rublel throughout my studies during the past three years.

I deeply appreciate the academic help and moral support of Dr. Penka Terziyska.

The doctoral candidate would like to thank for the methodological scientific directions that she received during the courses of the following projects: LU – Meaglow Ltd. project having principal investigator Dr. D. Alexandrov, and Dr. D. Alexandrov’s NSERC project “Excitons of the structure and their applications in design of novel electronic devices”

I would like to express my gratitude to Lakehead University for providing me with the Ontario Graduate Scholarship. The completion of my thesis would be impossible without this support.

I would like to acknowledge the support of MEAglow ltd. who provided considerable financial and technical support to the university.

I thank my friend Jas who was always there to support me and encourage me.

Finally, I would like to say thank you to my husband Anton and my parents for always being there for me.

## Chapter 1. INTRODUCTION

### 1.1 Group III-nitrides materials system and applications

The group III-nitride materials system has attracted remarkable interest for their potential application in various electronic and optoelectronic devices. The binary compounds InN, GaN, and AlN form continuous ternary alloy systems, having a direct bandgap throughout the entire alloy composition. The main advantage of this material system is that it covers a wide range of energy bandgaps from near infrared to deep UV, spanning from 6.2 eV for AlN [1] to 3.4 eV for GaN [2] and potentially 0.7 eV [3] – 2.5 eV for InN which makes these materials potential candidates for solar cells [4-7], UV detectors [8], and light-emitting diodes [9,10]. Other advantages of group III-nitrides represent their outstanding electrical properties, their resistance to high radiation, and their high melting temperatures. The materials exhibit large breakdown fields which makes them useful for high-power and high-frequency device applications [11,12], while the relatively high thermal conductivities allow the devices to be easily cooled [13]. The large bond strength of AlN and GaN makes these materials stable at high temperatures, which allows device operation at high temperatures. The group III-nitrides has a potential for space applications as the large bandgap and bond strength make them resilient to radiation damage [4,14]. These materials also find application in short-wavelength laser diodes, green light-emitting diodes, high-density data storage and full-colour displays [15].

Group III-nitrides can crystallize in wurtzite, zincblende and rock salt structure with the wurtzite being the most thermodynamically stable polytype under ambient conditions.

The zincblende structure is metastable and can form by growth on cubic substrates, and the rock salt structure can be formed only under very high pressures [16]. The difference between the wurtzite and the zincblende structures is in the stacking sequence of the nitrogen and metal atoms ABAB along (0001) direction for the wurtzite structure, whereas the stacking order for the zincblende structure is ABCABC along (001) direction. The wurtzite crystal structure lacks inversion plane normal to the c-axis which results in a spontaneous polarization of the material. The polarity of the crystal is determined from the bond direction. The convention is when bonds point from N-plane to the Ga (In, Al)-plane it marks the positive (0001) direction and the material is said to be Ga (In, Al)-polar. For N-polar material the opposite direction is taken. The growth of Ga (In, Al)-polar and N-polar GaN has been extensively studied as the growth kinetics for the different polarities is different [17] and therefore it affects the bulk and surface properties of the material [18].

Some of the important material properties that allow this material system the large range of device applications are presented in Table 1.1

Although, group III-nitrides has a large number of potential applications, there exist technological issues with regards to the growth of the binary compounds, as well as the growth of their ternary alloys that hinder the development of these materials.

Table 1.1 Some fundamental properties of wurtzite GaN, InN, and AlN

Parameter	InN	GaN	AlN
Energy Bandgap, (eV)	0.6-0.65 [19], 0.7 [3], 0.9 [20], 1.1[21], 1.4 [22], 1.9-2.5 [23]	3.4 [28]	6.2 [1]
Lattice constant a (Å)	3.538 [24]	3.189 [25]	3.110 [30]
Lattice constant c (Å)	5.703 [24]	5.185 [25]	4.98 [30]
Thermal conductivity (W/cm K)	0.45 [25]	2.0-2.1 [25]	2.85 [25]
Dielectric constant, $\epsilon$	8.4 [26]	5.3 [25]	4.77 [25]
Mobility	3500 [27]	900 [29]	--

One of the challenges for the epitaxial growth of group III-nitride material system is that currently no native substrates exist for these materials. Therefore, device performance is significantly limited by the structural quality, resulting from the heteroepitaxy. The lattice mismatch, the difference in the thermal expansion coefficient, and differences in the chemical stability between the substrate and the epilayers lead to high level of dislocation densities, induced biaxial strain, mosaicity, or wafer bowing. To reduce the structural defects and maintain a reasonable material quality, normally the use of expensive and time-consuming buffer layers is required.

Gallium nitride is certainly the most extensively studied material from this class of binary compounds followed by AlN. However, further investigations are still needed to reach the understanding level for other well-developed semiconductors like GaAs or Si. The GaN layers suffer from large background electron concentrations caused by native defects

and impurities. This makes the p-type doping for GaN very difficult. In addition, the chemical stability of the material presents a technological challenge for wet etching.

The successful development of GaN and the achieved p-type doping led to the demonstration of excellent p-n junction LEDs, so the first improvement of the group III-nitrides was towards the development of blue LEDs [31]. A breakthrough in the LED technology came in 1994 with the announcement of commercial blue LED [32], which was followed by the demonstration of bright blue/green LEDs in 1996 [33]. This became possible with the improvement of the GaN crystal quality by employing low-temperature GaN buffer layers, instead of the previously used AlN buffers, for the first time by Nakamura [34] in 1991. After these events, drastic progress was made in the research of GaN and related materials.

Considerable effort has been invested for InGaN development as it is used as an active layer in LEDs and is responsible for the emission in the near UV, violet, blue, and green colours of the spectrum. The technology for the growth of InGaN layers with high gallium content is well established. Usually, thin InGaN layers are grown completely strained on thick GaN buffer layers. The GaN buffer layers are normally about 4  $\mu\text{m}$  thick, so that the dislocations induced by the lattice mismatch with the underlying substrate are annihilated. Even in this case, these GaN buffer layers have high dislocation densities of about  $10^9 / \text{cm}^3$ . Despite the high dislocation densities in these materials, the GaN-based LED structures using InGaN active layers experience high efficiencies due to carrier localization [15].

The growth of high quality indium-rich InGaN further represents a challenge and this impedes the development of solar cells and longer-wavelength LEDs . One of the reasons is the indium incorporation in InGaN which requires growth at relatively low temperatures. The growth of good quality GaN and gallium rich InGaN occurs at high temperatures with the conventional growth techniques used for commercial production. However, the dissociation temperature for InN is lower because In-N bonds are weaker than the Ga-N bonds and low growth temperatures are needed for indium to incorporate efficiently in the alloy [35-37]. Furthermore, the difference in the formation enthalpies of InN and GaN leads to indium surface segregation at the growth front. Another problem is the large difference in the interatomic spacing of InN and GaN which leads to a solid phase miscibility gap [38, 39]. In addition, p-type conductivity for In-rich InGaN and InN is harder to achieve than for GaN due to the larger background electron concentration and the electron surface accumulation layer characteristic for InN [40].

InN is the least understood material from the group III-nitride materials system. It has been extensively studied in the past decade to aid in the development of the InGaN ternary. The fundamental properties of InN are still not well understood. For instance, the value of the energy bandgap is a subject of debate [41]. InN films grown by different growth techniques often experience different properties which leads to controversy for reported values of electron effective mass, native defects, decomposition temperatures, which further complicates the interpretation. InN is theoretically predicted to have superior electrical properties than GaAs, which makes it a possible candidate for high-speed and high-power FETs [42]. The material has been recently investigated for realization of terahertz devices [43-45].

## 1.2 Thesis objectives

The aims of this work were to improve the quality and achieve atomically smooth surfaces of GaN, InGaN and InN, grown at temperatures compatible with the growth temperature of InN. This would allow the growth on inexpensive thermally fragile substrates, as well as heterostructures growth of GaN on top of InN, without compromising with the quality of the layers. The crystal growth was performed by a novel method called Migration-Enhanced Afterglow Epitaxy (MEAglow) which is designed to improve crystal quality at low temperatures and also allows deposition on large areas. The advantages of this growth technique are discussed in detail in Chapter 2. Since MEAglow is a new and relatively immature growth method, this work was also to study how some of the growth parameters affect the film properties.

## 1.3 Thesis outline

This thesis is organized in total of seven chapters. The following Chapter 2 discusses briefly the conventional growth techniques used for the production of group III-nitride semiconductors and describes in detail the new migration-enhanced afterglow method used for the present research. The characterization methods used for the studied materials are described in Chapter 3. Chapter 4 is focused on the growth of GaN films by MEAglow and their characterization. In Chapter 5 MEAglow growth of InN is presented. Chapter 6 studies the optimization of the growth process towards the achievement of better indium incorporation and crystal quality of MEAglow InGaN layers, and Chapter 7 provides some conclusion remarks for the present work.

## Chapter 2. Overview of the main growth techniques and the MEAglow technology

Group III-nitrides have been synthesized by various growth techniques.

The most common are Metalorganic Chemical Vapor Deposition (MOCVD), Molecular Beam Epitaxy (MBE), Hydride Vapor Phase Epitaxy (HVPE), RF sputtering, and Atomic Layer Deposition (ALD). All these techniques have their advantages in particular aspects and also their drawbacks which reflect on the physical properties of the semiconductors. For example, MOCVD is the leading commercial technology for growth of high quality GaN layers but is not preferable for the growth of InN and InGaN with high indium content, owing to the high temperatures employed.

In a broad classification, the vapor phase growth techniques can be divided into Physical Vapor Deposition (PVD) and Chemical Vapor Deposition (CVD). The PVD methods are classified into evaporation and sputtering methods such as: MBE, Pulsed Laser Deposition (PLD), thermal evaporation. Some of the CVD methods are MOCVD or also called MOVPE (Metalorganic Vapor Phase Epitaxy) and HVPE.

A brief description of the most employed conventional growth techniques used for the production of group III- nitride material is provided in Section 2.1 of this chapter, in order to emphasize on the advantages, as well as some of the current technological issues in growth of III-nitrides related to these methods. Section 2.2 presents in more detail the MEAglow growth technique which was used for the work presented in this thesis.

### 2.1 Growth techniques used for group III-nitrides

### 2.1.1 MOCVD

The metalorganic chemical vapor deposition technique is the most successful in producing high quality GaN for applications in optoelectronic devices, such as LEDs [46], laser diodes (LD) [47], and transistors [48]. Much of the color spectrum for LEDs can be produced by the MOCVD technique by combining green and blue nitride LEDs with phosphide LEDs, which has made the technique dominant for device manufacturing. The technique offers good control of alloy composition of <25% InN or AlN mole fraction and GaN layer properties. However, the growth of alloys with mole fractions closer to InN or AlN still represents a challenge [49].

The conventional MOCVD method relies on the vapor transport of metal alkyl and ammonia precursors to a heated substrate. The growth takes place at high temperatures because of the cracking efficiency of the ammonia which is best decomposed at temperatures above 1000 °C [50]. In MOCVD reactors the metalorganic vapors are being transported from the bubblers by carrier gas to the heated substrate, where the reaction takes place. The growth process is controlled by precisely controlling the important growth parameters, for instance, the temperature and the mass flow rates. The vapor pressure of the metalorganic precursors is controlled by the temperature of the bubblers.

Very high quality GaN have been achieved by MOCVD at temperatures above 1050 °C using GaN or AlN buffer layers on top of the sapphire substrates [34,51]. Various designs of MOCVD reactors are available for group III-nitrides growth. For instance, the very high quality GaN layers reported in [34] were produced by two-flow MOCVD reactor developed by Nakamura et al. [52]. The reactant gas for this system was directed parallel to the substrate, while a second gas flow was directed perpendicularly to the substrate in

order to change the direction of the reactant gas. This type of reactor design helped improve the crystal quality of the films as well as increased the growth rates in comparison to the conventional MOCVD systems [52].

A big disadvantage of the MOCVD system is the high temperatures required for group III-nitrides growth. The use of high growth temperatures reflects on the abruptness of the heterointerfaces, which directly affects the transport properties of the material [53]. The growth of InN and indium-rich InGaN requires low growth temperatures due to the low dissociation temperature of InN ( $\sim 550$  °C) but MOCVD growth at these temperatures becomes limited by the low decomposition rate of ammonia [54]. Furthermore, high temperatures employed in the MOCVD growth of InN layers create uniformity problems when grown on large areas, and a typical solution of this problem can be the use of planetary reactors. In these reactors multiple substrates are arranged on top of a common round susceptor. The advantages of this type of MOCVD reactors are given in [56].

Another common problem related to the MOCVD growth is that it involves use of hazardous materials ammonia, hydrogen, silane (used for silicon doping, though it is often diluted in hydrogen to about 2% now to make it less dangerous).

### 2.1.2 MBE

MBE is the most sophisticated PVD technique capable of producing high quality epitaxial layers. It is a non-equilibrium growth technique which is based on reacting thermal atomic beams on a heated substrate surface. In MBE for group III-nitride usually the group III species are provided by metal sources such as (Ga, In, Al) and the nitrogen is supplied by a gas source. The delivery of the beam of atoms requires low pressures, ultra

high vacuum with background base pressure in the order of  $10^{-10}$  torr or less, while growth takes place at pressures of about  $10^{-5}$  torr. Under low pressures the atoms in the beam have very large mean free paths and the transport from the source to the substrate can be regarded as collisionless. The growth temperatures used in MBE are much lower than for MOCVD growth. For example GaN is usually grown at temperatures below its decomposition temperature ( $\sim 800$  °C) [55] and for InN the temperature can be as low as  $\sim 550$  °C [54]. A big advantage in MBE systems is that due to the vacuum conditions that are maintained, they allow in-situ monitoring of the growth process, typically involving electron diffraction (RHEED, LEED), which helps precisely to control the growth to a monolayer level, makes the process adjustable and eliminates much of the guessing. MBE technology has been created to improve the interfaces in structures such as superlattices and multiple quantum wells. At low temperatures, the diffusion is reduced, which results in very abrupt interfaces. InN and indium rich InGaN is hard to achieve under thermodynamic equilibrium because of the low dissociation temperature and high vapor pressure of nitrogen over InN. Plasma-assisted MBE (PAMBE) systems which use nitrogen plasma source to dissociate the nitrogen molecule, remain the dominating technology for the production of InN epilayers and InGaN alloys with high indium mole fraction [54].

A major drawback for MBE device production is that the growth rates are lower in comparison to MOCVD (often less than  $1\ \mu\text{m/hr}$ ), and the fact that Ga-face material cannot be grown directly on sapphire. Besides, the technique is very expensive, which makes it undesirable for mass production.

Similar to the MOCVD growth systems, there are various existing modifications of MBE reactors in order to address various problems inherent in the growth process. Such systems are metalorganic molecular beam epitaxy (MOMBE), migration-enhanced epitaxy (MEE), metal modulated epitaxy (MME), plasma etc. The MOMBE uses metalorganic chemical beams as group III sources. The MEE and MME methods are discussed in Section 2.2 in relation to the MEAgrow technique applied in the present work.

### 2.1.3 HVPE

Hydride Vapor Phase Epitaxy was used first for producing nitride semiconductors [2]. It is one of the common methods for growth of thick GaN which can be separated from the sapphire and used as a free-standing substrate. The growth rate can be very high, about  $1\mu\text{m}$  per minute. GaCl and  $\text{NH}_3$  are commonly used for precursors and the films are free from carbon contamination. GaN is grown on top of a heated substrate at about 1000-1100 °C. A drawback of this growth method is that HCl results as a byproduct from the reaction of GaCl with ammonia. HCl is very corrosive and results in fast degradation of the reactor. This technique is not able to produce sharp interfaces between the layers of a structure and thus, regardless of the high achievable growth rates and the reasonable quality of the GaN films, HVPE is harder to use for device production.

### 2.1.4 ALD

Atomic Layer Deposition is a low temperature chemical vapor deposition technique which relies on self-terminating surface reactions. For this method the precursors are pulsed separately in time with short purging periods. The growth rates are very slow

because of the layer-by-layer growth. The principles of operation of ALD and details for this growth technique are given in [57]. Due to the self-limiting process, the layers result in better uniformity because the precursors do not react among themselves and the reaction terminates when all the available sites are occupied. In ALD the film thickness can be controlled to an angstrom scale which makes it useful for device applications. Ammonia usually reacts with a group III precursor that may contain chlorine which results in the formation of HCl byproduct. The limitations of the thermal ALD for group III-nitrides growth are discussed in [58]. As a replacement of the ammonia precursor plasma-assisted ALD technique can be applied. In reference [58], Ozgit-Akgun et al. adopted to their ALD system a MEAglow hollow-cathode plasma source. The elemental analysis for the films produced in [58] confirmed that oxygen contamination was significantly reduced due to the use of the hollow-cathode plasma source. The MEAglow hollow-cathode plasma source is described in the next section in a relation to the growth system used in this thesis.

## 2.2 Description of the MEAglow growth technique

### 2.2.1 Method

In the present thesis a prototype growth technology, called MEAglow was used for the growth of group III-nitrides. MEAglow stands for Migration-Enhanced Afterglow Epitaxy and represents a hybrid between MBE and low pressure CVD systems. As was already mentioned, it transfers the migration-enhanced epitaxy method commonly used in MBE, to a CVD environment.

### 2.2.1.1 MEE

The MEE method has been originally developed in 1986 for GaAs/AlGaAs low temperature growth in MBE systems [59]. For nitride growth it is commonly employed in plasma-assisted MBE systems [60]. The method represents a pulse delivery of the metal and nitrogen precursors, which are separated in time. First a thin wetting metal layer is delivered and is subsequently consumed by nitrogen. A number of cycles are used to grow the semiconductor. The advantage of this method is in the increased surface diffusion of the adatoms, which is otherwise limited by the low growth temperatures. The growth interruption resulting from the separate pulsing of the precursors leaves extra time for the metal adatoms to find energetically favorable sites on the substrate lattice before being nitrided. This is aimed to improve the surface roughness and the crystal quality of the material when low growth temperatures are employed. Many groups have reported substantially improved crystalline quality and surface morphology of the group III-nitride binaries in MBE systems grown by MEE [61-63]. A drawback of this method, applied in MBE systems is that the growth rate is lower because only a monolayer can be grown at a time due to the formation of metal droplets.

### 2.2.1.2 MME

Metal Modulated Epitaxy is an improved version of MEE in which only the metal fluxes are modulated while the nitrogen plasma flux is kept continuous. It is applied in plasma-assisted MBE systems. The metal flux is set much higher than the nitrogen flux for increasing the migration length [64]. These conditions in non-modulated mode lead to droplet buildup but the short modulations of the shutter prevent it. The layer is depleted

after closing the shutter and the droplets are consumed by the nitrogen flux. This growth technology was sophisticated in MBE systems by computer control of the shutter transitions, also called “smart-shuttering” which is based on the feedback from RHEED transients [64]. The MME method has shown a great improvement in the surface roughness and crystal quality of the materials, as well as growth rate and the production of reproducible p-type Mg-doped GaN having extremely high hole concentrations [65]. The achieved growth rates with MME in MBE systems reach up to 90% of the normal non-modulated MBE growth.

There are several other reports for growth methods that make use of interruption during growth, which have succeeded in producing good quality of GaN. Some of them, for example, use simultaneous pulsing of nitrogen and gallium fluxes, others use pulsing of time-averaged variable gallium fluxes [61].

The advantage of migrating MEE to a CVD reactor is that large deposition areas can be exploited [66]. The growth in the MEAgrow system is carried out at much higher pressures than in MBE systems. This allows for nitrogen collisions in the gas phase, which results in a reduction of the energy of the plasma species (both kinetic energy and potential energy) and leaves mainly the long-lived molecular species to participate in the reaction [66].

### 2.2.2 The MEAgrow System

The MEAgrow system is shown in Figure 2.1. The reactor consists of three chambers pumped independently, plasma source, gas cabinet, and control panel connected to a computer. It has been presented and described in detail in [67, 68].



Figure 2.1 The MEAglow growth system.

The excited nitrogen species are introduced downwards from the top of the reactor from a specifically designed for the purpose scalable hollow-cathode plasma source [67, 69], utilizing ultrahigh purity nitrogen (99.9 % pure). The nitrogen is further purified by an inert gas purifier at the plasma line inlet. The plasma source can be operated in either RF or DC mode. It can be scaled by increasing the number of the holes and this enables growth over larger areas in comparison to MBE systems. For the present work the plasma generator was operated only in RF mode at the standard frequency of 13.56 MHz. The plasma source doesn't use a quartz or alumina tube, commonly applied in other inductively coupled RF and microwave plasma sources, so the oxygen level of contamination is reduced to a minimum [70,58]. A schematic view of the nitrogen plasma source is presented on Figure 2.2. There are two hollow-cathode arrays. The grounded array is for DC operation (as the live electrode is at negative voltage). For RF operation the hollow-cathode array on the active RF electrode is more active because the DC bias at that electrode is positive. The grounded array still acts as a hollow-cathode in relation to

the potential of the plasma. The electron density has been measured at the grounded hollow-cathode array to be  $9 \times 10^{11} / \text{cm}^3$  at the maximum 600W of RF power [69]. Other plasma sources having low oxygen contamination are the capacitively coupled sources but they reach electron densities in the order of  $10^9$ - $10^{10} / \text{cm}^3$ . The plasma source is also suitable for fast switching between on and off mode, which is needed for the nitrogen pulsing in the migration-enhanced growth regime.

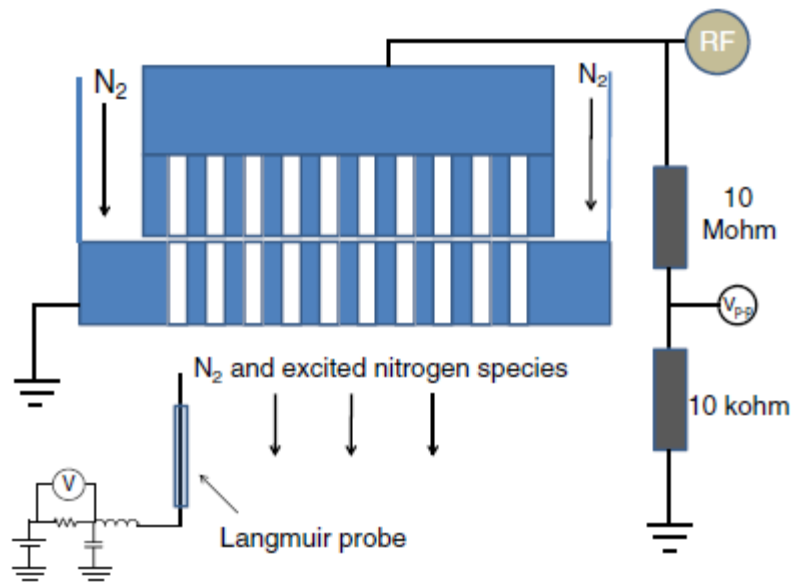


Figure 2.2 Scheme of the MEAgrow hollow-cathode plasma source, as it was presented in [69] by Butcher et al.

The reaction chamber is the main chamber of the system where the growth takes place. It is being pumped to the upper end of the UHV regime to about  $10^{-7}$  torr, though the system has reached vacuums of  $<10^{-8}$  Torr. The vacuum is continuously maintained in order to reduce the contamination coming from background water vapor which is very hard to pump out. This is achieved by means of independently pumping system using a

combination of rotary pump and an Edwards STPH301C high throughput turbomolecular pump that reaches 48,000 rpm and can handle gas flows as high as 2500 sccm. An MKS throttle valve with feedback from a baratron gauge were used to control the pressure during growth, which varied between 1 and 4 torr. The substrate holder stage is located in the middle of the main chamber and is capable of rotation up to 50 rpm. The height of the sample holder is adjustable. A 4 inches heater is situated below the sample holder and is capable of maintaining temperatures up to 700 °C. At these temperatures all the metalorganic used for film growth will efficiently decompose. The highest decomposition temperature is for the TMG which starts decomposing at 500 °C but the last methyl group is freed at about 650 °C [71]. A thermocouple for measuring the temperature is placed below the heater and sends the readout to a computer which automatically varies the DC voltage via a PID controller.

The growth chamber is equipped also with pyrometer and RHEED which are meant for optical control of the growth. The RHEED gun cannot be used during growth since the growth pressures are relatively high and there is also a possibility of contamination with metalorganic, but it could be used for post-growth analysis, or the growth process could be interrupted and the chamber pressure can be pumped down to vacuum level. A separate independently pumped chamber contains a Residual Gas Analyzer (RGA) which is used to monitor the amount of the various elements and molecules during growth. A pressure of about  $10^{-8}$  torr is maintained for the RGA operation. The residual gas analyzer is also used for leak detection. Helium gas was used for the leak test because the helium molecules are light and diffuse quickly into the chamber.

The third chamber is used to introduce the sample into the main chamber without air contamination. It is called the Load Lock Chamber. The load lock chamber is equipped with a transfer arm and is separated from the main chamber by a pneumatic gate valve. The load lock chamber is equipped with a rotary and turbomolecular pumps and is capable of quickly lowering the pressure down to  $10^{-6}$  torr.

The metalorganic bubblers are stored in a separate gas distribution cabinet, which is connected to the main chamber for the transport of the group III species. The MEAglow reactor uses trimethylindium (TMI)  $\text{In}(\text{CH}_3)_3$ , trimethylgallium (TMG)  $\text{Ga}(\text{CH}_3)_3$ , trimethylaluminium (TMAI)  $\text{Al}(\text{CH}_3)_3$  and biscyclopentadienyl magnesium  $\text{Cp}_2\text{Mg}$ . The metal alkyl vapors are transported from the bubblers to the reaction chamber by using nitrogen gas. The flow rates are precisely controlled by mass-flow controllers. The metalorganic species are supplied to the growth chamber by a metalorganic inlet and are directed towards the sample surface by a showerhead, positioned at the side of the sample holder. There are four gas lines implemented to the growth chamber - two purge lines, a plasma line, vapor line and a vapor bypass line. The plasma line carries nitrogen gas to the plasma generator. The vapor line delivers the vapor from the metalorganic sources to the growth chamber and is pressure regulated with nitrogen. The bypass line collects the bypass from each metalorganic line and sends it to a bypass pump.

There is a small control cabinet attached on the back of the gas cabinet housing the temperatures controllers for the bubblers and the power inlets for TMI and TMAI bubbler heaters. Though, using direct vapor injection temperature control is not as critical as when a carrier gas is used.

The MEAgrowth process is entirely computer controlled. The growth is implemented in the form of computer programmed recipes, using a Plasmionique Flocon system, from where the various growth parameters, like for example, pressure, gas flow rate, temperature, are varied.

## Chapter 3. Characterization methods

### 3.1 X-ray Photoelectron Spectroscopy (XPS)

The XPS technique is an electron spectroscopic method for surface characterization. This technique is also known as Electron Spectroscopy for Chemical Analysis (ESCA) and is mainly used for determining the chemical composition of the materials. XPS is very surface sensitive and provides information for the elemental and chemical composition of only the first 2 – 10 nm of the surface. With XPS all elements having an atomic number larger than 2 can be detected. It is not able to detect hydrogen ( $Z = 1$ ) and helium ( $Z = 2$ ). It can provide information for elements present in atomic concentrations  $>0.1\%$ . With XPS a quantitative analysis can also be performed for determining the relative atomic concentration for the elements present on the surface. Destructive depth elemental profiles are also possible with XPS up to several hundreds of nanometers by ion etching.

The XPS method is based on the photoelectric effect. The measurements are carried out in ultra high vacuum conditions by irradiating the sample with soft x-rays having sufficient energy to eject a core electron from an atom. The kinetic energy of the resulting photoelectron can be measured to determine the binding energy of the electron using the relationship [72]:

$$(1)$$

where  $h\nu$  is the photon energy and  $\phi$  is the work function of the spectrometer. The binding energy is unique for each element and is equal to the energy difference between

the final state of an atom, having  $(n-1)$  electrons and the initial state of the atom with  $n$  electrons.

Another type of electron is also produced as a result of the relaxation of the excited atom, and these electrons appear on the XPS spectra in addition to the photoelectrons. These are the so called Auger electrons. The Auger process occurs when an electron from an outer shell fills an inner vacancy in the orbital and a second electron is released from the outer shell to reduce the energy of the orbital.

XPS spectra for MEAglow grown GaN samples were taken with a Kratos Axis Ultra DLD instrument.

### 3.2 Secondary Ion Mass Spectroscopy (SIMS)

Secondary ion mass spectroscopy is a destructive ion beam technique commonly used for elemental detection in solids. The surface is bombarded with heavy ions and emission of secondary particles is induced from the sample surface such as electrons, neutral species, atoms and molecules or ion clusters. It is the charged secondary ions that are detected using a mass spectrometer and the obtained spectra enable a detailed analysis for the chemical composition of the surface.

There are two different SIMS analyses based on the sputtering processes. These are static SIMS and dynamic SIMS. In static SIMS a very low primary ion current densities are used, so that the surface is not strongly modified. SIMS offers several advantages over XPS such as hydrogen detection, very high sensitivity for many elements and compounds which can be detected in the range of parts per million to parts per billion and it can also provide direct compound detection by molecular secondary ion emission [73].

Dynamic SIMS is used for elemental analysis as a function of depth. In dynamic SIMS high primary ion current densities are applied, so that it yields higher secondary ion flux.

### 3.3 X-ray Diffraction (XRD)

X-ray diffraction is a non-destructive characterization method used for determining the structural properties of crystals, such as phase composition, grain size, crystal orientation, defects, and strain state. The incident x-rays with a characteristic wavelength are diffracted by the crystal in accordance to Bragg's law [74], as is shown on Figure 3.1. These x-rays are generated by bombarding a metal anode (usually Cu) with electrons in an x-ray tube. The condition for diffraction by a crystal is:

$$(2)$$

where  $n$  is the diffraction order,  $d$  is the spacing between the successive atomic planes, and  $\theta$  is the Bragg angle at which the incident beam must probe the crystal in order to occur constructive interference. From this relationship, the interplanar spacing can be determined for known angles. In experiments the  $\theta$  angle is measured. The information for the crystal structure is derived from the position, the shape and the intensity of the Bragg reflections. The peak positions can be compared with the data from the International standard data base (JCPDF).

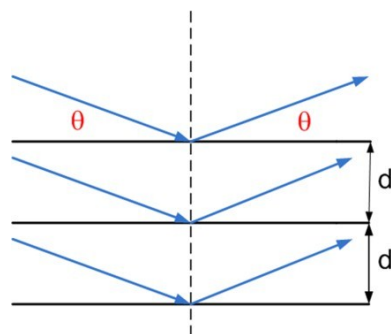


Figure 3.1 Illustration of x-ray diffraction from crystal planes according to Bragg's law.

In this work a PANalytical X'Pert Pro MRD powder diffractometer (with Cu anode,  $\text{CuK}\alpha$ ) was used for obtaining information about the crystal structure and phase composition of the studied group III-nitrides. The diffractometer was operated at 40 kV tube tension and 20 mA emission current.

The routine symmetric  $\omega - 2\theta$  scans were performed with a step size of  $0.002^\circ$  and 3.57 s in the range of  $30$  to  $40^\circ 2\theta$ . The  $\omega$  angle denotes the angle where the incident x-ray meets the sample surface, and the diffracted angle  $2\theta$  is defined between the incident beam and the detector angle, so that  $\omega$  is always half of  $2\theta$ . These routine measurements retrieved information for the c-oriented crystals and the interplanar spacing. The c lattice constant was determined by the following relationship [75]:

$$\frac{1}{d^2} = \frac{h^2 + k^2}{a^2} + \frac{l^2}{c^2} \quad (3)$$

where  $h, k, l$  are the Miller indexes, and  $a$  is the in-plane lattice constant. From this expression, the c lattice constant can be determined as

X-ray rocking curves were performed for one of the InN samples. The results were shown in Chapter 5. XRC is a versatile structure analysis tool which is typically used to study

single crystals. It can provide information for mosaic spread, dislocation density, strain, and ternary composition. In this work the method was only used to confirm that the layers were epitaxial by looking at the omega scan. A detailed description of the method is given in [76].

### 3.4 Optical transmission spectroscopy

Optical transmission spectroscopy is a very powerful characterization method, which is commonly used to derive optical parameters, such as the absorption coefficient ( $\alpha$ ) and the energy bandgap of the material. This technique can also give information for thin film thicknesses, refractive index, and the crystal quality.

For determining the energy bandgap from the optical absorption spectra the following relationship for the absorption coefficient is used:

$$\alpha = A(h\nu - E_g)^n \quad (4)$$

where  $h\nu$  is the photon energy,  $E_g$  is the energy bandgap, and  $A$  is a constant depending on the electronic transition. For direct transitions  $n = 1/2$ , and for indirect transitions  $n = 2$ , whereas for forbidden transitions  $n = 3/2$  for direct transitions and 3 for forbidden indirect transitions. From expression (4) follows that the energy bandgap can be derived from a plot as an intercept of the linear part of the absorption coefficient squared with the x-axis, representing the photon energy [77].

In this work instead of the absorption coefficient squared, the optical density squared is used for determining the energy bandgap. Optical density squared (ODS) is proportional to the absorption coefficient squared and is defined by the following relationship [77]:

$$- \quad , \quad (5)$$

where  $t$  is the thickness of the film,  $I_0$  is the intensity of the incident radiation, and  $I$  is the intensity of the transmitted light. The plot of ODS against the photon energy gives qualitative information about the film thickness, which can be judged from the steepness of the slope of ODS (compared to known spectra) [78]. The sample thicknesses in some of the experiments in this work were calculated from the interference fringes from the transmission spectra, assuming a known refractive index, as follows [79]:

$$\frac{2nt}{\lambda} = m, \quad (6)$$

The thicknesses of InGaN samples were calculated assuming  $n$  equal to the refractive index for GaN. The wavelengths  $\lambda_1$  and  $\lambda_2$  denote the location between two successive interference maxima and  $m$  represents the interference order between  $\lambda_1$  and  $\lambda_2$ .

Two spectrophotometers were used to carry out the optical transmission measurements in this work – a Cary 5E with wavelength range from 175 – 3300 nm, and a Cary 50 with wavelength range of 190 – 1100 nm. The light sources for the Cary 5E were a deuterium lamp for the UV wavelength range and a tungsten halide lamp for the visible to near infrared range. The detectors were a photomultiplier tube for the UV – visible range and a Peltier-cooled lead sulfide photocell for the NIR. The Varian Cary 50 instrument uses a full range xenon pulse lamp as a light source and dual silicon diode detectors.

Baseline and zero corrections were taken before each measurement. The transmission percentage is calculated by the software by dividing the sample data for each wavelength

to the baseline for the corresponding wavelength. The relationship for the transmittance is as follows:

$$\frac{I_{\lambda}}{I_{\lambda_0}} = e^{-\epsilon c l} \quad (7)$$

where  $I_{\lambda}$  is the intensity of the sample at a particular wavelength and  $I_{\lambda_0}$  is the reference intensity at the same wavelength.

### 3.5 Atomic Force Microscopy (AFM)

Atomic Force Microscopy is a non-destructive imaging technique for surface characterization with atomic scale resolution. The AFM microscope uses a mechanical method for scanning the sample surface. A sharpened tip is mounted on a cantilever and positioned close to the sample surface. The cantilever deflects from the surface in accordance with the forces between the tip and the sample surface. This deflection is recorded and used to produce an image. The microscope can be used in various modes for examining different surface properties. The two main modes are static (contact) and dynamic (non-contact) modes [80].

Routine AFM imaging measurements were performed in this study to obtain the 3D topography of the surface in tapping non-contact mode. Tapping mode is used for topography imaging of the surfaces which could be easily damaged or surfaces that are hard to measure with other AFM modes. In tapping mode the tip is alternately placed in contact with the surface for a short time and then is lifted off to avoid dragging of the tip. Tapping mode is used in ambient air. The cantilever in this mode is oscillated at or close to its resonant frequency.

The measurements were taken with an AFM Nanosurf Easyscan 2 atomic force microscope using silicon probes model AppNano ACLA, having a tip radius of 6 nm.

The root mean square value of surface roughness was determined from the scans to give relative estimation of the level of roughness on the samples surface.

### 3.6 Scanning Electron Microscopy (SEM)

Scanning electron microscopy is a surface characterization technique. The microscope is shown in Figure 3.2. The microscope uses an electron beam produced at the top of an electron column which passes through the column where electron lenses are used to focus the beam on the sample surface. Different signals are produced and detected from the surface such as secondary electrons, backscattered electrons, Auger electrons, and characteristic x-rays. They are detected with different detectors and give information about the sample surface and composition. The characteristic x-rays are used for determining the chemical composition with energy dispersive x-ray spectroscopy (EDX), while secondary electrons are typically used for imaging.



Figure 3.2 The Hitachi SU-70 SEM as shown in the Hitachi commercial brochure.

The SEM micrographs used in this work were taken with a ultrahigh resolution Schottky emission Hitachi SU 70 microscope. High-resolution images taken with the microscope are shown in Figure 3.3. The resolution of the microscope was sufficient to provide clear details in the cross-sectional images for the conductive samples. The imaging of the highly resistive samples was challenging due to large charging effects.

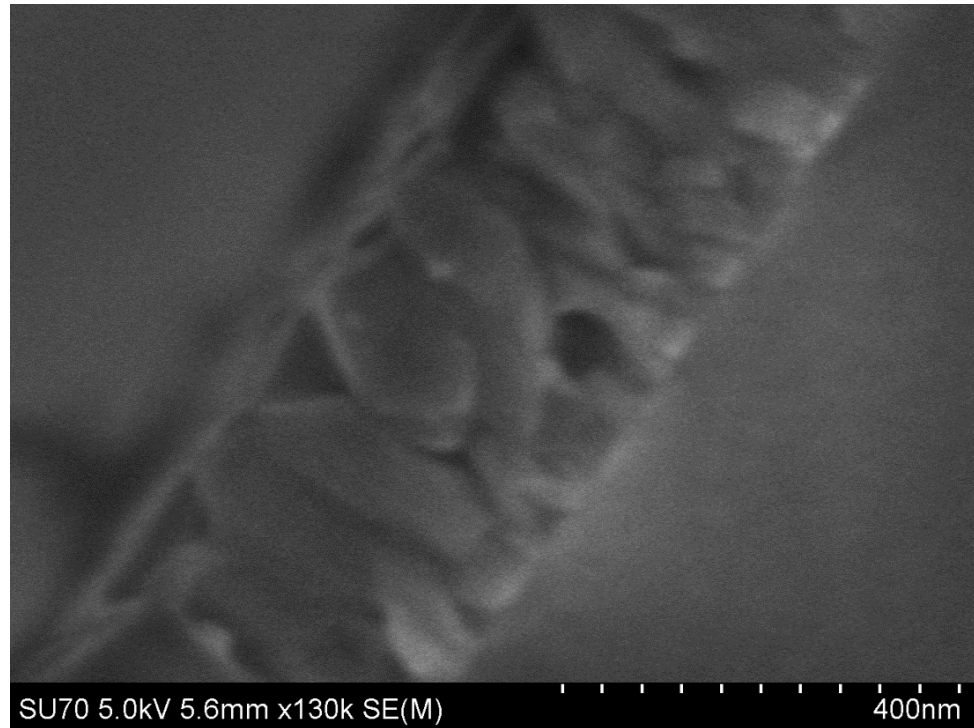


Figure 3.3 InN cross-sectional high resolution image taken with the Hitachi SU-70 SEM.

### 3.7 Hall Effect

The electrical properties were measured by Hall Effect in Van der Pauw geometry [81]. About 1 cm large square pieces were taken from the centre of the samples to avoid edge effects and indium contacts were placed in the four corners. The samples were then mounted in an Ecopia HMS-3000 Hall effect system. All measurements were carried out at room temperature. The strength of the magnetic field was 1 T, a permanent magnet was used, which provides a lower noise measurement than an electromagnet.

The resistivity of the thin films was measured by applying constant current between two adjacent contacts and the voltage is measured across the other two contacts. The resistivity can be determined from the van der Pauw relation [81]:

$$- \quad - \quad - \quad (8)$$

Where  $\kappa$  is the van der Pauw correction factor. The subscripts are the respective terminals. The mobility and the carrier concentration are determined by:

$$- \quad - \quad (9)$$

Where  $r$  is a factor dependent on the scattering type and the degree of degeneracy and  $R_H$  is the Hall coefficient.

## Chapter 4. MEAglow grown GaN

### 4.1 Preliminary experiments

#### 4.1.1 Growth conditions

GaN was grown by the MEAglow technique under conditions for metal modulated epitaxy. The MME method was initially created for MBE systems and was presented in detail in Chapter 2.

Metal modulated epitaxy (MME) hasn't been used before for growth with a MEAglow system, and some preliminary runs were needed to characterize the growth parameters. The aim was to achieve smooth, stoichiometric layers with energy bandgap of 3.4 eV that grew at fast growth rates at low deposition temperatures. Such layers can be used as buffer layers for further device application where very smooth surfaces are required to achieve sharp interfaces. Growth at low temperatures allows deposition at larger areas than the commonly used 2'' wafers and in this way the costs for the material's production can be reduced [69].

Initial conditions were set for similar pulsed mode conditions as had been previously used for MME in an MBE system [65]. A series of experiments were performed to first examine the thickness variation in these preliminary GaN growths by varying only the total growth time.

The GaN films were grown on c-axis 2'' sapphire wafers at 630 °C under 1.6 torr chamber pressure. The TMG and nitrogen flow rates were set to 1 sccm and 1800 sccm respectively. The plasma source was operating at 600W RF power continuously

providing active nitrogen throughout the cycling periods. A cycle period lasted 55 s modulating only the trimethylgallium flow rate for 30 seconds on and 25 seconds off. Each growth was terminated by a plasma step having duration of 7 minutes at the end of growth. The variation of the total growth time is presented in Table 4.1.

Table 4.1 Variable growth parameters

Sample Id	Total growth time	Number of cycles
Sample 1	2895	45
Sample 2	40020	45x16
Sample 3	10320x3	45x4

The total growth time in Table 4.1 was calculated by multiplying the cycle length by the number of cycles. For the first GaN layer (Sample 1) a nominal number of 45 cycles was selected. The total growth time for Sample 2 was increased to 11.11 h from 50 min for Sample 1, in order to achieve a thicker layer. After each 45<sup>th</sup> cycle a cooling and reheating step were performed to reduce powder formation from gas phase reactions that were found to affect the samples for longer growth times. Sample 3 was grown under exactly the same conditions as the previous two samples but the growth was split into three parts, each consisting of 45x4 cycles, in order to monitor the thickness variation throughout the growth process. Sample 3 was taken out of the growth chamber after each run for x-ray diffraction and optical transmission measurements and was then etched in HCl:H<sub>2</sub>O (1:1) solution to remove surface contaminants prior to each subsequent growth.

#### 4.1.2 Results and analysis

All of these 3 MME grown GaN samples had a very dark metallic appearance and semi-insulating electrical characteristics. Characterization was performed by x-ray diffraction  $\omega$ - $2\theta$  symmetric scans, optical absorption spectroscopy and atomic force microscopy.

Optical transmission and absorption spectra for the samples of the 45 and 45x4 cycle film growths (1 and 2, respectively) are presented in Figure 4.1 and Figure 4.2. There are no visible interference fringes present on the transmission spectra at higher than the absorption edge wavelengths, which suggests that both layers were very thin. Both layers also appear to have similar thickness. This is also evidenced by the equal slope of the linear part of the optical density squared plots for both of the absorption spectra. The energy bandgap was estimated from the optical absorption spectra to be 3.3 eV which is 0.1 eV lower than the reported value of 3.4 eV for stoichiometric GaN [28]. Such a low bandgap was mainly observed in this work with non-stoichiometric films grown under metal rich conditions. Similar absorption spectra have been reported previously for metal rich GaN [82].

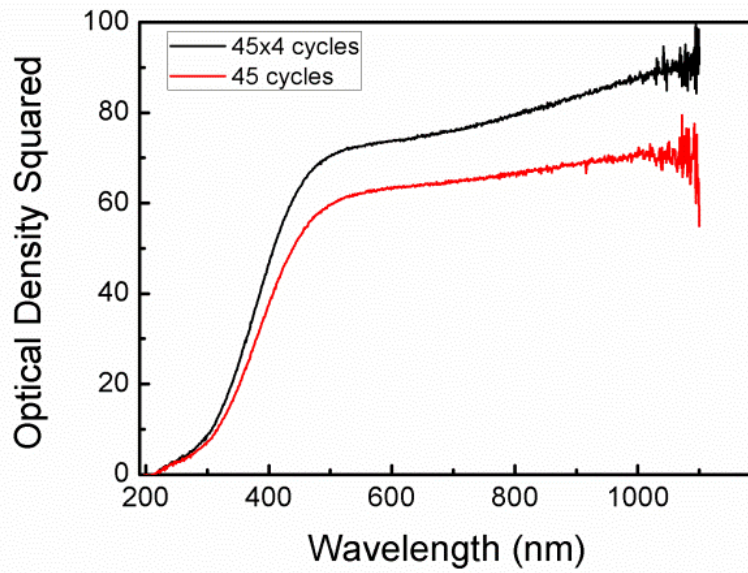


Figure 4.1 Optical transmission spectra for Sample 1 and Run 1 of Sample 3.

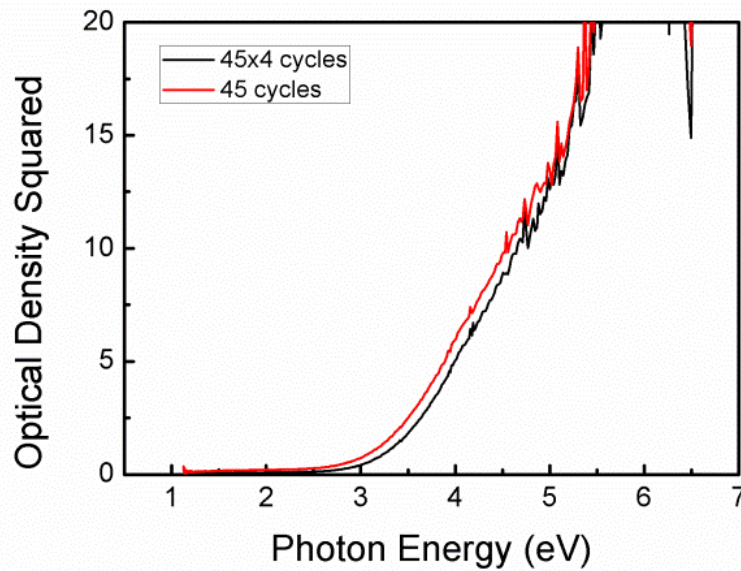


Figure 4.2 Optical absorption for Sample 1 and Run 1 of Sample 3.

The thickness and energy bandgaps of the samples, which were determined from the absorption spectra, are shown in Table 4.2. The two -undetermined values for the energy bandgap from absorption spectra are as a result of the non-linear dependence of the

absorption coefficient squared and the photon energy for those samples, which made an extrapolation with the x-axis impossible. An example absorption spectrum for this is shown in Figure 4.3 (Sample 2). The range of the absorption edges for these samples was between 3.2 eV and 3.3 eV. From the similar values of the thicknesses in Table 4.2, it is evident that the growth rate didn't increase linearly with the increase of the total growth time. This suggests that the growth surface was poisoned, disallowing or severely curtailing further growth.

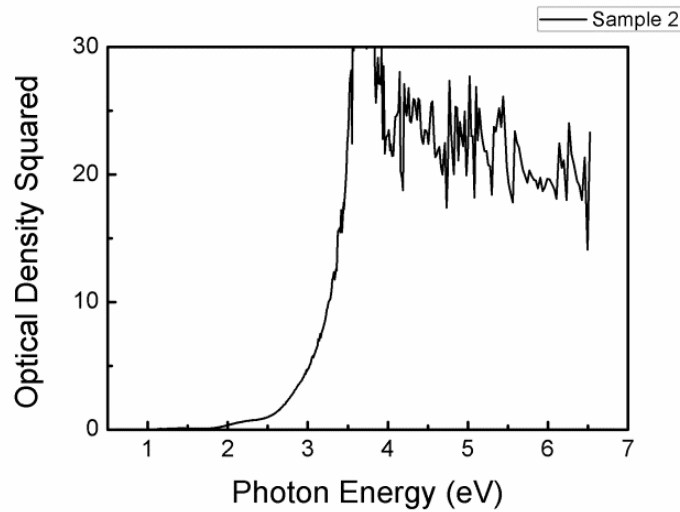


Figure 4.3 Optical absorption spectrum for Sample 2, for which no linear part of the spectrum was found to extrapolate with the x-axis.

Table 4.2 Thickness and energy bandgap comparison from the optical absorption spectra for samples 1-3. The performed measurements after each 45x4 cycles for the three runs of Sample 3 are denoted as 3a, 3b, and 3c.

Sample ID	Thickness (nm)	E <sub>g</sub> (eV)
Sample 1	undetermined	3.3
Sample 2	357	undetermined
Sample 3a	Undetermined	3.3
Sample 3b	238	3.23

Sample 3c	334	undetermined
-----------	-----	--------------

The optical transmission spectra from the three separate runs of Sample 3 are presented in Figure 4.4a). Few interference fringes for the subsequent growths after the first run are present on the spectra from which information about the film thickness was taken. These spectra show absorption at high wavelengths, which is not characteristic for stoichiometric GaN layers. The GaN layers are typically 70-80 % transparent for energies below the energy bandgap. The onset of the absorption shifts to higher wavelength with an increased total growth time of the film. This indicates a metal, or other impurity, buildup in the layers that increases absorption at these low energies. Optical transmission spectrum of a commercial MOCVD stoichiometric GaN layer is presented in Figure 4.4b) for comparison.

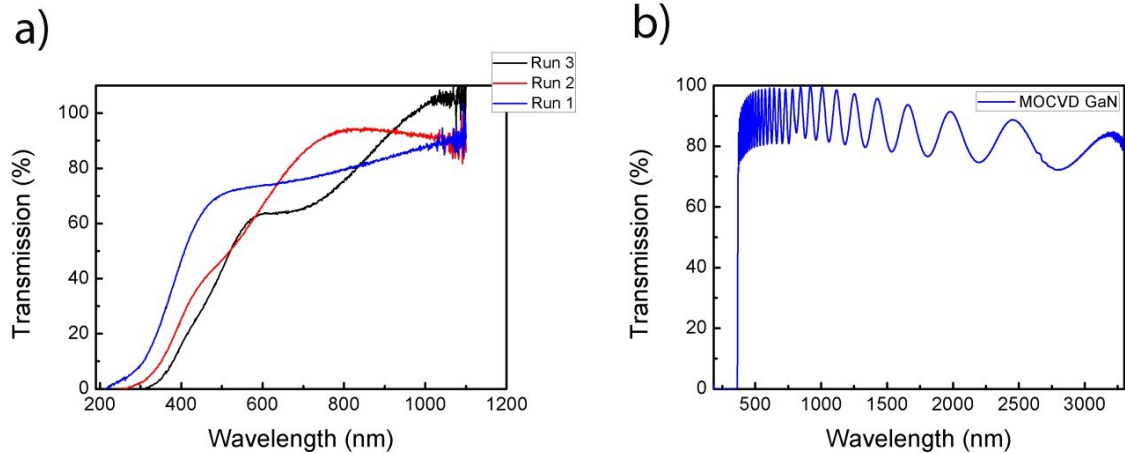


Figure 4.4 Optical transmission spectra for a) the three growth runs of Sample 3, b) stoichiometric commercial GaN template

Contamination of the growth surface from incompletely decomposed trimethylgallium, most likely in the form of methylgallium, or from excess free gallium, were suggested as possible reasons for the decreased growth rate of the studied GaN layers at the relatively low deposition temperatures employed. At low temperatures usually the third methyl group from the trimethylgallium is hard to decompose and impurities in the form of monomethyl gallium, carbon or free gallium metal get incorporated into the film which hinders further growth.

The surface of Sample 3 was studied further with x-ray photoelectron spectroscopy to identify any possible carbon or metal contamination. A Kratos Axis Ultra DLD instrument located at University of Ottawa was used. Wide scans were performed with a constant pass energy of the analyser of 80 eV, and narrow scan spectra were acquired for the main elements with a 20 eV pass energy, using a monochromatic Al K $\alpha$  x-ray source. Curve fitting was performed for the deconvolution of the peaks and relative atomic percentages were calculated using CasaXPS software. Since the MEAgrow GaN samples were semi-insulating the peaks positions were corrected for surface charging effects using the known position of the adventitious hydrocarbon peak at 284.8 eV, which is always present as a surface contaminant after exposure of the film to the atmosphere [83].

The data from Sample 3 was compared to data for a commercial GaN template taken with a very high resolution XPS instrument, and three additional MEAgrow grown samples that were grown under different conditions (measured using the Ottawa system) with different characteristics. One of the samples (Sample 4) was extremely smooth semi-insulating GaN. This sample had a transparent appearance and was closer to stoichiometry. The second MEAgrow sample studied with XPS for comparison (Sample

5) was very non-uniform and had a very rough surface. This sample was spotty and had visible dark and transparent parts and two pieces, one from each of the two parts were taken for XPS analysis. The common feature between these two additional samples and Sample 3 was the termination of the surface with a 7 minutes long nitrogen plasma step. The third MEAgrow sample used for comparison (Sample 6) was grown under very similar conditions to Sample 3 but had a shorter terminating plasma step of 12.5 s. This shorter nitridation was used to ensure that any possible inclusions of free gallium metal that might be present after growth on the film were not removed during the final nitridation. The growth conditions for the additional 2 samples are listed in Table 4.3.

Table 4.3 Growth parameters for the two additional samples grown under less Ga-rich conditions

Sample ID	Pressure (torr)	Temperature (°C)	TMG (sccm)	N2 (sccm)	Surface Termination	TMG On (s)	TMG Off (s)
Sample 4	1.2	660	1	1400	7 minutes plasma	30	25
Sample 5	1.2	660	1	1400	7 minutes plasma	30	25

A tentative peak assignment was done based on information available in the literature. As is often the case with XPS, instrumental resolution and the overlap of peaks limited the ability to accurately determine peak components. The assignments given here are therefore tentative, though supporting evidence from the literature was used. The peak fitting procedure and some of the supporting XPS data are shown in Appendix A.

The surfaces of Sample 3, Sample 5A and 5B were etched in HCl:H<sub>2</sub>O (1:1) solution to remove surface contaminants (including the oxide) before the XPS measurement. The measurement of Sample 4 was performed after 6 months without any subsequent etching so that a thicker oxide may have formed on the surface. Sample 6 also wasn't etched, and therefore it could also have had a thicker surface oxide.

The carbon 1s line for Sample 3 and Sample 6 revealed four peaks in addition to the peak due to adventitious hydrocarbon (Figure 4.5). The two peaks at 280.8 eV and 282.7 eV are probably due to Ga-C and Ga-CH bonds originating from the incorporation of Ga-CH complexes from partially decomposed TMG. This is suggested because both samples were grown under very metal rich conditions and relatively low temperatures. At temperatures lower than 600 °C one of the methyl groups is more likely to be incorporated in the film, since TMG decomposes more completely above 600 °C [84]. From the quantification results, the total amount of carbon present on the surface was found to be 29% of all the main elements present. This was for an RMS surface roughness, measured by AFM, of only 4 nm for the films, as compared to the 0.5 nm RMS surface roughness measured for a typical commercially available unintentionally doped GaN sample. The carbon concentration for the commercial sample was only 8.9%.

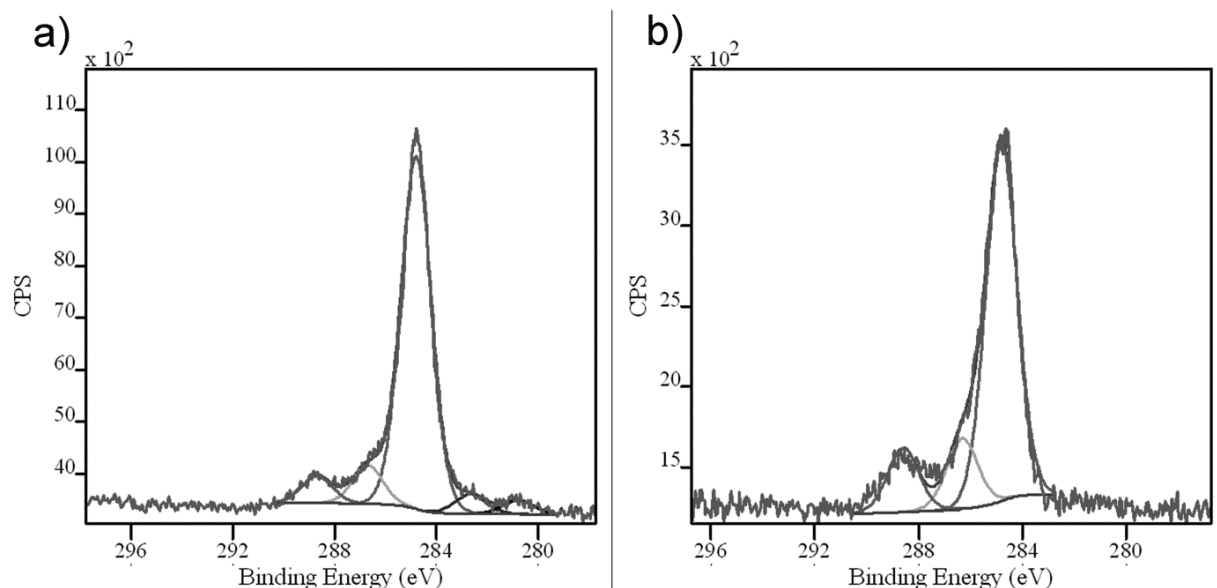


Figure 4.5 High resolution XPS spectra of Carbon 1s for a) Sample 3 and b) Sample 4

Samples 4 and 5 were not grown in very metal rich conditions, so for these samples the C 1s peaks below the hydrocarbon, related to Ga-CH bonds, were not present (Figure 4.5b)). Therefore, the carbon contamination level in the bulk of the GaN film (since these are bulk contribution rather than a surface contribution) was significantly reduced. The peaks at the positions of 286.7 eV and 288.7 eV were common for all the MEAglow grown samples and were found to belong to C-N and C-O bonds, respectively [85,86]. The C-N peak is ascribed to bonds with additional nitrogen species observed in N 1s transition resulting from the termination of the growth with plasma. For the commercial GaN template just the 288.7 eV peak, due to C-O bonds, was present in addition to the adventitious hydrocarbon.

Both Ga 2p and Ga 3d transitions represent broad single peaks, and for each of these were fitted three components. The Ga 3d peaks were centered at a position between the energy reported for metallic gallium and the binding energy reported for Ga-N bonds, which may

indicate inclusions of free gallium in the bulk film. According to [87] where the author examines Ga and N terminated surfaces, a surface terminated with nitrogen can shift the Ga 3d peak to lower energy positions and a surface terminated with Ga can shift it to higher positions since there will be more Ga likely bonded to oxygen, which is due to the chemical shift in the oxidation state with XPS. The Ga 2p and Ga 3d peaks for the MEAglow samples were all shifted to lower binding energies, possibly due to metallic inclusions. The contribution from gallium metal is hard to resolve after the sample exposure to air, as the free metal tends to bond with oxygen and will form surface oxide, so a distinct peak due to Ga-Ga bond may not be observable [88]. Possible Ga-C bonds are unresolvable within the broad peaks.

The N 1s peak is broad and includes the Ga LMM Auger feature which overlaps at 396 eV with N 1s when an Al  $K\alpha$  X-ray source is used for the XPS. The use of this source was preferred over the other commonly used source, Mg  $K\alpha$ , because a Ga Auger peak interferes with the position of the adventitious carbon and a correction for the charging cannot be applied when using that source. All the MEAglow samples contain multiple components from chemisorbed nitrogen surface species in the N 1s transition because the surface was flooded at the end with nitrogen plasma. Only Sample 6 which was terminated with a short nitridation step revealed only one peak in addition to the main peak at 398 eV. The commercial GaN for comparison didn't indicate additional components except for the peak due to surface hydrolysis, explained below.

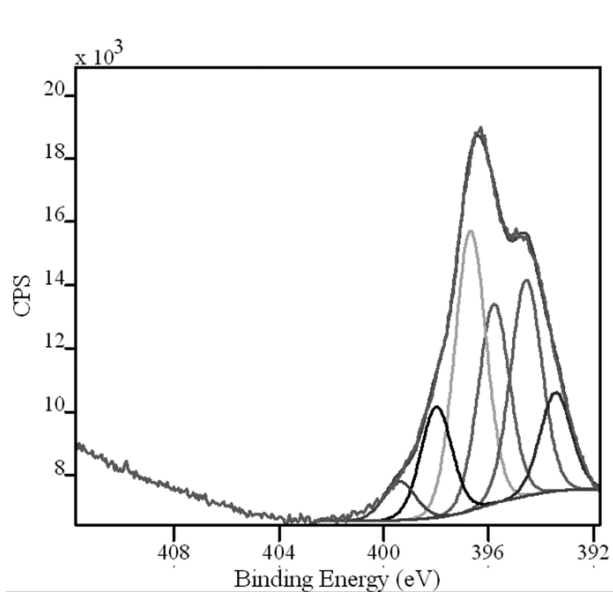


Figure 4.6 High resolution XPS spectrum of N1s for Sample 3.

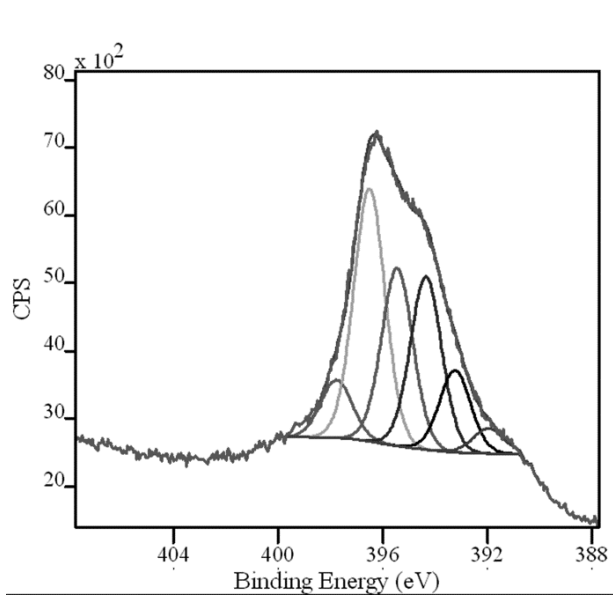


Figure 4.7 High resolution XPS spectrum of N1s for Sample 4.

Two N 1s components at 398 eV and 399.5 eV were found for all MEAglow samples. These are shown in Figures 4.6 and 4.7. The peak at 398.2 eV was found previously to originate from atomic nitrogen incorporated in dysprosium nitride films [89] and as a contribution to the N1s in nitrogen rich InN films, grown with plasma-assisted CVD

technology. The second peak at 399.5 eV was ascribed to N-H or N-C bond [90]. The N-H species can result from  $\text{NH}_3$ , which forms as a product of the surface hydrolysis of GaN when the material is exposed to water in air by the following reaction:



Aluminium was present on the survey spectrum of part A (the transparent part) of Sample 5. The sample wasn't homogeneous and the observed aluminium may have originated from the sapphire surface. The components for the peak fitting for Sample 5B are shown on Figure 4.8. Significant broadening of the N 1s transition for the two parts of Sample 5 is observed at higher binding energies which can be ascribed to chemisorbed nitrogen surface species. Aluminum bonded to nitrogen can also contribute to the broadening but the reported peak position of N 1s for AlN overlaps with the N 1s peak position for GaN. An N 1s Transition at 402 eV is also evident for sample 5A and 5B which can be attributed to nitrogen bound to oxygen from the sapphire. Chemisorbed molecular nitrogen was also observed for TiN films at the same binding energy and may be another possible suggestion [91]. The contributions for surface chemisorbed species are a lot higher for Sample 5 in comparison to the other MEAgrow grown GaN films. The peaks below 396.4 eV are fitted for the purpose of removing from the quantification report of the components the contribution of the overlapping Ga Auger peak.

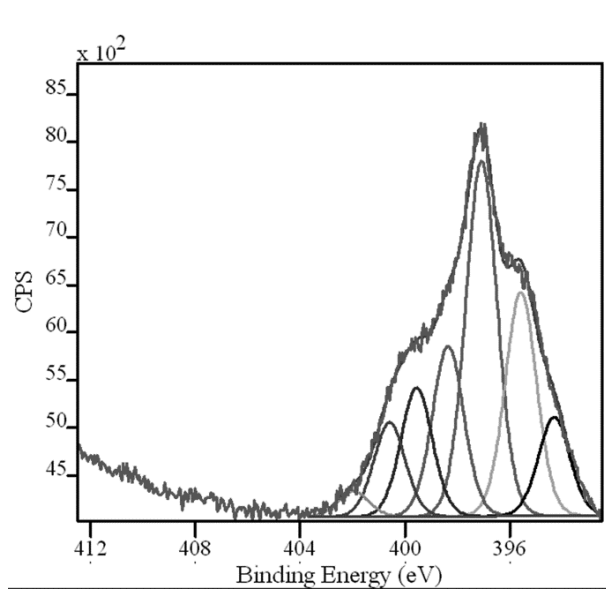


Figure 4.8 High resolution XPS spectrum of N 1s for Sample 5B

The early MME growth attempts, produced by pulsing in the metal rich regime at low temperatures resulted in the incorporation of background impurities degrading the structural and optical quality of the layers. After continuous optimization of the growth process near stoichiometric good quality GaN layers were achieved and the level of the contaminants was significantly reduced.

On Figures 4.9 and 4.10 are presented SIMS results for one of the early-grown samples (Sample A) and for a stoichiometric GaN film after optimized growth (Sample B). These results confirm the very high level of carbon present in the bulk film for the initial growths. As can be seen the levels are significantly reduced for Sample B, which means that we have managed to improve the layers significantly. The levels of the impurities are still high but this is due to the polycrystalline nature of the films and these impurities have segregated down the grain boundaries, not incorporated in the bulk crystal [92]. This is evidenced by the levels for oxygen, hydrogen, and carbon all being similar for Sample

B since adventitious hydroxides and hydrocarbons are likely only to be present as monolayers for surfaces freshly exposed to air. Photos of the samples are presented on Figure 4.11a) and 4.11b). The early sample with a high level of carbon is yellow and has a dark edge, while the stoichiometric sample, as expected, is transparent and only a little yellow at the edge (the grey parts are metal deposited on the back of the sample).

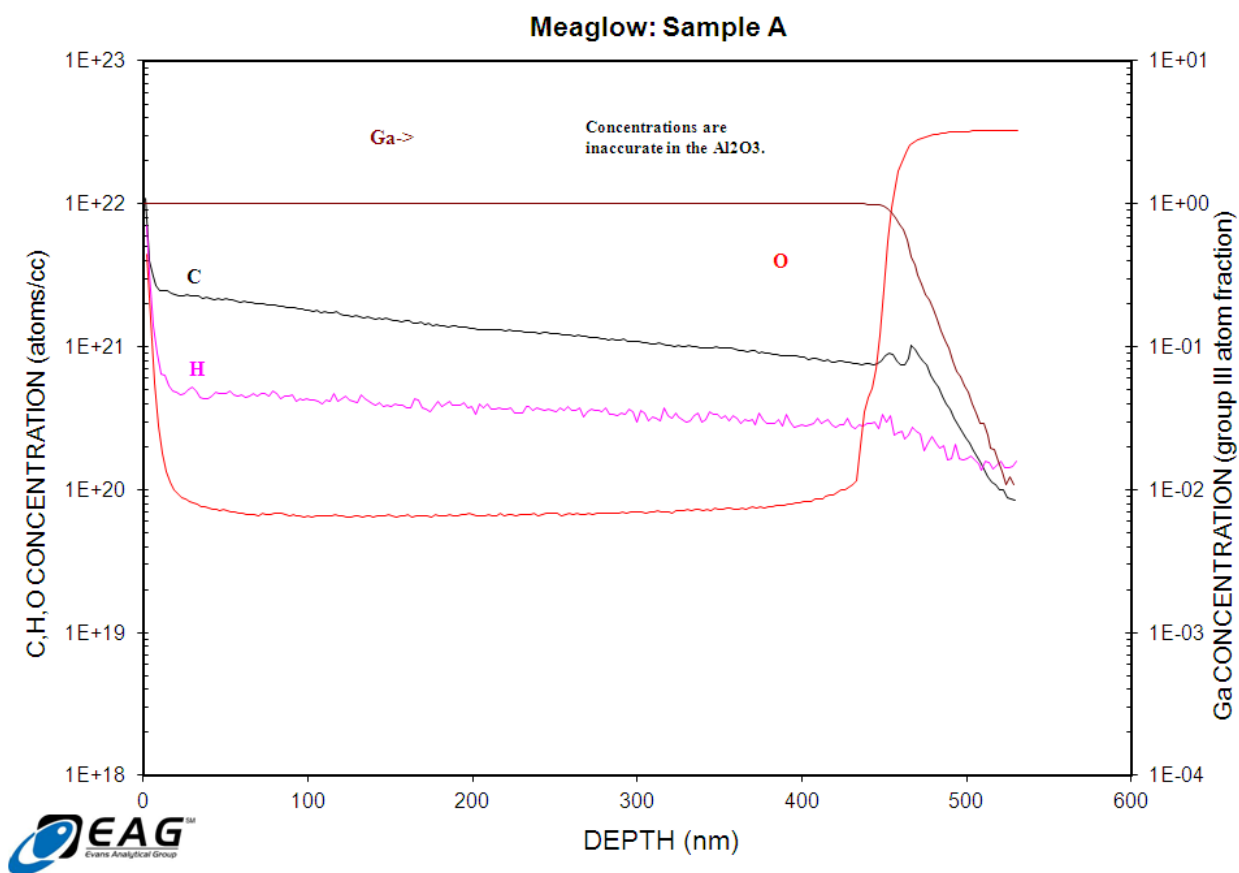


Figure 4.9 SIMS data for an early sample having high concentration of background impurities (Sample A).

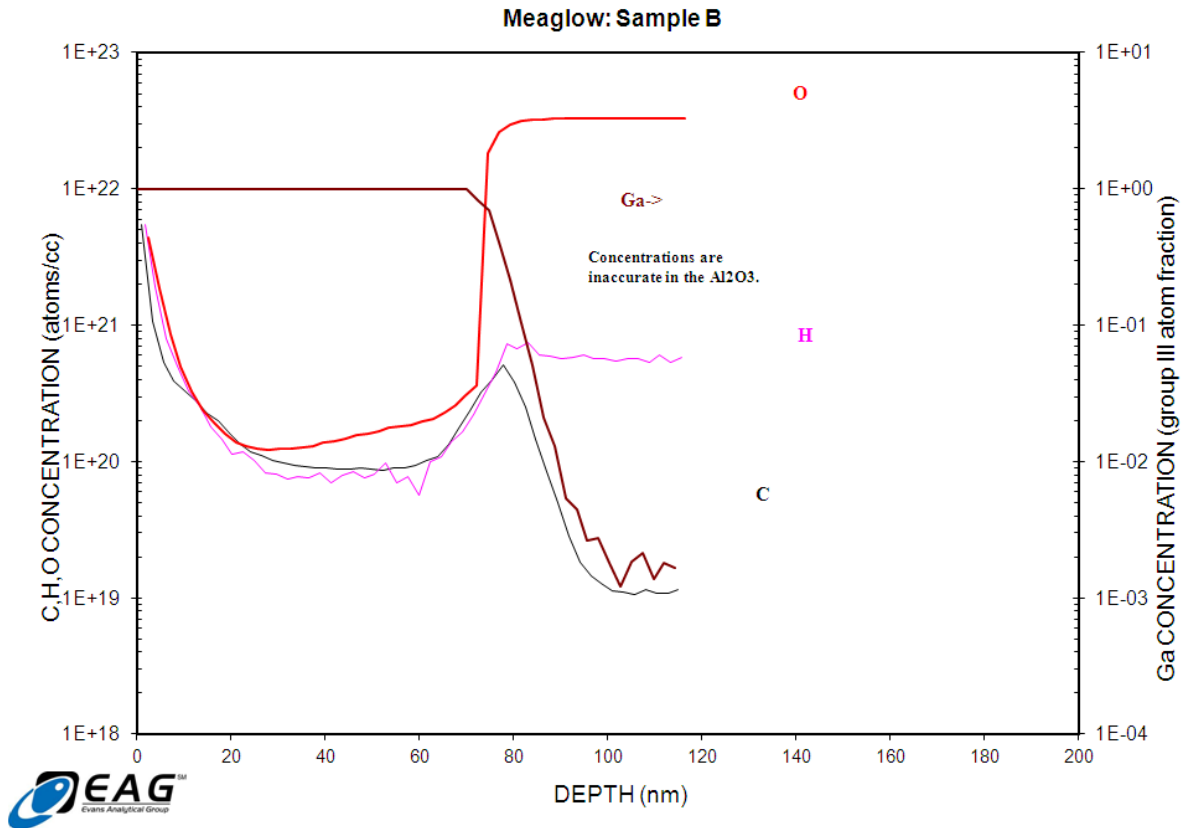


Figure 4.10 SIMS data for more stoichiometric MEAglow GaN layer (Sample B).

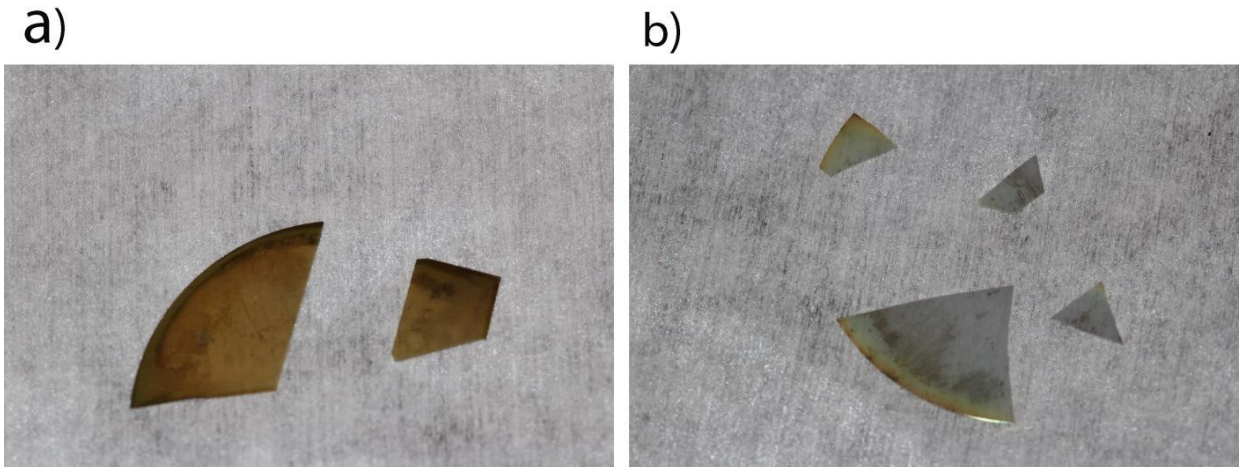


Figure 4.11 a) An early-grown MEAglow sample, b) stoichiometric MEAglow sample

In the subsequent sections more detail will be presented of techniques used to improve the growth conditions aiming towards the achievement of atomically smooth surfaces and improved crystallinity. In Section 4.2 the dependence of the pressure is discussed in terms of finding an intermediate growth regime at 600 °C for achieving good surface morphology. Section 4.3 studies the growth limiting process in terms of deposition per cycle and crystal quality. Further studies have been performed on recrystallization and improved quality of metal rich GaN layers after post-growth annealing experiments in vacuum and air and are described briefly in Section 4.4

#### 4.2 The effect of chamber pressure on the growth of GaN

Migration-enhanced afterglow epitaxy is a new and therefore relatively immature growth method. For this reason several series of experiments were needed to help understand the growth process. In comparison, for a typical MBE system an epitaxial phase diagram has been established for GaN growth which contains three distinct growth regimes that relate the surface morphology of the material to the growth conditions [93]. For that case the authors considered the dependence of Ga flux on temperature. The nitrogen rich regime results in the formation of nitride islands (three dimensional growth) and the Ga droplet regime resulted in the formation of metal droplets. The intermediate regime is the result of growth under slightly Ga-rich conditions which yields the smoothest morphology without the presence of droplets. The intermediate regime was achieved for unmodulated MBE growth at about 700 °C when varying the metal flux [94]. These three regimes were further mapped for growth with the MME method in MBE systems (Figure 4.12) [65]. The authors discovered that they can pulse between the Ga-droplet and N-rich conditions

and still achieve a controllable 2D growth at 500 °C which is shown with b and c arrows on the plot.

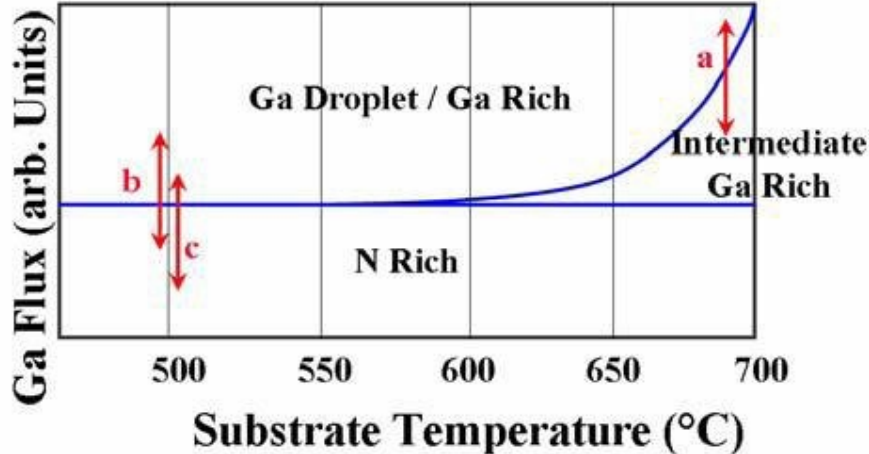


Figure 4.12 Surface phase diagram for MME growth in MBE systems - Phys. Status Solidi C 6, S788 (2009).

In MEAglow MME growth takes place at pressures between 1-10 torr. Since in MBE systems the growth takes place at higher vacuum of  $\sim 10^{-4}$  to  $10^{-5}$  torr, there are practically no gas phase collisions. In the MEAglow reactor, the growth pressure is a lot higher and in order to define similar growth regimes, the pressure dependence had to be further mapped to define the three regimes for certain temperature and gas flow rates. In these experiments we tried to map the pressure dependence to further define the three regimes at temperatures close to 650 °C.

#### 4.2.1 Growth conditions

The studied samples were grown by MEAglow MME under constant growth conditions with the chamber pressure as the only variable parameter. The samples were prepared at about 640 °C. The total growth time was 1028 cycles with cycle length was set to a total

of 10.5 s, with metalorganic flowing in the chamber for 4 s. This pulse length was found in previous experiments to be optimal for higher growth rate. The growth was terminated with a step of 2 hours of nitrogen gas flowing into the chamber in order to prevent the accumulation of particles which were found to condense on the surface from metal redeposition from the reactor chamber walls and other surfaces during cooling. The plasma step terminating the growth was removed because it was found to damage the surface of the layers. The growth conditions for all the experiments are listed in Table 4.4.

Table 4.4 Growth Conditions

Sample ID	Chamber pressure /torr
2012-03-28-2-GaN	1.2
2012-04-10-3-GaN	2.8
2012-04-11-2-GaN	2.0
2012-04-17-1-GaN	2.2
2012-05-25-1-GaN	2.1
2012-05-25-2-GaN	1.9
2012-05-28-1-GaN	1.8
2012-06-06-1-GaN	1.7

The RF plasma source during growth was operated at the maximum power of 600 W in order to generate more active nitrogen species, and the flow rate was kept constant at 1400 sccm. The TMG flow rate was set to 0.8 sccm.

#### 4.2.2 Analysis

The total pressure is an important variable in the growth process. It influences the flux of molecules reaching the sample surface and also the gas phase reactions which occur above the substrate. Increasing the chamber pressure leads to more collisions among the nitrogen active species decreasing their mean free path and ultimately their kinetic energy. Increasing the number of gas collisions also increases the probability of an excited plasma species being de-excited, so that a lower density of active species reach the sample surface. The kinetic theory of gases was used to calculate the number of nitrogen gas collisions to a first approximation. The collision frequency was first calculated by the mean free path of the molecules and their average velocity.

$$\lambda = \frac{kT}{P}; \quad \bar{v} = \sqrt{\frac{8kT}{\pi M}}, \quad (2)$$

where  $k$  is the universal gas constant,  $T$  is the temperature,  $M$  is the molar mass,  $P$  is pressure, and  $N_A$  is Avogadro's number.

The number of gas collisions was found by dividing the collision frequency by the residence time. The residence time was calculated from the gas velocity and the distance between the plasma source and the sample holder. The gas velocity is found from the nitrogen gas flow rate divided by the total area. The total area was calculated from the diameter of the holes of the hollow-cathode plasma source. Since the gas flow rate is given at standard temperature and pressure conditions (in this case set to 1400 sccm), the actual flow rate was adjusted for the different pressures for the studied samples.

$$\dots \quad (3)$$

The dependence of the change in pressure on the deposition per cycle is shown in Figure 4.13, where the number of gas collisions is plotted against deposition per cycle. The data for the sample thickness was obtained by SEM cross-sectional images using a Hitachi SU 70 ultra high resolution microscope.

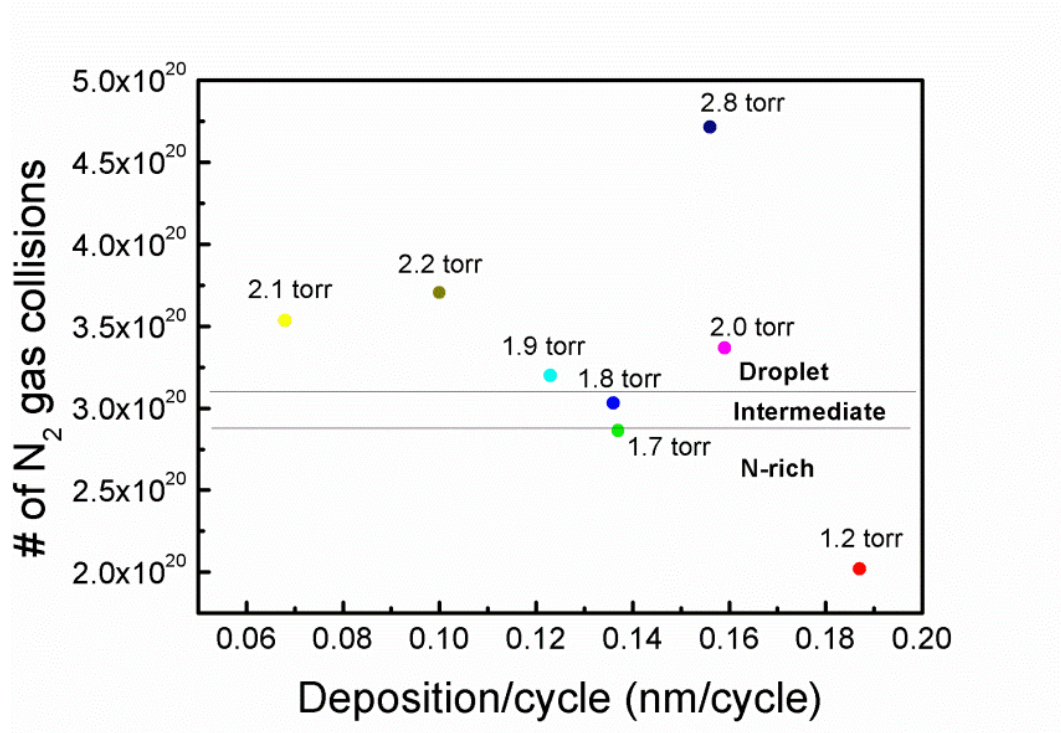


Figure 4.13 Dependence of the GaN layer deposition per cycle on the number of nitrogen gas collisions, with the derived three growth regimes

From the plot it is evident that the deposition per cycle and therefore the growth rate decrease with the increasing number of collisions, which indicates that the metal is not being completely consumed because of the decreasing density of active nitrogen on the surface. The two points of 2.0 torr and 2.8 torr are scatter due to the non-uniformity of the films produced at such high pressure in the Ga droplet regime. The thickness of those

films could not be determined accurately by SEM cross-section micrographs (an example is shown for 2.8 torr sample in Figure 4.18a) below).

The growth regimes are dependent on the initial amount of gallium that is deposited. Too much gallium deposited results in the formation of droplets and the growth is in the droplet regime. When the TMG is off, the conditions start to lean towards the nitrogen rich regime but the metal droplets are hard to consume and sometimes nanowires will form from the droplets [95]. If the initial amount of TMG is insufficient, then nitrogen rich island growth is evident. From these results I have observed that depositing the right amount of TMG initially results in a good wetting layer that can be uniformly nitrided.

The three growth regimes were determined by estimating the surface roughness of the GaN films by AFM. It was found that at a 1.8 torr chamber pressure, a transition between the droplet regime and N-rich regime occurs and an intermediate region was defined where the surface roughness was least. A dependence of the surface roughness on the chamber pressure is plotted on Figure 4.14. As expected from Figure 4.12, the intermediate zone is very narrow at this growth temperature.

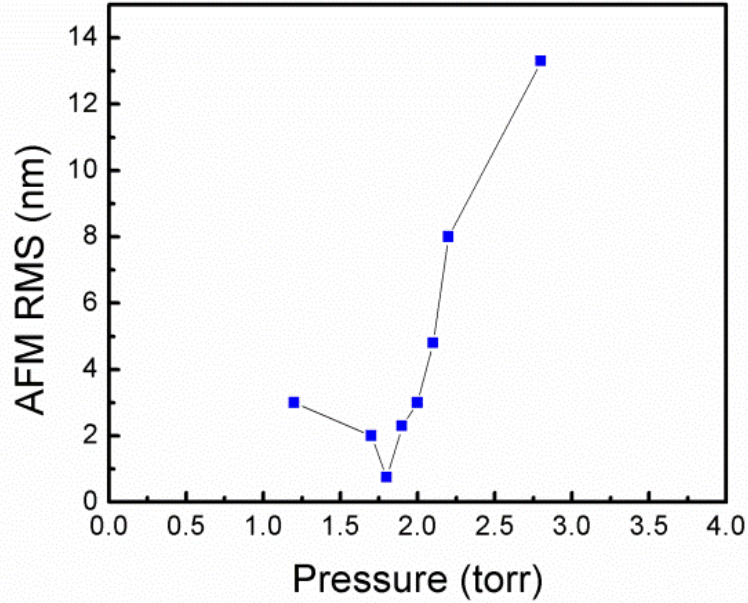


Figure 4.14 RMS surface roughness dependency on pressure. The data points are connected with line just for better following of the trend. The connecting lines are drawn only to show the trend

The roughness of the surface decreases, under nitrogen rich conditions until at 1.8 Torr the intermediate zone is achieved and then the roughness starts increasing with further increases in the total pressure. At higher pressures the excess gallium conditions prevail and the free Ga metal cannot be consumed completely resulting in droplet formation. The different surfaces can be seen in Figure 4.15 and Figure 4.16.

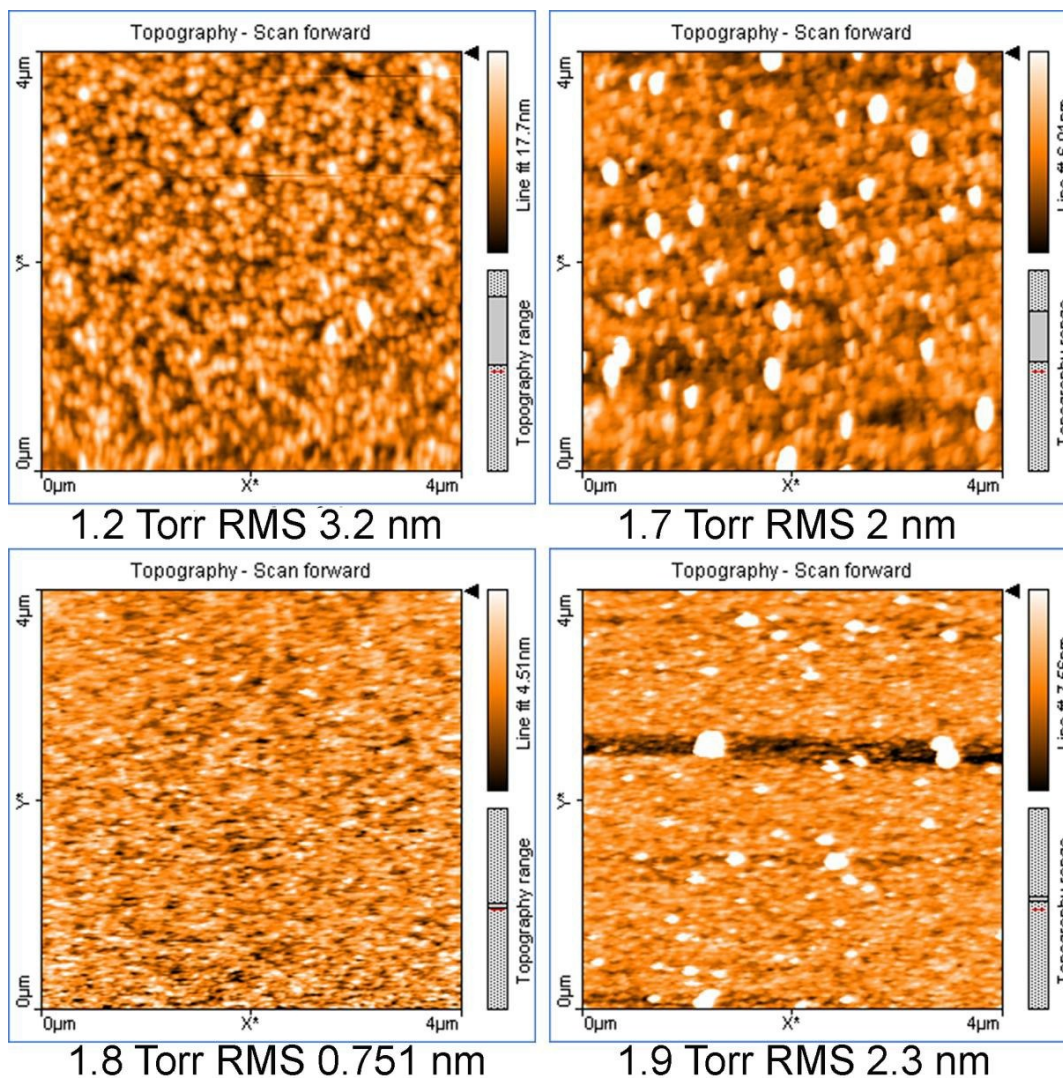


Figure 4.15 AFM surface images for the samples grown under 1.2, 1.7, 1.8, and 1.9 Torr. The RMS surface roughness corresponding to the sample grown at particular chamber pressure, is shown below each image.

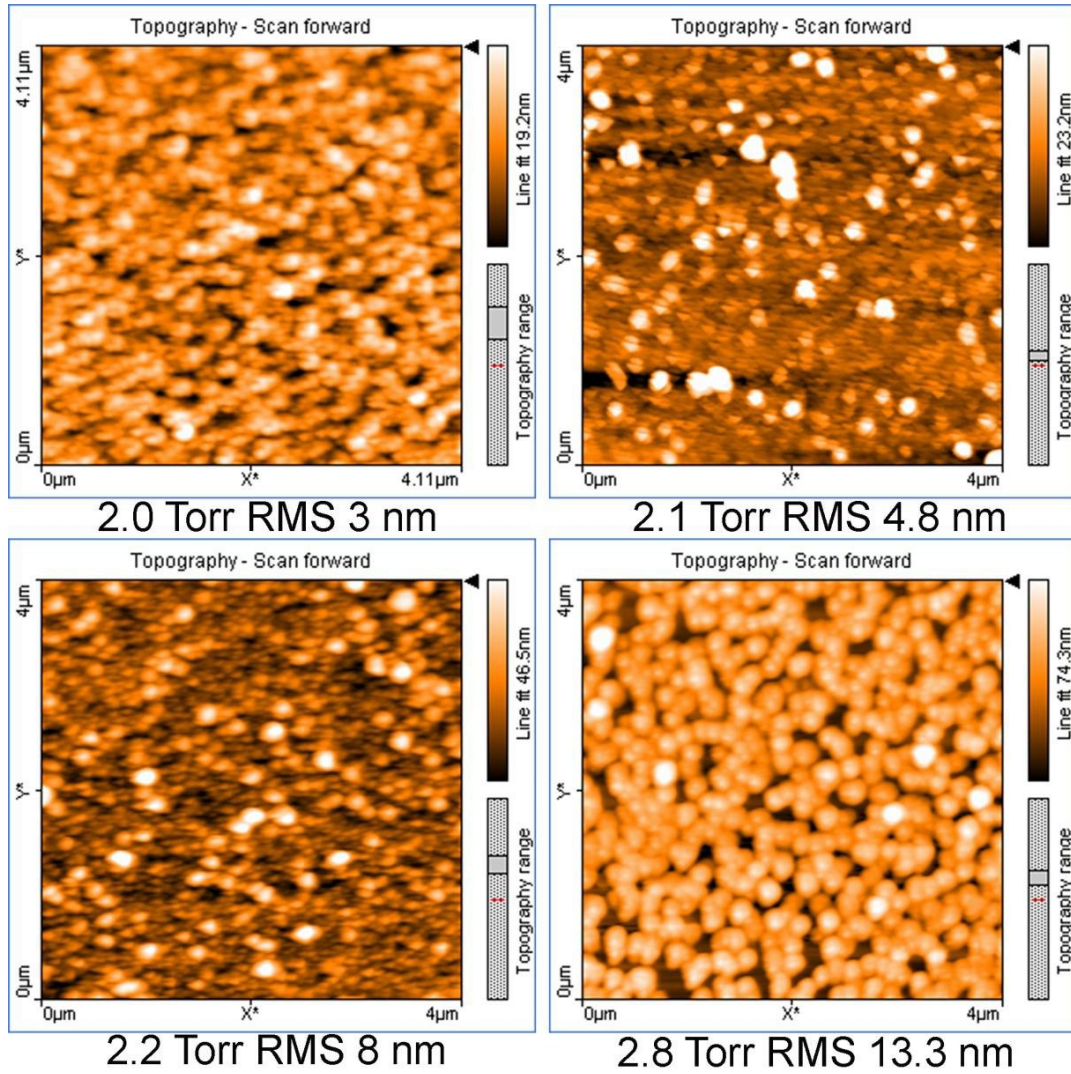


Figure 4.16 AFM surface images of the samples grown under 2.0, 2.1, 2.2, and 2.8 Torr. The RMS corresponding to the sample grown at particular chamber pressure, is shown below each image.

Further, the TMG bombardment rate was calculated in order to get the approximate amount of gallium that reaches the surface. The bombardment rate is entirely pressure dependent and can be calculated from the Knudsen equation:

$$\text{---} \text{---} \quad (4)$$

where  $\bar{v}$  is the average gas velocity and  $V_m$  is the molar volume, calculated from the ideal gas law. In this work the gas temperature was taken to be 300 K for simplicity, though for later work a thermocouple was placed in the MEAglow system above the sample holder to measure the gas temperature more accurately.

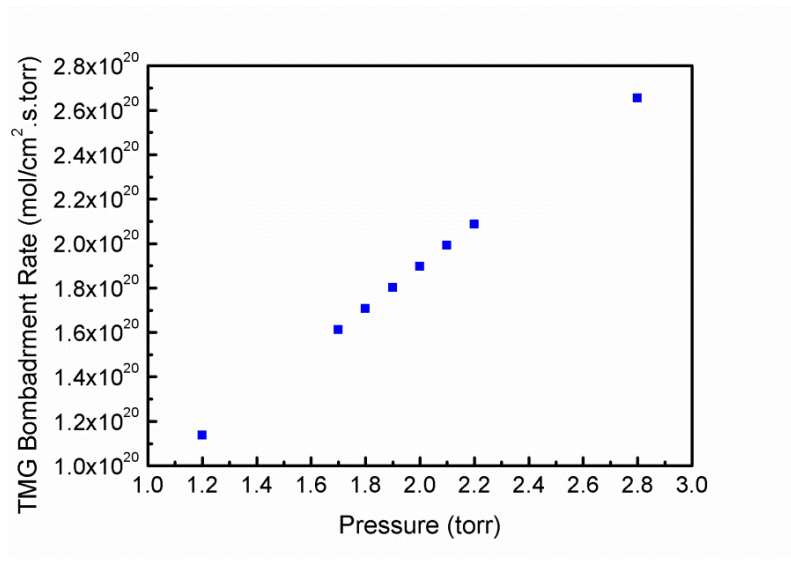


Figure 4.17 TMG bombardment rate dependence of pressure.

The bombardment rate is plotted on Figure 4.17 against the growth pressure. It is evident from the plot that the amount of gallium atoms bombarding the surface increases with the total pressure. At 1.8 torr  $1.7 \times 10^{20}$  molecules of trimethylgallium hit the surface per second which, in part (along with dissociation probabilities), determines the thickness of the gallium layer. The SEM cross-section images for the two extreme conditions of the pressure variations are shown on Figure 4.18a) and 4.18b).

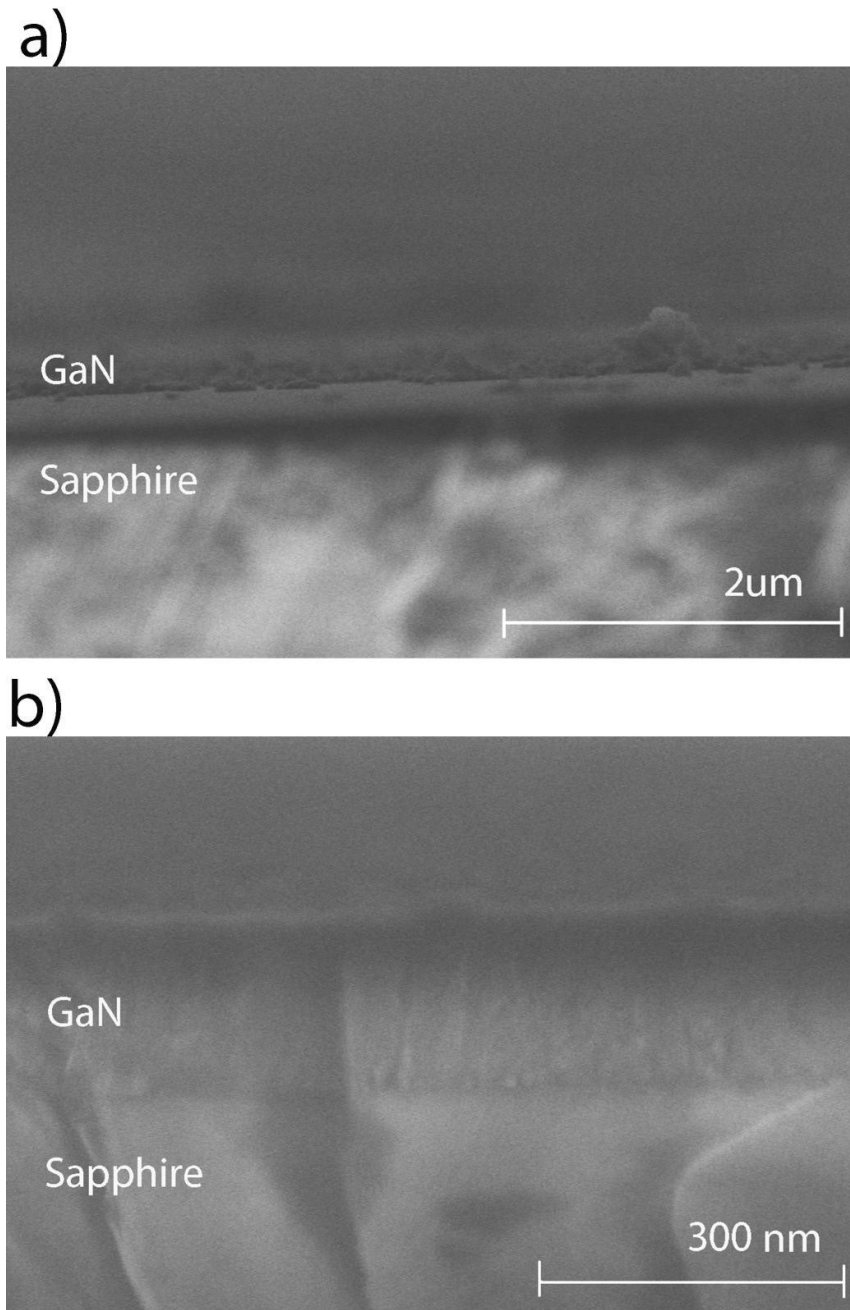


Figure 4.18 GaN grown under a) 2.8 Torr chamber pressure and b) 1.2 Torr chamber pressure

From the above pictures it can be seen that the sample with the highest pressure is very non-uniform and consists of very high features and holes, which is also confirmed by the optical transmission measurement, presented in Figure 4.19. The sample grown under the

lowest pressure shows the largest thickness for the series because more gallium is consumed as soon as it reaches the surface. The two samples show a very big difference in their visual appearance. The 2.8 Torr sample is very transparent making almost no difference with the sapphire, while the 1.2 Torr sample looks yellow. The rest of the samples show the trend that the yellow discolouration begins to disappear with the increasing pressure, which may be an indicator that damage is being caused by the plasma species under low chamber pressure conditions, resulting in defects with yellow colour centres.

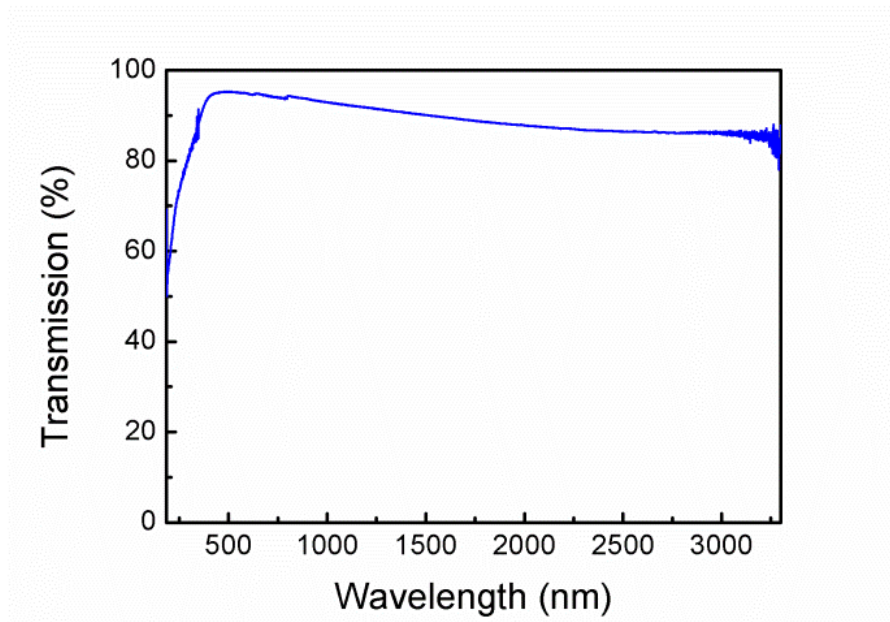


Figure 4.19 The non-uniformity of the GaN layer grown at 2.8 Torr is evident from the optical transmission spectrum.

The crystal structure of the GaN layers was investigated by X-ray diffraction and optical transmission. The scans of the samples are plotted on the same scale for comparison. The GaN grown under 1.8 torr has XRD peak position of  $34.601^\circ$  and is

closest to the accepted position of (0001) GaN, while positions for the rest of the samples look scattered from  $34.457^\circ$  to  $34.582^\circ$ , all much lower values. The peak of the sample grown under the lowest pressure of 1.2 torr is located at the lowest angle position. The FWHM varies from  $0.167^\circ$  to  $0.225^\circ$  and the broadening is affected by the strain, thickness, and grain size. The XRD spectra are given in Figure 4.20.

The band-gap energies and the maxima of optical density squared are listed on Table 4.5 for comparison. It can be seen that the sample grown under 1.8 torr has an energy band-gap of 3.32 eV which in comparison to the others samples from the series is closest to the 3.4 eV band-gap of GaN.

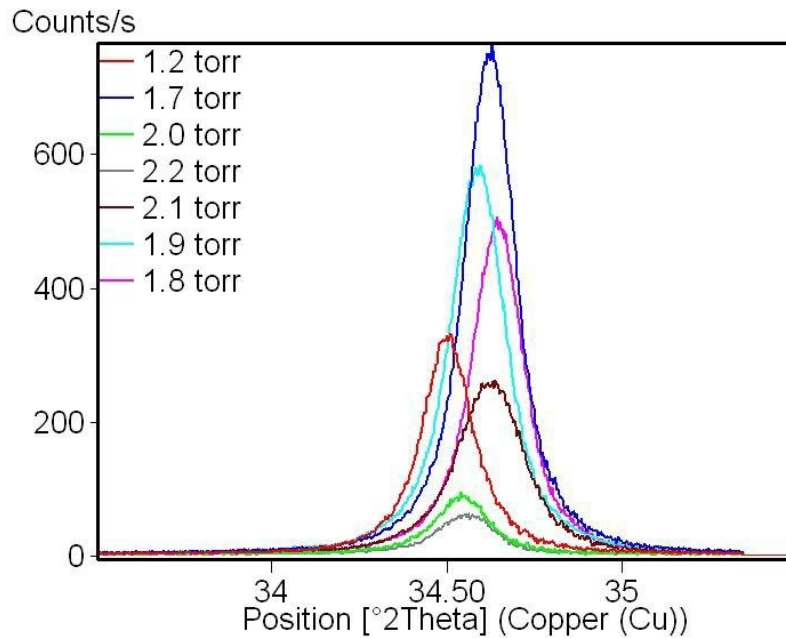


Figure 4.20 X-ray diffraction spectra of the studied samples.

Table 4.5 Energy Bandgap obtained by optical transmission

Sample ID	Energy Bandgap /eV
1.2 Torr	3.27
1.7 Torr	3.13
1.8 Torr	3.32
1.9 Torr	3.27
2.0 Torr	3.19
2.1 Torr	3.09
2.2 Torr	3.04
2.3 Torr	-

The bandgap energies from the optical transmission spectra for all the samples are lower than the bandgap for GaN which indicates the presence of defect levels. In Figure 4.21 are plotted the values of the energy bandgap of the studied GaN samples against the value of the c lattice constant obtained from the XRD spectra. The errors estimated from the XRD peak positions for the lattice constant are  $\pm 0.001 \text{ \AA}$ , and the error from the extrapolation of the linear part of the optical density squared is  $\pm 0.02 \text{ eV}$ . From the plot is evident that the values of the c lattice constant for the samples grown at 1.8, 1.7 and 2.1 torr are closest, though a little lower than the reported value for GaN of  $5.185 \text{ \AA}$ . The rest of the values are higher than the reported value. The XRD peak position of 2.1 torr could be due to a larger strain, as it had the largest FWHM of  $0.225^\circ$ . The data in Figure 4.21 shows a general common trend among all the samples that as the energy bandgap decreases, the c lattice constant increases, however there is a large scatter in the data, which suggests multiple effects are in play. These may include native defect or impurity

incorporation, plasma damage, and sample thickness variation (which strongly influences strain).

The shift in the energy bandgap to lower energies, accompanied with a large increase of the c lattice constant in MEAgrow grown GaN samples is typically observed in more metallic samples. The dependence for some of these very Ga-rich samples is shown in Figure 4.22. These three samples, presented in Figure 4.22, were grown under identical conditions, and only the flow rate of the TMG was decreased systematically. As can be seen with decreasing amount of gallium, the energy bandgap increases and the c lattice constant decreases.

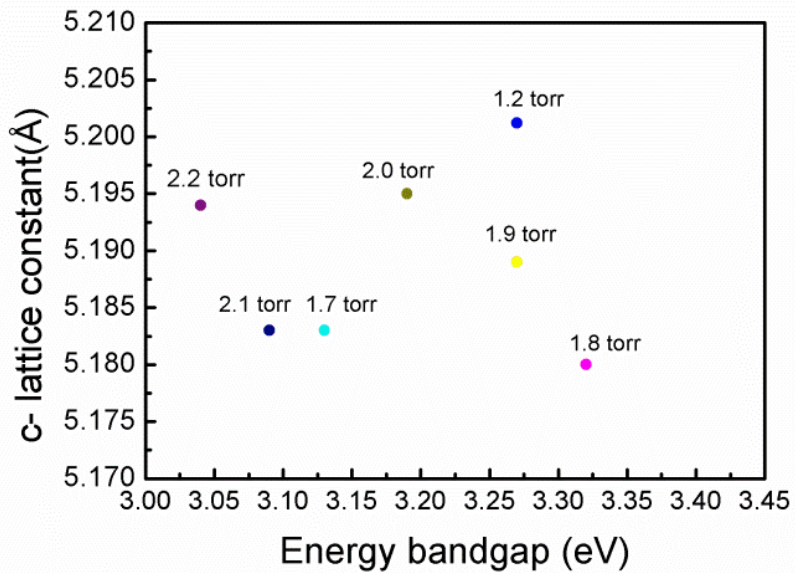


Figure 4.21 The Energy bandgaps of the GaN samples grown at various chamber pressures versus the c lattice constant.

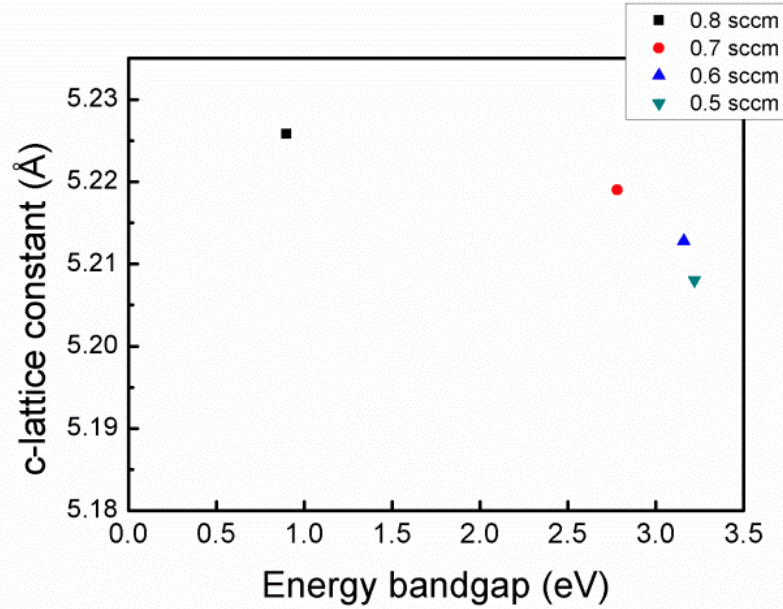


Figure 4.22 The dependence of c lattice constant versus the absorption edge for Ga-rich MEAgrow GaN.

All the GaN layers grown under different pressure conditions retained their semi-insulating character and high level of compensation and therefore it can be inferred that the level of the background impurities was still high, particularly carbon which is known to cause compensation in GaN and is used in the production of semi-insulating GaN.

These results suggest that the grown GaN films are still far from stoichiometry even when optimal growth conditions were obtained for pulsing in an intermediate growth regime, which can provide very smooth surfaces. The results indicate that further improvement of the growth conditions is needed to achieve better stoichiometry and crystalline quality.

#### 4.3 Study of the growth rate limiting processes for MME MEAgrow grown GaN

The influence of the three growth regimes, identified in the Figure 4.12 above, on the growth rate by modulation of the pulses time intervals was investigated further for

MEAglow GaN samples grown at 640 °C. As the MEAglow growth process occurs in a CVD environment, the pulse modulation cannot be controlled in-situ with RHEED, as is the practice for MME growth in an MBE system. This leads to the need for a better understanding of the growth limiting processes in order to achieve improved control and reproducibility of the applied MME method.

The pulse modulation was studied by examining six samples that were grown under similar conditions at 640 °C. The samples were grown with 1700 sccm and 0.8 sccm nitrogen and TMG flow rates, respectively, under pressure of 1370 torr. A metal grid was placed above the sample holder to shield the sample surface from more energetic plasma species, such as positively charged ions. The grid can be biased optionally but in this study it was set to 0 V.

The variation of the pulse length was balanced by the total number of cycles in such a way that kept the total growth time constant. In this way it was possible to monitor the variation of the growth rate and its limiting growth regimes. The variation of growth conditions and the change in the growth rate are shown in Table 4.6

Table 4.6 Variable growth conditions

Sample ID	TMG On (s)	TMG Off (s)	Cycle length (s)	Number of cycles	Total growth time (s)	Deposition/cycle (nm/cycle)
Sample 1	4	6.5	10.5	1714	18000	0.140
Sample 2	4	8	12	1500	18000	0.153
Sample 3	4	10	14	1285	18000	0.155
Sample 4	6	12	18	1000	18000	0.220
Sample 5	8	16	24	750	18000	0.230
Sample 6	7	14	21	857	18000	0.248

The properties of the studied samples were examined by AFM, XRD, SEM, and optical transmission spectroscopy. The results from these measurements are listed in Table 4.7

Table 4.7 Properties of the GaN layers grown under the conditions listed in Table 4.6

Sample ID	AFM RMS (nm)	E <sub>g</sub> (eV)	XRD Intensity (cps)	XRD FWHM (degrees)	Deposition/cycle
Sample 1	2.1	3.2	340	0.21	0.140
Sample 2	1.5	3.25	580	0.168	0.153
Sample 3	1.3	3.25	370	0.136	0.155
Sample 4	1.3	3.32	820	0.124	0.220
Sample 5	3.9	3.2	2200	0.11	0.230
Sample 6	3	3.27	5000	0.117	0.248

Sample 1 resulted in dark layer, having a low energy bandgap of 3.2 eV. This slightly dark colouration suggested that the sample was metal rich and the nitridation was insufficient to consume the metal layer. This metal build-up impeded the growth rate and the limiting process for the growth rate was strongly Ga-limited. This was confirmed by the second experiment with the results for Sample 2. After increasing the pulse length for only nitridation from 6.5 s to 8 s for Sample 2, the resultant bandgap increased to 3.25 eV and the AFM rms dropped down to 1.5 nm from 2.1 nm, suggesting a transition from droplet regime to an intermediate regime. Further increase of the length for the nitrogen only pulse didn't increase the growth rate much suggesting that it was strongly limited by insufficient gallium. From these three growths (samples 1-3), a duty cycle with the intermediate growth regime under slightly Ga-limited conditions was determined. A duty cycle represents the ratio between the TMG pulse length and the total cycle length.

Taking the duty cycle from Sample 2 excluded the extreme Ga-limiting and nitrogen-limiting conditions and then was kept constant for the subsequent three growths while varying the total cycle length. The limitations of the growth rate were determined from the overall analysis of the energy bandgap, the rms surface roughness, the XRD spectra, and were based on experience gained from the previous growth series. For instance, the metal droplet regime was characterized by the decrease in the energy bandgap, poor XRD spectra, and larger rms surface roughness than the RMS of a GaN layer grown in the intermediate regime. When the growth rate was limited by the nitrogen rich regime, roughening of the surface was observed. Unfortunately, not much detail of the grain structure was seen from the SEM cross-sectional images due to the semi-insulating character of the layers and the resulting charging effect. This led to difficulty in determining the crystal size. A plot of the duty cycle against the deposited GaN layer per cycle is shown in Figure 4.23.

As the total cycle length increased again for Sample 4, keeping the same duty cycle, the growth rate increased and the limiting process was again slightly gallium limited as evidenced by a decrease in the AFM rms and an increase in the energy bandgap. As the deposition per cycle approached a monolayer per cycle (0.259 nm/cycle), the quality of the films increased, which is evident from the data in Table 4.7. Sample 5 resulted in much rougher surface, indicating the slight transition to N-rich regime, but the XRD results were again better than the previous sample. The pulse length was decreased for Sample 6 and again a transition to slightly Ga-rich regime occurred, as evidenced by the decrease in the surface roughness and increased energy bandgap.

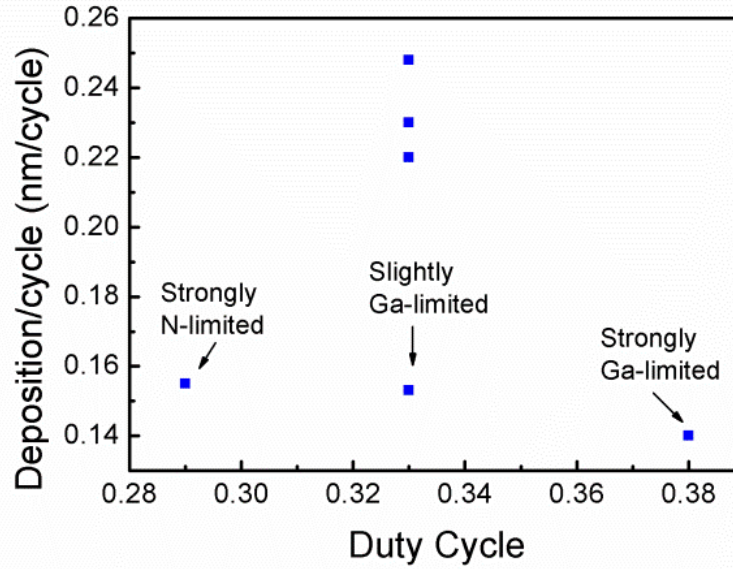


Figure 4.23 The determined duty cycle for growth in the intermediate regime showing increased growth rate.

#### 4.4 Improvement of GaN MEAGlow polycrystalline films after annealing

A polycrystalline GaN sample was studied for possible changes in the crystalline structure after annealing in air. The sample was chosen to be very non-stoichiometric and the growth conditions were exactly the same as for Sample 2 in Section 4.1. It was grown on a 2'' sapphire wafer. Under these conditions semi-insulating GaN was obtained having high levels of background impurities and free gallium metal, (as was confirmed by the XPS measurements in Section 4.1).

Previous studies on low temperature grown polycrystalline GaN have shown that it can recrystallize and improve its quality after post-growth annealing at temperatures below the growth temperatures (570 °C in the reference) [96].

The annealing procedure for the MEAglow sample was to first heat the sample in air to 650 °C for one hour. This temperature was close to the deposition temperature. The sample was taken for measurements and annealed subsequently for one additional hour at the same temperature. The third annealing was performed at lower temperature 600 °C for 1 additional hour. The whole wafer of the sample was annealed in series, rather than few pieces in parallel, in order to get more accurate results, as the grown GaN was non-uniform.

After the first annealing a noticeable conversion of the edges of the wafer to amorphous oxide occurred but the centre of the sample remained unaltered. The energy bandgap after each anneal kept increasing as is evident from the shift in the absorption edge to higher energies in the optical absorption spectra. The samples were measured in the centre where there was no visual evidence for a conversion to gallium oxide but the shift in the absorption edge to higher energies may be due to a contribution from amorphous  $\text{Ga}_2\text{O}_3$  forming, as the c lattice constant didn't change to the lower values expected for a more stoichiometric material with the annealing (Figure 4.24a)). Oxygen tends to segregate mainly on the grain boundaries [92], and a change in the lattice constant is not expected to be observed but its contribution could be observed from the optical transmission spectra. The presence of amorphous oxide in the optical absorption spectra of GaN was previously studied in [78]. From the XRD spectra presented on Figure 4.24a), can be seen that the GaN layers showed a slight improvement in the peak intensity and FWHM. This can be due to freeing of some of the incorporated excess metal, as it becomes mobile and can move to the surface and bond with oxygen. Gallium is liquid at only 25 °C and may therefore be very mobile at high temperature. Such a mobility can be a possible

explanation for the complete transition of GaN around the edge of the sample to gallium oxide, as the GaN layer was non-uniform and more metal had incorporated around the edge during growth due to the temperature gradient between the sample holder and the substrate surface.

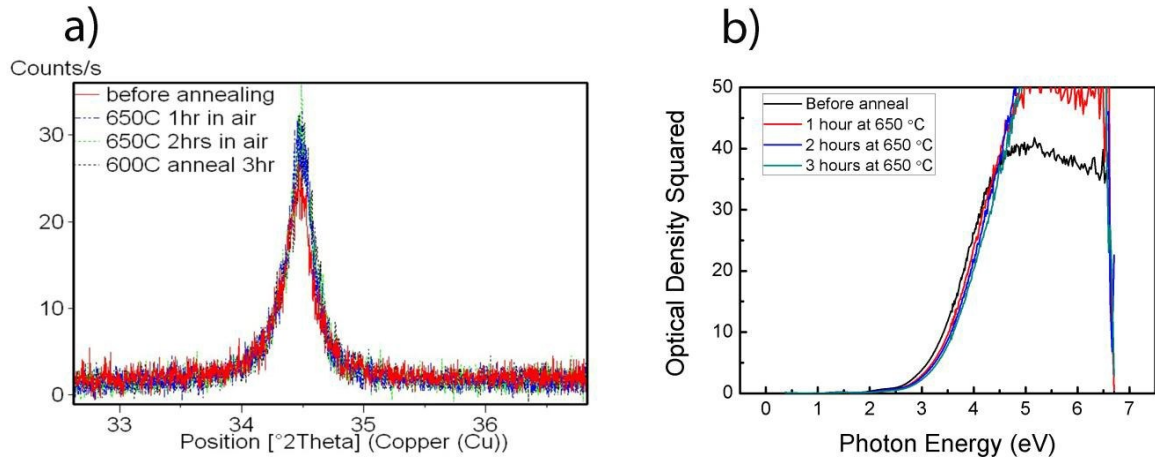


Figure 4.24 a) A comparison between the X-ray diffraction spectra after each annealing procedure, and b) comparison between the optical absorption spectra.

In this chapter the optimization of the growth conditions for MEAglow GaN samples towards the achievement of better quality stoichiometric layers was discussed. An elemental analysis was performed which revealed a high density of background impurities possibly incorporated due to the incomplete thermal dissociation of the metalorganic precursor. A method for mapping the surface phase diagram related to growth in MBE systems to the conditions of MEAglow reactor was presented. As a result conditions were found for growth of GaN layers with very smooth surfaces and better stoichiometry. The growth limiting regimes in metal pulsed modulation growth were studied. The annealing of very metal rich GaN samples was also studied for improvement of the crystallinity and a slight improvement of the crystallinity was observed possibly

due to the diffusion of free gallium metal. However, further annealing experiments and characterization are needed to confirm the results from the annealing studies.

## Chapter 5. Growth of InN by MEAgrow

### 5.1 Introduction

In this chapter the growth and properties of various InN layers produced by MEAgrow are studied. The chapter is divided into three parts. The first part presents a detailed description of the growth process and the optimized growth conditions used for the production of stoichiometric epitaxial layers on various buffer layers. Amorphous gallium oxide buffer layers, commercial GaN templates, and sapphire were used as the substrate layers for the high quality films and their impact on the crystalline quality of InN is investigated. The third part is focused on the thermal stability of nitrogen rich MEAgrow polycrystalline InN samples grown at low temperatures.

### 5.2 InN grown by MEAgrow

The development of InN has gained a great interest in the recent years mainly due to the advances in the InGaN alloy and its use in the commercial production of light-emitting diodes. However, InN is considered as the least understood of the group III-nitride binaries because of the challenges related to its epitaxial growth. Although a considerable progress has been made in this respect in the past decade and high quality films have been reported for various growth techniques, some inherent material properties such as the large disparity between the size of the indium and nitrogen atoms, high nitrogen vapor pressure, and the lack of the lattice matched substrates, complicate the growth process and the technology is not mature yet for its commercial application in device structures. The low dissociation temperature of InN requires growth at relatively low temperatures compared to other group III nitrides. The low temperature growth results in reduced

surface mobility of the adatoms which can cause island growth and decreased crystal quality. For this reason the migration-enhanced epitaxy technique is commonly used for InN film growth [63,97,98]. The advantages of the MEE and MME methods were described previously in Chapter two. All the epitaxial layers described here, in the first two sections of this chapter, were grown by using the metal modulated method. The results for these state-of-the-art layers were published in [99].

### 5.2.1 Substrate preparation and growth conditions

Growth of InN was attempted on sapphire substrates, on 2  $\mu\text{m}$  commercially available MOCVD GaN grown on sapphire, and on thin  $\text{Ga}_2\text{O}_3$  layers produced on top of a sapphire substrates. The c-plane sapphire wafers were heated to 1050  $^\circ\text{C}$  for 6 hours in air prior to growth to reduce the damage caused by polishing. The GaN templates were etched in  $\text{HCl}:\text{H}_2\text{O}_2$  (1:1) solution before growth to remove the thick surface oxide that is usually present in MOCVD grown films.

Few nanometers thick  $\text{Ga}_2\text{O}_3$  having different surface roughnesses, formed on c-plane sapphire, were also used for the InN growth. The thin  $\text{Ga}_2\text{O}_3$  layers were produced by annealing approximately ten nanometers semi-insulating GaN layers at 1050  $^\circ\text{C}$  for 1 hour in air. This was then etched in  $\text{HCl} : \text{H}_2\text{O}$  (1 : 1) solution. The GaN layers were grown at approximately 660  $^\circ\text{C}$  by the MEAgrow technique using the MEE method on top of a c-plane sapphire substrate.

All the substrate were additionally prepared in the MEAgrow system immediately prior to the growth process. They were heated to 550  $^\circ\text{C}$  under constant nitrogen flow for 2 hours, followed by a nitridation step for 1 minute at a pressure of 750 mTorr. The nitridation of sapphire was found to produce a thin AlN layer on the surface which helps improving the

crystal quality of the subsequent layer [100]. During the nitridation step the plasma source was operated at lower power (100 W) of 13.56 MHz RF power and 1000 sccm nitrogen flow rate.

The MME technique was applied for the growth of the InN layers. The nitrogen plasma was kept on continuously during growth and trimethylindium (TMI) was pulsed in the chamber for 10 s followed by an interruption of 10 s with only plasma used to consume the metal layer.

The optimal growth conditions used for the epitaxial layers were achieved after an increase of the chamber pressure to 1 Torr from 500 mTorr used in the previous runs. This led increased rate of nitrogen gas collisions (see Chapter X, Section X for GaN), so that the more energetic plasma species were quenched and less damage of the growing layer was caused from the plasma. For these conditions the TMI flow was set to 0.6 sccm and the RF plasma source was operated at 500 W with a nitrogen flow rate of 600 sccm.

The surface morphology of the InN layers was examined by atomic force microscope and scanning electron microscope. Two different x-ray diffractometers were used for studying the crystalline structure of the layers. A PANalytical X'Pert Pro MRD diffractometer was used for the routine  $\omega$ - $2\theta$  scans and a high resolution x-ray commercial diffractometer (GE Inspection Technologies) was used for the high resolution x-ray rocking curve  $\omega$ -scans that were performed on the InN layer grown on Ga<sub>2</sub>O<sub>3</sub> buffer layer. The optical transmission measurements were performed with a dual beam Varian Cary 5E UV-Vis-NIR spectrophotometer operating in the wavelength range of 175 – 3300 nm. The electrical properties for some of the samples were obtained from Hall effect measurements by the Van der Pauw method at room temperature.

The growth rate was about two orders of magnitude higher in comparison to atomic layer deposition (ALD). It was observed that the quality of the layers was best when the deposition cycle was closer to 2 monolayers.

### 5.2.2 InN grown on Ga<sub>2</sub>O<sub>3</sub> buffer layer

In this section the growth of InN layers on very thin gallium oxide interlayers is presented. A study was done on the influence of the roughness of the buffer layer surface on the crystal quality of the subsequent InN layer.

The InN layers that had the best quality over the rest of the grown samples on Ga<sub>2</sub>O<sub>3</sub> were achieved on very smooth Ga<sub>2</sub>O<sub>3</sub> surface. AFM images of the surfaces of the underlying oxide layer and the InN layers grown on top of it are shown in Figure 5.1. The coalesced crystallites of the InN film are evident from the AFM image (Figure 5.1a). This layer measured an RMS surface roughness of 4.7 nm over an area of 4x4 μm, whereas the underlying gallium oxide buffer layer shown in Figure 5.1b) measured RMS surface roughness of 0.5 nm.

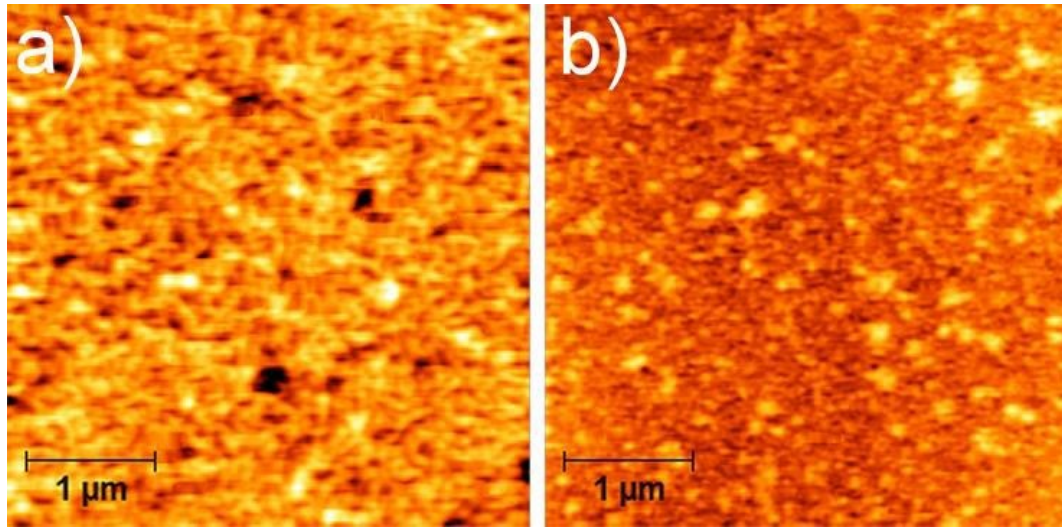


Figure 5.1 AFM surface images of: a) the surface of the InN layer grown on top of  $\text{Ga}_2\text{O}_3$ . The RMS surface roughness is 4.7 nm; b) the surface of the  $\text{Ga}_2\text{O}_3$  layer. The RMS surface roughness is 0.5 nm.

The surface of the InN was further examined with SEM to confirm the observed coalescence in the AFM images. Figure 5.2 shows the SEM micrographs of surface 5.2a), and the cross-sectional image 5.2b) of the same InN layer. Large crystallites that have coalesced and formed a continuous layer are evident from Figure 5.2, although the grain boundaries are still evident with some pits present on those sites. The sample thickness was determined from the SEM cross-section image to be 170 nm. The crystal structure was examined by  $\omega$ - $2\theta$  scan for which the spectrum is presented in Figure 5.3. The peak for InN was present at  $2\theta = 31.34^\circ$ , which indicates a c-axis oriented crystal and the full width at half maximum was estimated to be 403 arcsec.

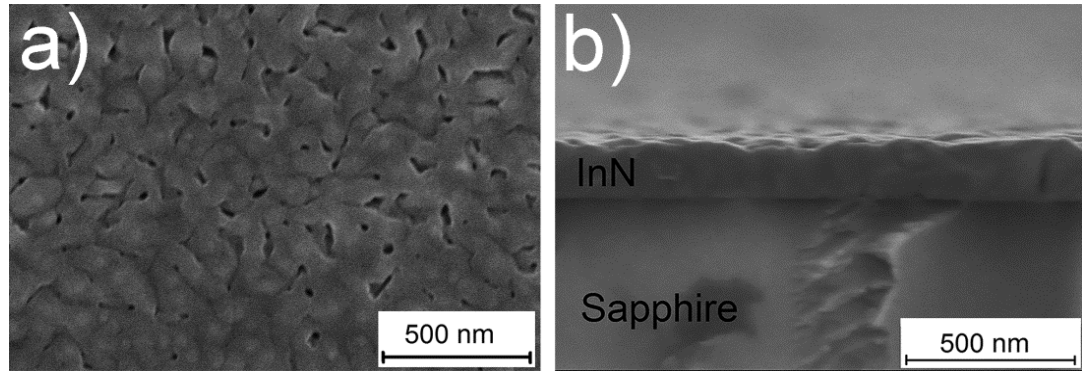


Figure 5.2 SEM micrographs of InN grown on top of the thin  $\text{Ga}_2\text{O}_3$  buffer layer, showing: a) surface image, and b) cross-section of the 170 nm thick InN layer grown on the  $\text{Ga}_2\text{O}_3$  buffer layer.

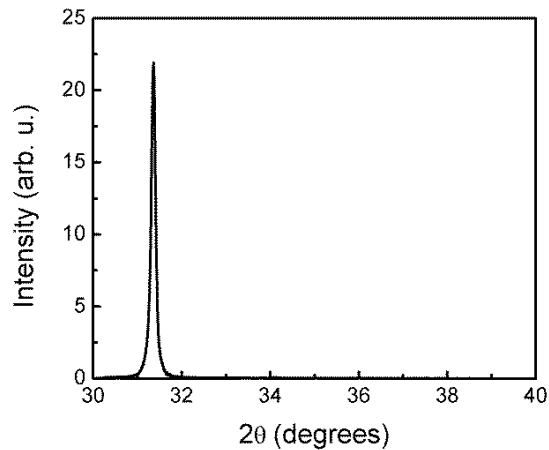


Figure 5.3 X-ray diffraction  $\omega$ - $2\theta$  scan for InN grown on the  $\text{Ga}_2\text{O}_3$  layer, showing no evidence of In metal peak at  $33.1^\circ$ .

The high resolution x-ray rocking curve scan ( $\omega$ -scan) was performed on this sample in order to assess the crystalline quality and a FWHM of 2560 arcsec was determined for the (002) Bragg reflection while a value of 2710 arcsec was observed for the (104) asymmetric Bragg reflection. These values are consistent with a coalescing single crystal material. For comparison, InN layers grown on 2 nm thick AlN buffers by Lu et al. [97]

had values of the (002) rocking curve of 2598 arcsec, and 1466 arcsec were achieved by the same group for InN layers grown on much thicker 120 nm AlN buffer layers. No asymmetric reflections were reported in ref. [97] for the samples grown on thin AlN buffer layers, as in their case RHEED and AFM clearly indicated polycrystalline material with no evidence of coalescence. They needed much thicker buffer layers to achieve comparable crystal quality with the layers grown on very thin Ga<sub>2</sub>O<sub>3</sub> by the MEAgrow technique.

The underlying oxide layer was insulating which allowed Hall effect to be performed to obtain the carrier concentration and the mobility for the InN film. A high electron concentration of  $1.3 \times 10^{20} / \text{cm}^3$  and mobility of  $150 \text{ cm}^2 / \text{V} \cdot \text{s}$  were measured at room temperature. Previous studies show that for high carrier concentrations there is no dependence on the crystal quality, instead the incorporation of point defects appears to be the dominant effect [101]. The very high mobility for such a high electron concentration implies that the crystal quality is relatively good. A comparison can be made to Figure 4 of Lu et al. [63]. Our sample sits more than an order of magnitude in mobility for such a high electron concentration. The sample grown on the gallium oxide is also very thin, it is well known that InN quality improves with thicker growth [102]. Thicker growth was attempted by doubling the growth time but more accurate temperature control was needed to achieve good quality layers as sapphire is transparent to infrared while InN absorbs and with the increasing InN thickness, the temperature for the growing surface increases.

The absorption edge was determined from optical transmission spectroscopy for both the oxide interlayer and the InN layer by extrapolating the linear part of the absorption coefficient squared with the x-axis intercept [77]. On Figure 5.4a) is presented the

absorption spectrum plot from which the absorption edge of the InN was found to be 1.38 eV. On the optical transmission spectrum, presented on Figure 5.4b) there was no evidence for free electron absorption in the infrared region which is very unusual because the sample had a very high carrier concentration. Free electron absorption is normally present when there is a Moss-Burstein effect. That it is absent in this spectrum indicates that the bulk of the material does not have the strong Moss-Burstein effect which is expected for samples with such a high carrier concentration. Therefore, the high background electron concentration measured by the Hall effect for this particular sample may be due to higher conductivity regions near the substrate interface and/or the surface electron accumulation layer, as has been shown by others [103]. Because the InN layer is so thin, these interface and surface effects may dominate the measured carrier concentration so that the bulk value is actually somewhat lower than the measured value. It appears that the bulk carrier concentration is substantially lower, which may provide an explanation for the relatively high electron mobility seen for this sample.

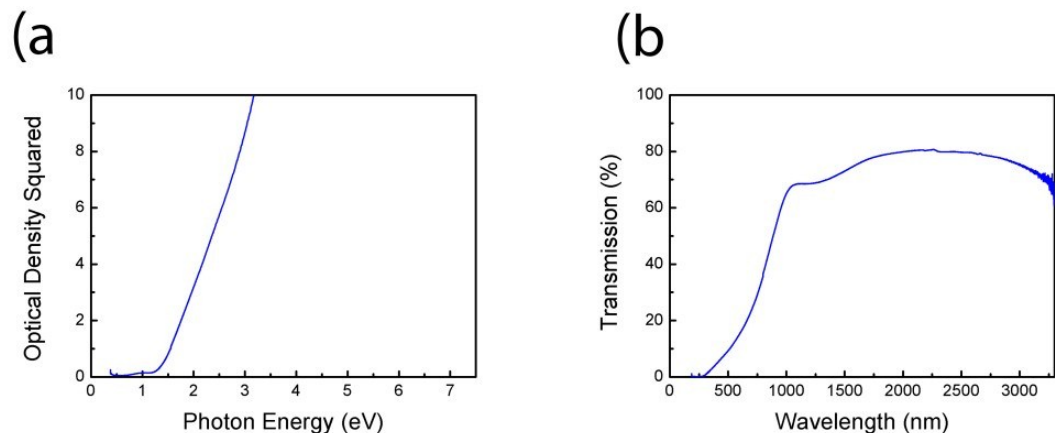


Figure 5.4 a) Optical absorption and b) Optical transmission spectra for InN/Ga<sub>2</sub>O<sub>3</sub>.

Figure 5.5 shows the absorption edge for the oxide substrate layer, which was estimated to be 5.59 eV. This value for  $\text{Ga}_2\text{O}_3$  is higher with respect to the reported value of 4.9 eV [104,105] for the crystalline form of  $\beta\text{-Ga}_2\text{O}_3$  which is the most chemically and thermally stable polytype, but it is comparable to values reported for smooth amorphous films grown by ALD [106]. The oxide showed a very high transparency optical transmission of approximately 95% at energies below the bandgap absorption edge.

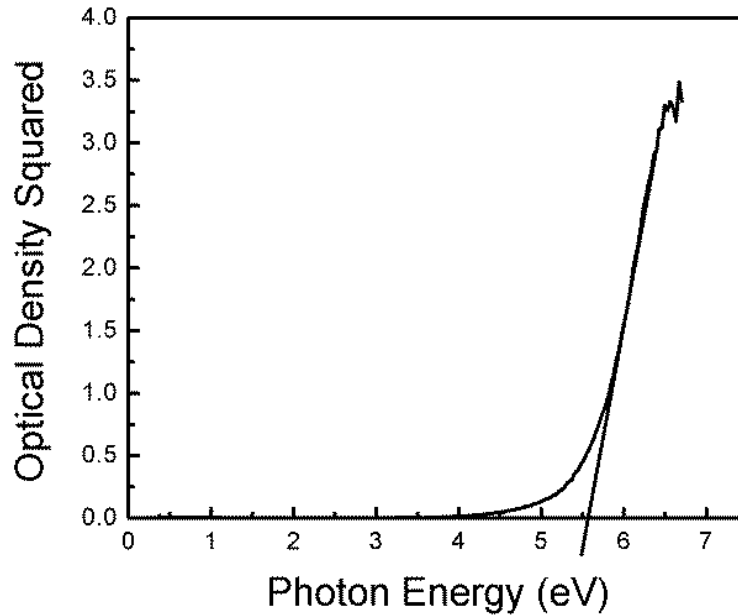


Figure 5.5 Optical absorption spectrum of the thin  $\text{Ga}_2\text{O}_3$  buffer layer showing a sharp absorption edge at 5.59 eV.

Other growths were attempted on rougher  $\text{Ga}_2\text{O}_3$  substrates, but these resulted in a poorer polycrystalline quality of the on top grown InN layers. SEM micrograph of such film is presented on Figure 5.6. It can be seen from the image that the crystalline quality of the on top grown InN layer was strongly dependent on the surface roughness of the underlying amorphous oxide. These initial results for high quality crystals achieved on

the thin amorphous oxide indicate some potential for the use of  $\text{Ga}_2\text{O}_3$  as buffer layers for InN growth. To date, the growth of InN has been focused mainly on growth on AlN and GaN buffers due to the need for lattice matched substrates. Smooth amorphous  $\text{Ga}_2\text{O}_3$  was demonstrated as an alternative buffer for reasonably good quality InN.

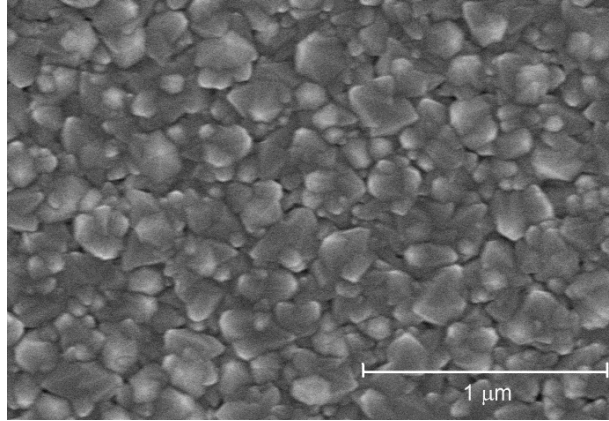


Figure 5.6 SEM surface image of InN grown on top of 20 nm rough  $\text{Ga}_2\text{O}_3$  thin layer.

### 5.2.3 InN grown on MOCVD GaN templates and sapphire substrates

Previous MEAgrow growths with non-optimized growth conditions were previously reported for InN grown on GaN and sharp heterostructures interfaces were produced at low temperatures [107] but these results were preliminary and the InN layers were largely polycrystalline. By optimizing the growth conditions in metal rich regime thin InN layers having excellent 2D morphology were produced on. The crystal quality for some of these layers was superior to the crystal quality achieved on the  $\text{Ga}_2\text{O}_3$  thin buffers as the MOCVD GaN templates were much thicker.

The surfaces of two sister samples grown on GaN and sapphire under the same growth conditions, are shown on the SEM micrographs in Figure 5.7. Figure 5.7a) shows the

surface of the sample grown on MOCVD GaN template and Figure 5.7b) shows the surface of the sample grown directly on nitrided sapphire substrate. It is evident that the InN film grown on GaN resulted in continuous epitaxial layer, whereas the InN grown on sapphire was polycrystalline. Both samples had substantially different visual appearance. The sample grown directly on sapphire had grey powdery look, indicating that indium metal had segregated during growth, while the sample grown on GaN was dark and uniform with no visible trace of segregated indium. Indium metal was confirmed by the x-ray diffraction spectra for the sapphire samples which are particularly sensitive to the tetragonal (101) In orientation, found at  $33.1^\circ$ . The XRD for the InN layers grown on GaN template and on sapphire is presented in Figure 5.8. There are no indium inclusions on the XRD spectrum for the film grown on the GaN template. The FWHM (266 arcsec) of the XRD peak for the sample grown on sapphire substrate is narrower than the FWHM of the peak for the sample grown on GaN buffer layer (338 arcsec). The narrower full width at half maximum for the peak of the polycrystalline InN grown on sapphire is due to the more relaxed small crystallites which leads to a reduced strain inhomogeneity, whereas the larger broadening of the peak for the sample grown on GaN could be attributed to inhomogeneous strain caused by misfit dislocations at the InN/GaN interfaces. The small peak at  $31.22^\circ$  is due to the K-beta line of the underlying GaN layer which is not completely removed by the nickel filter used in the XRD system.

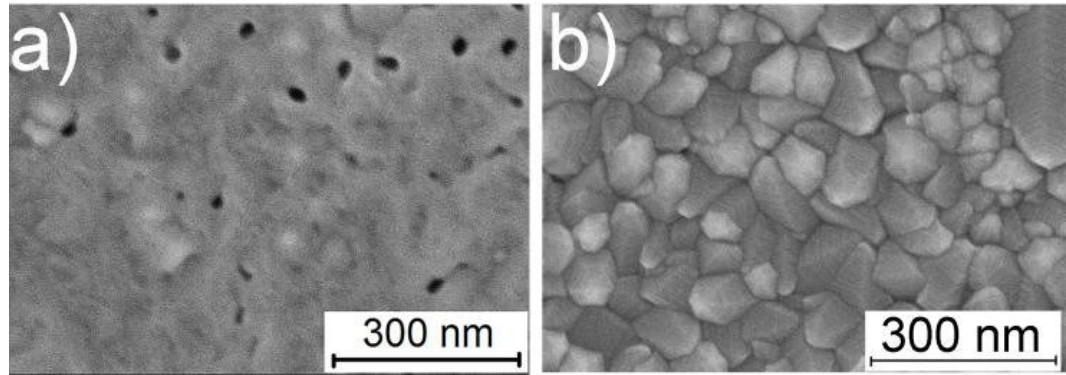


Figure 5.7 SEM micrographs of a) InN grown on a MOCVD GaN template, and b) the sister sample, grown directly on sapphire substrate.

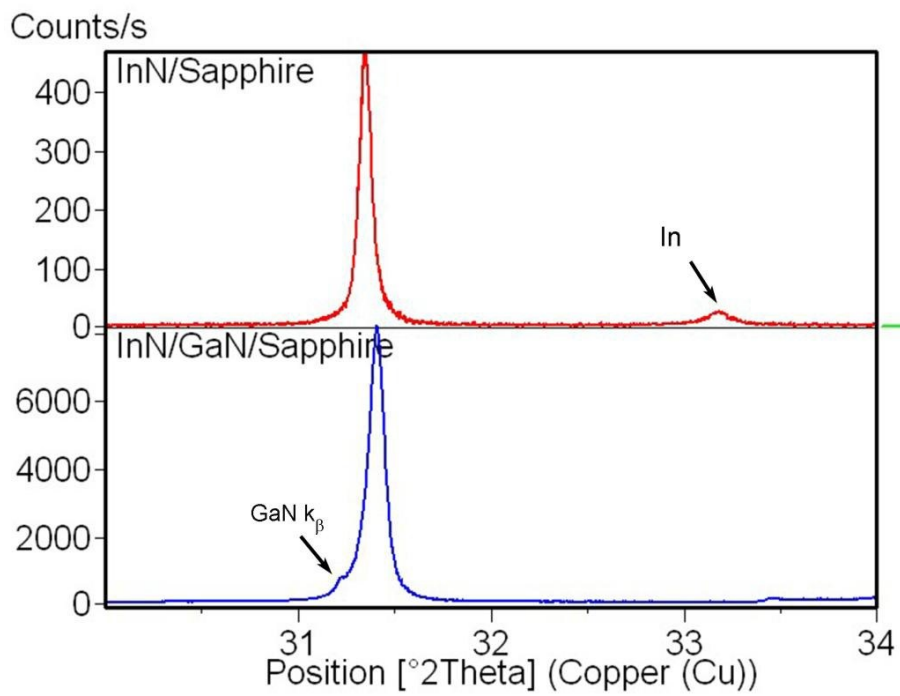


Figure 5.8 X-ray diffraction for the InN layer grown on GaN template and its sister sample grown on sapphire, corresponding to the samples presented on Figure 5.7.

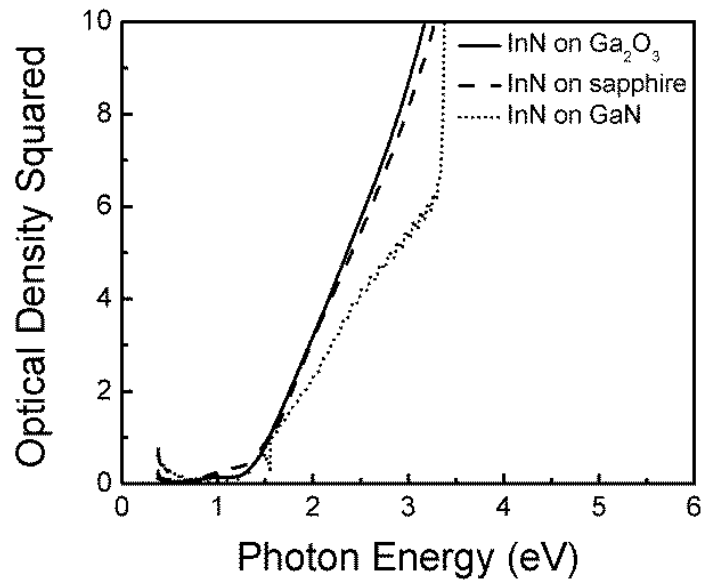


Figure 5.9 Optical absorption spectra for InN films produced by MEAgrow under similar growth conditions. A comparison is made among the layers grown on different substrates.

The optical absorption spectra of the InN layers grown under similar conditions on GaN, sapphire and  $\text{Ga}_2\text{O}_3$  are plotted for comparison in Figure 5.9. The three samples measured similar absorption edges close to 1.38 eV. The drop in the absorption spectrum for the sample grown on a commercial GaN at  $\sim 1.55$  eV is due to a common measurement artifact which is related to the change of the diffraction grating in the spectrophotometer. From Figure 5.9 is evident that if linearly extrapolated the absorption spectra with the x-axis, they will result in the same apparent energy bandgap which is independent of the films crystal quality as was previously studied by Chen et al. [101]. The comparison between the three absorption spectra appears to be reasonable because there was no evidence for free carrier absorption up to a wavelength of 3300 nm related to the presence of strong Moss-Burstein effect. The background electron concentration for the epitaxial layers grown on GaN templates could not be measured by Hall effect due to the

contribution from the background electron concentration from the underlying GaN layer. The carrier concentration for InN layers grown directly on sapphire was not measured as well due to the non-uniformity of the samples.

After further optimization of the growth conditions, 2D growth was achieved for the MEAgrow InN samples. SEM surface image of a layer grown at 512 °C in metal rich conditions by MME is presented in Figure 5.10. This image shows excellent quality fully coalesced material with large terraces. The height of the terrace steps was measured by AFM to be 2 nm and the RMS surface roughness was 4.2 nm over the measurement area. However, the RMS surface roughness over the terraces was less than 1 nm.

The *c* lattice constant was determined from the XRD spectrum to be 5.703 Å which agrees with the values reported for InN in the literature [20]. Large variations of the *c* lattice constant for InN are known to occur when there is defect incorporation, and this result indicates low level of defects present in the lattice.

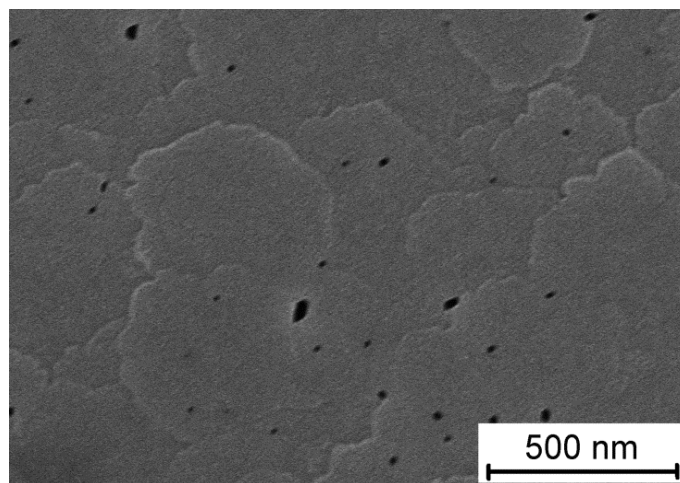


Figure 5.10 SEM surface image showing excellent 2D growth of an InN layer, produced by MEAgrow on commercial GaN template after optimized growth conditions.

### 5.3 Post-growth annealing studies on MEAGlow grown nitrogen rich InN

While previously in the chapter the growth of stoichiometric material was studied, this section describes the effect of annealing MEAGlow grown nitrogen rich InN thin films in air and in vacuum on their optical and electrical properties.

InN stoichiometry and defect structure is strongly dependent on the growth conditions [108]. Previous experimental work shows that InN films having large amount of excess nitrogen are typically grown at temperatures below 400 °C under non-equilibrium conditions [101]. For growth of nitrogen rich material, the use of plasma activated nitrogen as group V source is required in order to produce energetic species. The existence of nitrogen rich InN has been confirmed in the past decade. Such material was observed experimentally from at least 6 independent groups [109-115].

Considerable theoretical work for InN defect and electronic structures have been carried out for growth conditions comprising thermodynamic equilibrium [116-118]. In the thermodynamic equilibrium case it is well known that the growth of InN would result in nitrogen loss because of the high nitrogen overpressure required for InN and the low dissociation temperature of the material. Therefore, nitrogen vacancies ( $V_N$ ) have been considered for a long time as the main source for the high background electron concentration in InN films [119, 120]. When indium rich growth conditions are considered, Stampfl et al. calculated for zincblende InN, that the formation energy of  $V_N$  will be the lowest and nitrogen rich defects are impossible due to their very high formation energy ( $\sim 6$  eV) (See Figure 5.11) [117]. More recently, Duan and Stampfl

performed calculations for the wurtzite polytype of InN including nitrogen rich conditions as well, and they found surprisingly low formation energies for nitrogen rich defects [118]. The results are shown in Figure 5.12, and as can be seen, under these conditions the formation energies of nitrogen interstitials ( $N_i$ ) can be less than 1 eV. Under certain conditions these energies would allow the nitrogen interstitial to be the dominant defect in wurtzite InN [121]. In the work of Duan and Stampfl, the  $N_i$  defects are said to be triple donors, which can contribute to the high background electron concentration in the as grown InN, if the defects are in reasonable abundance. Butcher et al. have calculated from experimental results the activation energy for the nitrogen removal on the growth front for RPECVD grown samples as low as  $0.4 \text{ eV} \pm 0.1 \text{ eV}$ , which also suggests low formation energies for nitrogen interstitials since otherwise this defect could not exist in any significant concentration [121]. Similarly to the RPECVD process, MEAgrow growth process predominantly makes use of the lowest excited nitrogen molecular species  $N_2^*$ , having potential energy of 6.1 eV [121]. According to Butcher et al. for the formation of InN molecules an energy of 1.2 eV is needed, thus leaving 4.9 eV excess energy and an extra nitrogen atom. This energy exceeds the formation energies of some nitrogen rich native defects, shown on Figure 5.12, and will suffice for their formation [121].

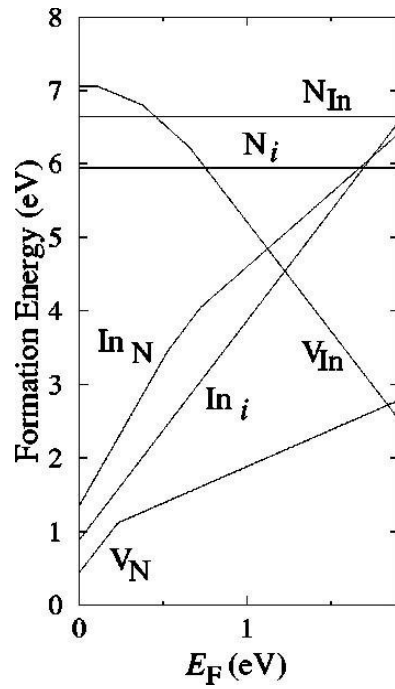


Figure 5.11 Activation energies calculated for indium rich growth conditions for zincblende polytype of InN. The picture is as shown in reference [117] from Stampfl et. al

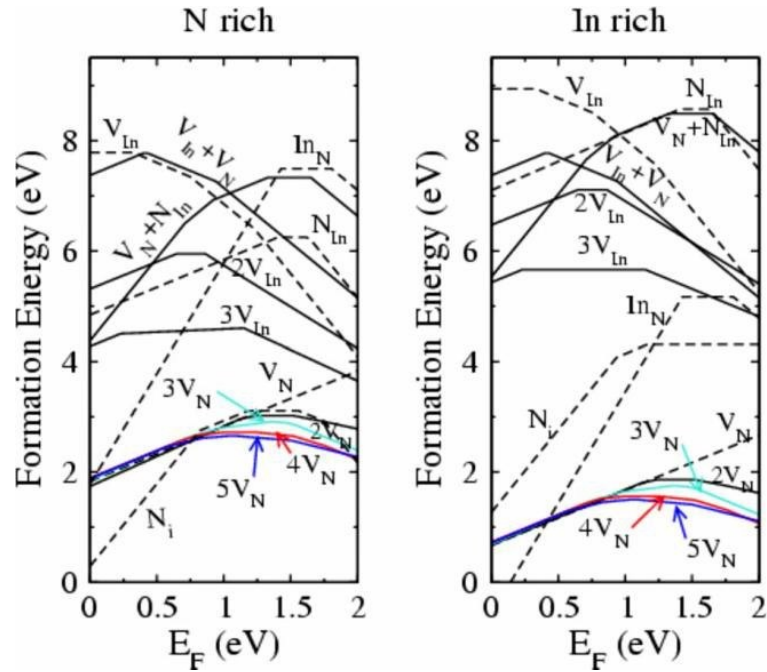


Figure 5.12 The formation energies for native defects for wurtzite polytype of InN under nitrogen rich and indium rich conditions, as presented in reference [118] from Duan and Stampfl.

In this work post-growth annealing was applied to some nitrogen rich samples in order to observe a potential nitrogen loss. Since the interstitial defects can act as donors in InN, annealing out the excess nitrogen should result in a change of the background electron concentration. If the carrier concentration is reduced due to a removal of the excess nitrogen present, it should also affect the apparent energy bandgap measured by optical absorption spectroscopy, as the extent of the Moss-Burstein effect would be smaller in this case. Hall effect and optical transmission spectroscopy were used to characterize the samples after each annealing procedure. X-ray diffraction measurements were performed after the film growth to check the crystallinity.

A series of four InN films were grown using the metal modulated epitaxy method under 2.2 torr chamber pressure on c-axis oriented sapphire substrates. The sapphire substrate

preparation procedure prior to growth was described in Section 5.2.1. The only variable parameter between the three samples was the growth temperature in order to vary the nitrogen to indium ratio in the films. The growth conditions for the MEAgrow samples are presented on Table 5.1.

Table 5.1 Growth conditions for Samples A, B, C, and D

Sample ID	Growth Temperature (°C)	Chamber Pressure (torr)	Nitrogen only Time (s)	TMI pulse Time (s)
Sample A	330	2.2	10 per cycle	20
Sample B	330	2.2	10 per cycle + 1800 at the end	20
Sample C	360	2.2	10 per cycle	20
Sample D	395	2.2	10 per cycle	20

In Figure 5.13 is presented the variation of nitrogen to indium ratio with the growth temperature for RPECVD grown samples in reference [121]. It can be seen that at 200 °C the amount of excess nitrogen measured in the films is extremely large reaching to N/In of about 1.7. Considering the relationship for the RPECVD samples, shown in Figure 5.13, it can be inferred that Samples A and B must have the largest abundance of nitrogen rich defects for this series, followed by Samples C and D, respectively. Samples A and B were grown under the same conditions and temperature (~330 °C). At this temperature the nitrogen to indium ratio should be about 1.2 according to Figure 5.13. XRD results, described below, confirm the extent of non-stoichiometry for these samples. For sample B, an additional 30 minutes long nitrogen plasma step was inserted at the end of the growth in order to flood the surface with nitrogen and create more excess nitrogen surface species. Nitrogen surface species attributed to nitrogen interstitial defects have been observed with XPS previously for RPECVD samples [90]. This interstitial nitrogen should

create more dangling bonds on the surface, thus contributing to and increasing the electron concentration in the surface accumulation layer of InN.

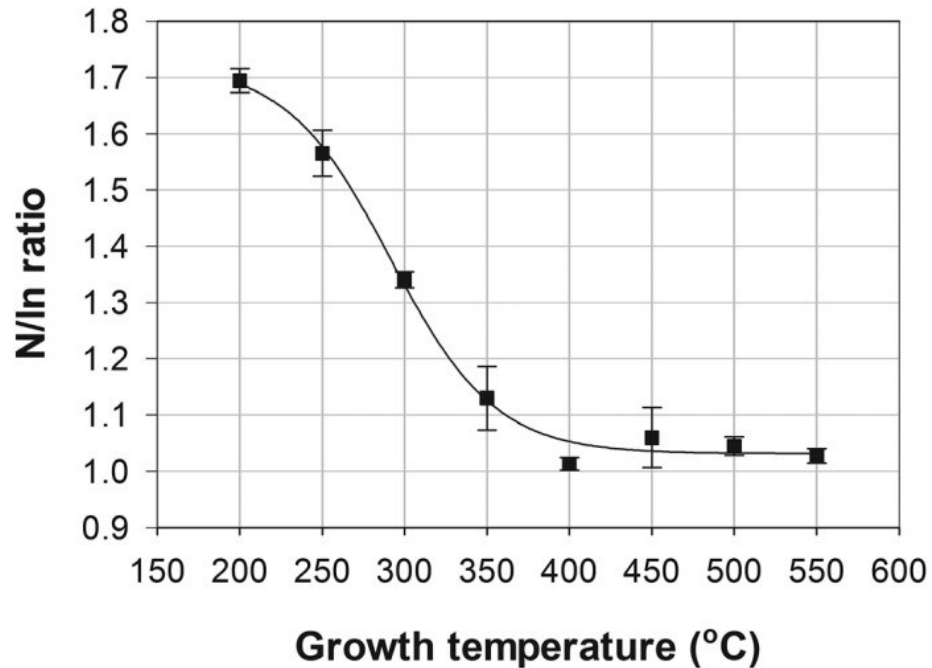


Figure 5.13 The growth temperature dependence on the nitrogen to indium ratio of RPECVD grown InN as it was presented in reference [121] by Butcher et al.

The films were approximately 500 nm thick. The sample thicknesses were measured from the interference fringes in the optical transmission spectra. This method sometimes can give a large error, which was found from previous observations, that can reach up to 50% compared to the more accurate values determined from the SEM cross-section images. Therefore, the values of the measured carrier concentration most probably deviate from the real values and the growth temperature dependence of the carrier concentration of the studied samples cannot be discussed here, but a great accuracy of these values is not necessary for the purpose of comparison between the different annealing experiments,

since the goal of the experiments was to observe a change in carrier concentration potentially caused by the annealing out of the excess nitrogen species present in the films.

Samples A and B measured different thicknesses most probably because some etching has resulted from the 30 minutes long plasma step at the end of the growth of sample B. The carrier concentration for sample B is a little bit higher than the carrier concentration of sample A, but it may just be because the sample is thinner, or it can also be as a result of the more nitrogen rich surface. That sample B is thinner than sample A is also evident from the lower slope of the linear part of the absorption squared in the optical absorption spectrum shown on Figure 5.15. The mobility of sample B is a little bit lower than the mobility of sample A probably because of the higher electron concentration but is of the same order suggesting similar crystalline quality. Both samples had the same absorption edge at  $1.58 \text{ eV} \pm 0.02 \text{ eV}$ . The InN film grown at  $360 \text{ }^\circ\text{C}$  measures the largest thickness by optical transmission spectroscopy, indicating a faster growth rate resulting from the more efficient decomposition of TMI, while the sample grown at  $395 \text{ }^\circ\text{C}$  was thinner and had more metallic look indicating that the growth rate was limited by the presence of too much excess metal on the growth surface. Samples C and D were grown at elevated temperatures and they had a more metallic appearance, while samples A and B resulted in very dark (a little darker than expected) uniform films, as has been previously observed for nitrogen rich material grown at  $300 \text{ }^\circ\text{C}$  [122]. A little cloudiness is present on the surface of sample C. Photos of the samples were not taken because they were lost in the vacuum chamber while unloading after the last annealing experiment in vacuum but all the films followed the trend in reference [30] for the variation of the colouration of RPECVD InN samples grown under similar temperatures.

The presence of tetragonal In (101) for samples C and D was confirmed by the x-ray diffraction  $\omega$ - $2\theta$  scan. The spectra are presented on Figure 5.14 . All the samples showed a highly c-axis oriented crystalline structure. The c lattice constants for samples A and C (5.722 Å) are greater than the lattice constant of sample D (5.706 Å), which was produced at higher temperature and is supposed to be more stoichiometric. The value for the c lattice constant of Sample D is closer to the value, reported for stoichiometric InN (5.703 Å). The large c lattice constants for the samples grown below 400 °C are commensurate with the lattice constants obtained for nitrogen rich samples studied previously for RPECVD (see Figure 4 in ref. [123]), although the values are lower than the values for samples grown by reactive evaporation [112]. The presence of interstitial nitrogen defects was suggested to relate to strong hydrostatic strain arising from the introduction of this defect into the InN lattice. The presence of segregated indium metal in nitrogen rich material is not uncommon. Indium metal has been observed previously on the XRD spectra of samples that measured ratio of N/In > 1 [124].

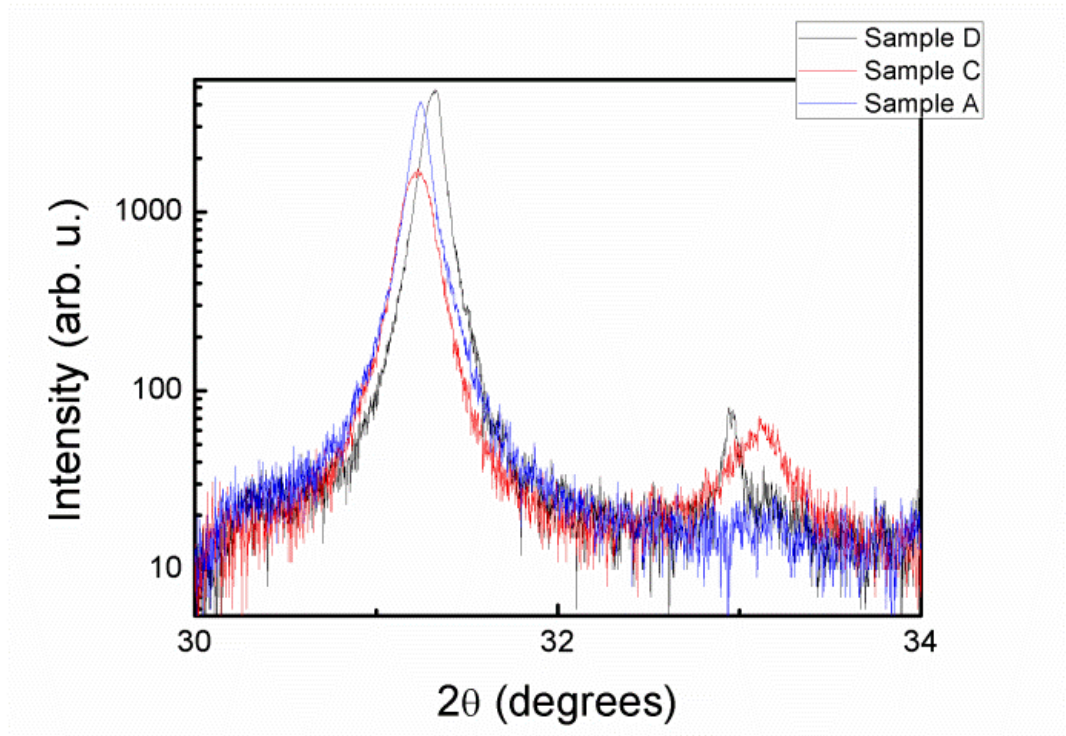


Figure 5.14 XRD spectra for the 4 annealed samples grown at temperatures between 300 °C and 400 °C.

The optical absorption spectra of the four samples are presented on Figure 5.15. Sample C and D showed apparent energy bandgap of 1.32 eV and 1.18 eV. These results agree well with previous studies for the growth temperature dependence of the apparent energy bandgap of InN grown on sapphire substrates [101].

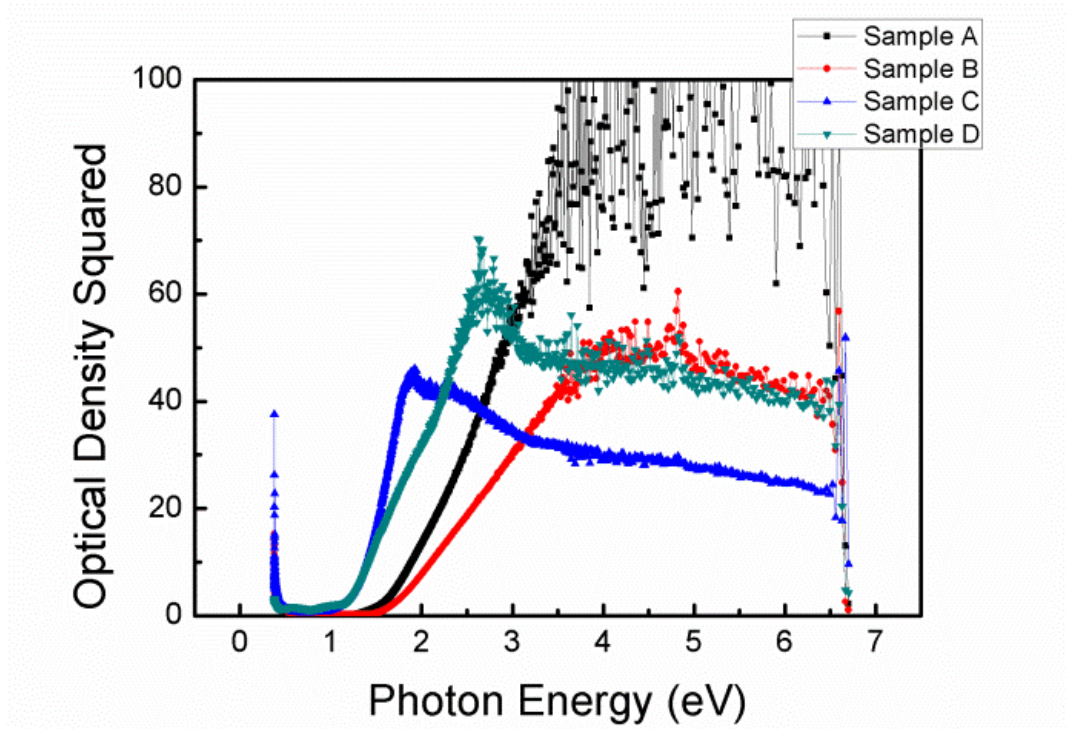


Figure 5.15 Optical absorption spectra for the four annealed samples grown between 300 °C and 400 °C.

The four samples of this series were annealed together under moderate vacuum conditions of  $10^{-6}$  torr. Table 5.2 summarizes the annealing conditions and the results before and after each procedure. The samples were first annealed for 1 hour at 390 °C and no change was observed in either the carrier concentration or the apparent energy bandgap of the InN layers. The temperature was further increased to 460 °C and again no major changes were found for annealing time of 1 + 12 hr. These results indicate that the excess nitrogen defects present in the bulk are too resilient to anneal out at comparable temperatures with those reported for removal of the defect from the growth surface. This means that significantly larger energies are required for the defects once incorporated in the bulk crystal to diffuse and form nitrogen molecules and eventually escape from the

crystal. It was noted by Butcher et al. [121] that defect removal during growth was a two step process, diffusion of the defect species to the surface, and their subsequent desorption. Obviously during growth the diffusion step is less important since the defect species are closer to the sample surface, whereas diffusion becomes the limiting process for annealing an already grown sample.

Table 5.2 Results from InN post-growth annealing.

Sample ID	Anneal Temperature (°C)	Time duration (hour)	Carrier Concentration	Mobility	Apparent Energy Bandgap (eV)
Sample A	Before anneal	N/A	1.30E+20	27.1	1.57
	387	1	1.31E+20	26.9	1.57
	460	1	1.32E+20	26.7	1.57
	460	12	1.30E+20	26.6	1.57
Sample B	Before anneal	N/A	1.83E+20	24.2	1.58
	387	1	1.84E+20	23.9	1.58
	460	1	1.86E+20	23.2	1.58
	460	12	1.94E+20	21.9	1.58
Sample C	Before anneal	N/A	1.15E+20	42.8	1.31
	387	1	1.17E+20	41.8	1.31
	460	1	1.18E+20	41.6	1.31
	460	12	1.18E+20	41.4	1.31
Sample D	Before anneal	N/A	2.16E+20	51.5	1.18
	387	1	2.14E+20	51.6	1.18
	460	1	2.13E+20	51.5	1.18
	460	12	2.16E+20	50.6	1.18

Another annealing experiment was performed for a 170 nm thin sample grown at 290 °C. The thickness was determined from the SEM cross-section, presented in Figure 5.16. The polycrystalline columnar structure of the sample is evident from the micrograph with crystallite size less than 200 nm along the a-lattice constant. The carrier concentration of the sample was measured by Hall effect to be  $2.75 \times 10^{20} / \text{cm}^3$  before the annealing in

vacuum. This value is comparable with polycrystalline nitrogen rich RPECVD films grown at the same temperature [108]. The results from the annealing experiment are presented in Table 5.3. For this sample no change was observed as well even when the temperature was raised to 515 °C, confirming the results from the first series of examined samples with nitrogen to indium ratio greater than unity. Since the carrier concentration remained the same for 13 hours anneal at 515 °C, it follows that no decomposition occurred for the InN nitrogen rich film at this temperature.

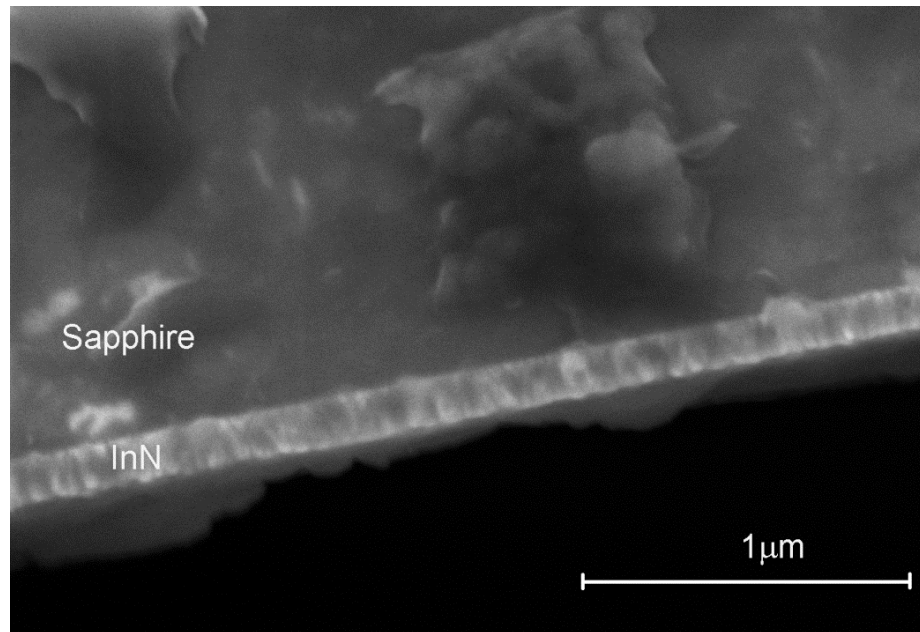


Figure 5.16 SEM cross-sectional image of the sample grown at 290 °C. The columnar structure is evident from the micrograph, showing small grain size less than 200 nm.

Table 5.3 Properties of the annealed samples.

Sample ID	Anneal Temperature	Time Duration (hr)	Carrier Concentration	Mobility	Apparent Energy Bandgap
2012-01-04-2-InN Same section	Before anneal	N/A	2.75E+20	9.73	1.81
	387 vacuum	1 hour	2.76E+20	9.7	1.81
	387 vacuum	1+12 hours	2.82E+20	9.29	1.81
	432 vacuum	1 hour	2.81E+20	9.3	1.81
	432 vacuum	1+12 hours	2.82E+20	8.74	1.82
	480 vacuum	1 hour	2.84E+20	8.64	1.83
	480 vacuum	1+12 hours	2.77E+20	8.61	1.83
	515 vacuum	1 hour	2.73E+20	8.04	1.82
	515 vacuum	1+12 hours	2.80E+20	7.9	1.82
	400 air	10 min	2.60E+20	5.77	
	400 air	30 min	2.02E+20	4.68	
	400 air	1 hr	2.30E+00	3.24	

There are many existing reports for various decomposition temperatures of InN [125-128] and a considerable discrepancy among the various data. Thermal annealing studies have also been performed on nitrogen rich samples grown by modified activated reactive evaporation (MARE) [112]. In this article the authors report that their nitrogen rich samples start decomposing at 500 °C. Their samples experienced major changes of their electrical and optical properties for both and vacuum annealing at 400 °C. The MARE samples were grown at significantly lower temperatures than the MEAglow samples (about 170 °C to room temperature), and they also observed oxygen incorporation under vacuum anneal. At such low growth temperatures, the nitrogen defect density should be very high, which would make the films less stable.

This and another sample, grown at the same temperature but 460 nm thick, were annealed in air at 400 °C for 10 minutes, followed by another annealing for 30 minutes and 1 hour. The results for both samples showed the same trend. The carrier concentration didn't change and there was a slight decrease in the mobility possibly indicating oxygen incorporation at the grain boundaries. It was previously reported that oxygen tends to segregate as an amorphous oxynitride at the grain boundaries of InN thin films [129]. These studies suggest that nitrogen rich MEAgrow samples are stable up to near the decomposition temperature for InN.

Two pieces from a nitrogen rich sample grown at 360 °C were first annealed in air. One piece 1a, was annealed for 10 minutes and the other 1b, for 1 hour at 400 °C. The mobility of the sample annealed for 1 hour dropped more than the piece annealed for 10 minutes possibly indicating that more oxygen had incorporated at the grain boundaries of the crystallites and impeded the conduction path of the carriers. Both pieces were afterwards annealed in vacuum at 430 °C for different time durations. Hall effect was performed after each period. The results are presented in Table 5.3. The two pieces showed improvement by a slight increase of their mobility, perhaps indicating some desorption of incorporated oxygen. Interestingly, the piece annealed for a longer time in air decomposed after exposure to 430 °C for 37 hours under vacuum, which was indicated by an increase of the carrier concentration, while piece 1a improved further. The reason for the faster decomposition of the piece annealed for longer time in air could possibly be attributed to the formation of more amorphous oxynitride between the grains and when this larger amount was annealed out, the film became less stable. In order to test the thermal stability of piece 1a, it was heated in vacuum for an additional 40 hours but no

further improvement or decomposition were observed. Since none of the rest nitrogen rich samples showed any change in their electrical properties up to temperatures of 515 °C, it can be inferred that the improvement of the two pieces can be attributed to the desorption of the incorporated oxygen during the air heating.

## Chapter 6. Growth of InGaN by MEAgrow

InGaN has been widely studied for its application in light-emitting diodes [130,131], and potentially in solar cells [4,6,132,133] because its direct bandgap can be tuned over the entire visible range. The alloy has already found application in violet, blue, and green LEDs and the growth of films having low indium mole fraction is well established using commercially available techniques such as MOCVD, while the performance of yellow and red LEDs is poor, probably because of poor material quality. The first commercially available bright blue LEDs from InGaN/GaN double heterostructures were demonstrated by S. Nakamura in 1993 [134]. These LEDs had a broad spectrum which was attributed to the introduction of Zn in the active InGaN layer. This was followed by the production of blue/green single quantum well LED structures [33,135]. The indium content for these structures was varied from 20 to 70 % in order to change the InGaN peak wavelength from blue to yellow but the emission spectra for green and yellow were broad and the structures had low power output, which was attributed to the strain between the InGaN well and the barrier layer [135].

The growth of InGaN over the entire alloy composition is plagued by inherent material properties so that high quality epitaxial crystals are hard to produce. Large lattice mismatch and the different thermal stability between GaN and InN are some of the

reasons for the challenging epitaxial growth. High quality crystals having high indium content are especially hard to achieve in comparison to gallium-rich ones because of the lower decomposition temperature of InN. Phase segregation in the alloy is another factor inhibiting the production of good quality InGaN films. The possible causes for phase separation have been described in ref. [138,38]. The occurrence of phase separation, the alloy composition, and the dissociation of InN can be strongly affected by the growth temperatures which have to be selected very carefully, as well as other growth parameters. In this thesis the growth of InGaN layers was attempted at temperatures in the range of 400 – 540 °C by MEAgrow MME. The upper temperature limit was determined by the re-evaporation of indium which occurs above 540 °C.

The following study aimed to find optimal growth conditions for improvement of the crystal quality and increasing the indium content in MEAgrow InGaN 100 – 300 nm thick layers. The first section in this chapter is a summary of the effect of metal rich growth conditions applied for InGaN layers grown directly on sapphire substrates and the phase segregation caused by clustering of indium on the growth surface. Section 1.2 is about the effect of metal pulse length on the indium incorporation at elevated temperatures. In Section 1.3 the composition-dependent structural, electrical and optical properties of the MEAgrow InGaN samples with respect to growth temperature are presented. Section 1.4 discusses briefly the InGaN grown on GaN buffer layers which are compared to MEAgrow InN grown using similar conditions on the same buffers in order to assess the effect of the lattice mismatch between the three compounds.

## 6.1 Growth in metal rich regime

Indium segregation is a common problem in InGaN growth at low temperatures which originates from the differences in the formation enthalpies of InN and GaN. Indium segregation at the growth front is known to have a detrimental effect on the optical properties of the material [137,138] and different strategies are applied in the various growth techniques to prevent it. For instance, in MOCVD reactors this issue is being solved by growth at higher temperatures ( $\sim 800$  °C) and high III/V ratios in order to maintain reasonable indium incorporation [137]. Surface segregation has been widely observed in MBE systems as well [138-142]. In non-modulated MBE growth, the indium segregation is typically related to the III/V ratio and is prevented by growth in the nitrogen rich regime [138,141]. GaN is normally grown under a slightly metal rich regime in MBE in order to maintain smooth surfaces, but growth of InGaN requires lowering of the Ga flux typically used for the metal rich regime. At high enough growth temperatures, the indium metal can act as a surfactant under metal rich conditions aiding in the growth of GaN with only small amounts being incorporated [140].

The following experiments were performed to eliminate the indium surface segregation present in the initial MEAgrow InGaN growths, while maintaining metal rich growth conditions. MBE growth using the MME method has been used for InGaN in the metal rich regime throughout the full indium compositional range [142]. In their work Moseley et al. report that the phase separation resulting from indium surface segregation was prevented by an increased frequency modulation of the metal shutters and by decreasing the time for the metal pulse. The results in ref. [142] demonstrate that indium segregation at the growth front does not depend on the growth regime but that it is more dependent on the quantity of the adsorbed metal layer. MEAgrow growth in the metal rich regime also resulted in indium surface segregation but a different strategy was used for preventing it,

since decreasing the metal pulse length can lead to a change in the alloy composition for this technique (see Section 6.2). In the MEAgrow growth regime we observed that low temperature growth of InGa<sub>N</sub> can be achieved without indium surface segregation regardless of the presence of a high metal dose and long pulse duration.

The InGa<sub>N</sub> samples for the study in this section were grown at approximately 420 °C on ¼ sections of 2'' sapphire wafers that were annealed at 1050 °C for 1 hour in air prior to growth. High metalorganic flow rates were used to deposit enough metal to enhance the adatom surface mobility. Equal flows of 1 sccm for both TMI and TMG were pulsed at a chamber pressure of 2.2 torr. The plasma source was operated at its maximum power (600W) and the nitrogen flow rate was set to 1400 sccm. The growth occurred for 600 cycles with a total time per cycle of 55 s, and time for metalorganic flow of 30 s. For these experiments occasional flushing of the chamber with nitrogen gas was introduced in order to remove the metalorganic and prevent indium droplet formation from TMI buildup in the chamber. Results for the three samples are presented. Two of the samples, Sample 2 and Sample 1 were grown under different growth conditions with and without a metalorganic (MO) flushing step, respectively. Sample 1 resulted in InGa<sub>N</sub> of indium composition in the alloy of 34 %, and the other two samples had indium concentration of 40 %. The indium mole fraction was calculated from the XRD peak position using Vegard's law assuming linear dependence between the bandgap of GaN at 3.4 eV and the bandgap of InN, believed to be 0.7 eV, though considerable controversy still exists in regards this latter value [143,144]. The 0.7 eV value was selected for this calculation in order the following results the obtained bowing parameters to be comparable with other values reported in the literature. According to the theoretical report presented in [144] a significant impact of an electron localization present in disordered solid crystals has to be

considered for the determination of the crystal properties. The author of [144] studied the impact of these electron localizations which can possibly account for the higher energy bandgap of InN, reported in the literature [119]. Alexandrov suggests a value for the energy bandgap of InN of about 1.9-2 eV when the electron localizations are taken into account [145].

Figure 6.1 shows the x-ray diffraction spectra of the three studied samples. The main InGaN peak is present at  $33.44^\circ$ . A second peak due to another phase of material is present on the XRD spectra at  $31.35^\circ$  and is due to InN. The InGaN peak of Sample A is shifted to higher angle with respect to the rest of the samples. Similar shift of the XRD peak is observed in ref. [142] and is suggested to be related to indium segregation at the growth front that would shift the InGaN peak towards GaN and leave indium droplets. The small XRD peak at  $35.3^\circ$  was observed only in some of the samples with various degree of powder on the surface and its origin is unknown, although it could be a second reflection from InGaN powder on the sample surface.

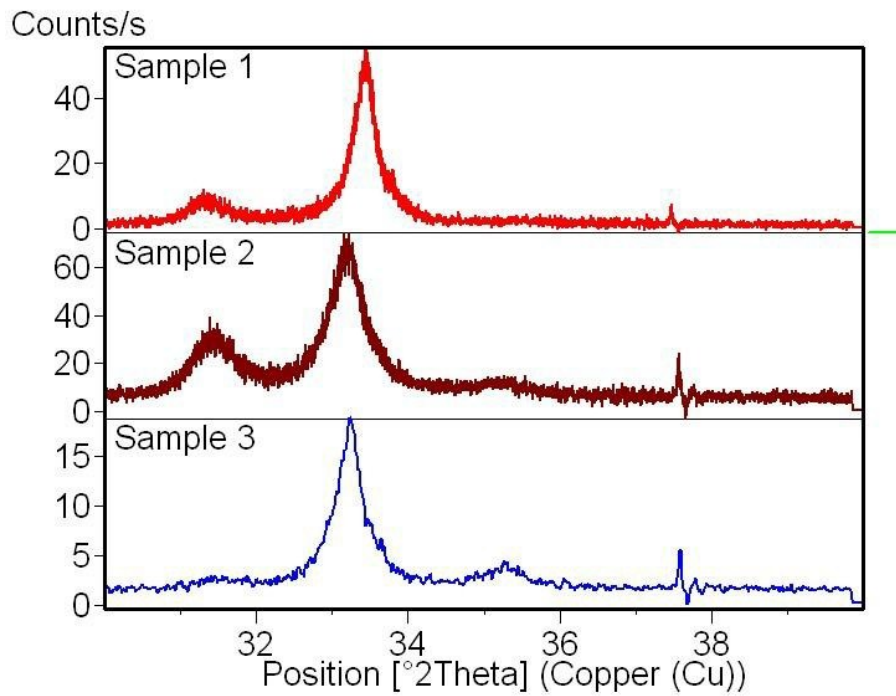


Figure 6.1 XRD of samples grown with (samples 2 and 3) and without (Sample 1) metalorganic flushing step.

The optical absorption data for Sample 1 is presented on Figure 6.2. From the data is evident that there can be extrapolated two distinct linear regions of the optical density squared with the x-axis. The first region appears at 0.6 eV, and the second region is at 1.9 eV. These two absorption edges in combination with the XRD results indicate that phase segregation resulting from indium surface segregation at the growth front is present in the alloy. The indium is converted to a nitride at the surface during the final stages of the growth.

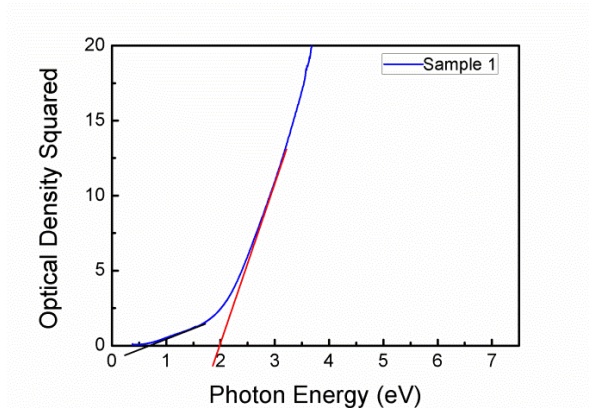


Figure 6.2 Optical absorption of Sample 1 showing two linear regions of the optical density squared.

For Sample 2, after introducing an MO flushing step in every 26<sup>th</sup> cycle and 2 hours cooling in the growth chamber. The optical absorption spectrum resulted in a single absorption edge of 2 eV (Figure 6.3), though some tailing is still evident from the absorption below this band edge. However, the XRD spectrum again indicated the presence of an InN phase. This InN phase could be the result of a surface contribution of a nitrated indium that deposited from the chamber at the end of the InGa<sub>N</sub> growth, perhaps during cooling, as the growth was terminated by nitridation at the beginning of the cooling step, though a good part of the indium that would have segregated during growth was eliminated by the flushing of the metalorganics in the reactor during growth. The results for Sample 3, discussed below would seem to confirm this hypothesis. Sample 3 was grown under the same conditions as Sample 2 but was taken out of the growth chamber very quickly during the MO flush step before the end of the program, so that no after-deposit could form during the cooling step. Instead of cooling in the growth chamber, where there still might be some residual TMI or indium, the sample was cooled in the load lock.

The XRD spectrum of sample 3, in Figure 6.1, shows only a very small InN peak. This InN was found to be present in a very small amount only on the surface. This is evident from a grazing incidence x-ray diffraction scan carried out at  $10^\circ$  grazing incidence angle (Figure 6.4). Figure 6.4 shows that the intensity of the InN peak increases with decreasing incident angle and the intensity of the InGaN peak decreases. This result indicates that the InN is a surface contribution since at grazing incidence the X-ray beam doesn't penetrate very deeply into the sample. The small XRD peak at  $35.3^\circ$  was also found to increase in the grazing incidence spectrum, again indicating that it is probably related to the surface and not the bulk of the layer. Similarly to Sample 2, Sample 3 also showed an absorption edge at 2.02 eV (Figure 6.5) though with significantly less tailing apparent than for Sample 2.

In ref. [142] very small amounts of indium nitride also remained on the surface as a result of the thermal decomposition during the cooling process after growth for samples grown by the Georgia Institute of Technology. They resolved this issue by capping the InGaN surface with 10 nm thick GaN layer, though this would be a non-optimal solution for many device structures.

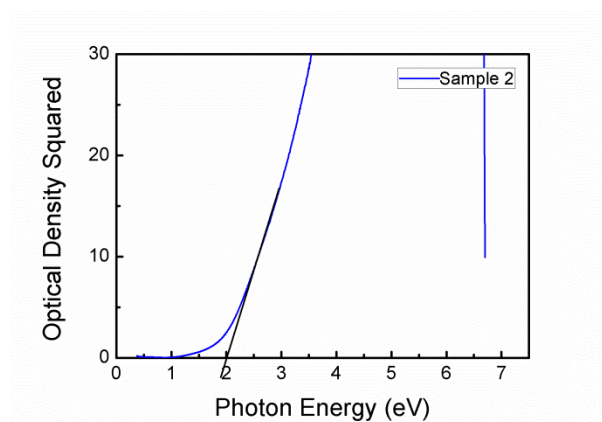


Figure 6.3 Optical absorption spectrum of Sample 2.

These results demonstrate a significant improvement of the MEAgrow grown InGaN and it is also an indicator that metal rich growth conditions can be applied successfully for compositions of up to 40 % indium without phase separation resulting from indium condensation on the growth surface.

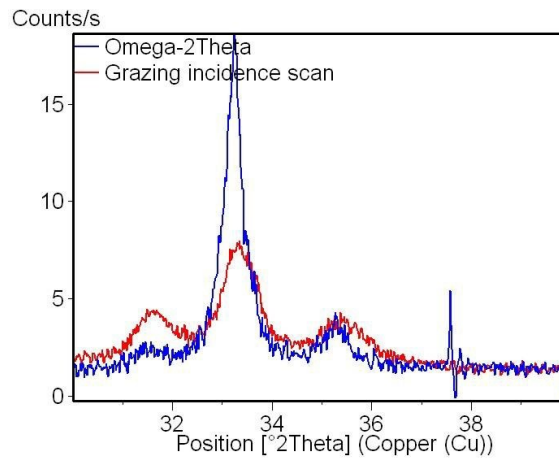


Figure 6.4 Comparison between  $\omega$ -2 $\theta$  and grazing incidence scan of Sample 3.

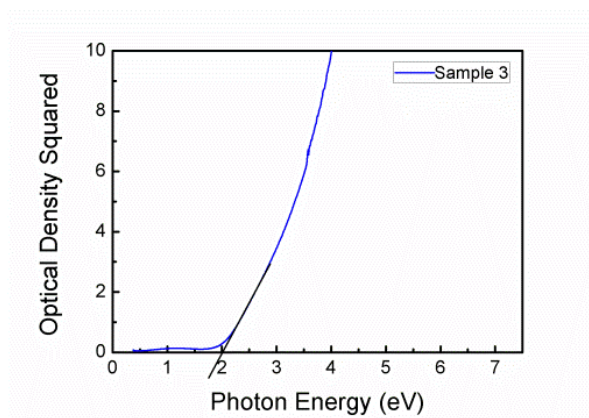


Figure 6.5 Optical absorption edge of Sample 3.

## 6.2 The effect of metal pulse length

One of the objectives of this study was to try and increase the indium incorporation in the InGaN films, which for MOCVD has proven to be problematic. In an MOCVD

environment the use of metalorganic precursors and ammonia are limiting factors which require a lot higher growth temperatures than the dissociation temperature of InN and this represents an obstacle for the growth of high indium content layers. In MEAgrow, ammonia is not being used as a nitrogen precursor but trimethylgallium needs a high enough temperature to undergo pyrolysis and release the three methyl groups. A series of InGaN films were grown at 540 °C while varying the time for the metalorganics pulse. This was done in order to decrease the amount of metal used and observe changes in the quality of the material grown. The rest of the growth parameters were kept constant. Four samples were selected to represent the trend from the variation of the metal pulse length. Figure 6.6 shows the XRD spectra of the samples studied from this series. Samples A, B, C, and D were grown with metalorganic flowing for 10, 7, 5, and 3.5 seconds, respectively. The number of cycles was increased with each growth in order to maintain approximately the same overall growth time.

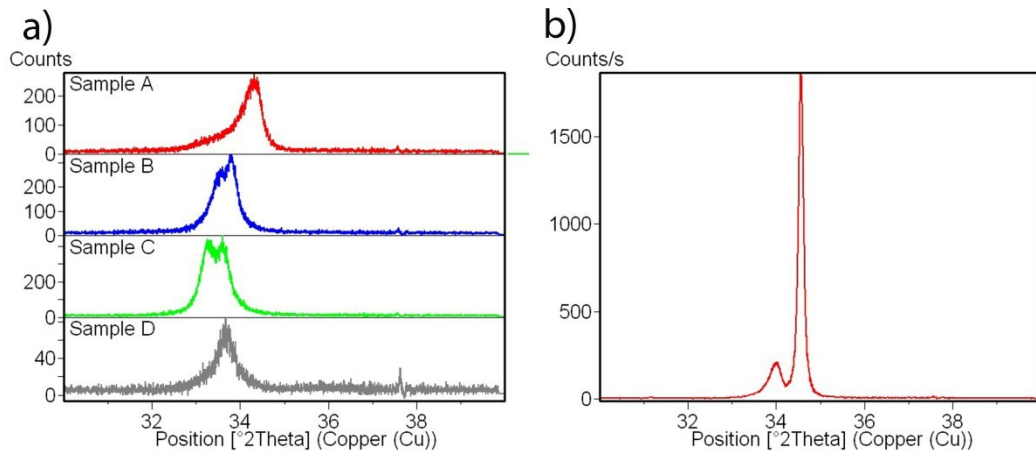


Figure 6.6 a) XRD spectra showing the variable composition with varying the time for the metalorganic pulse, and b) XRD of the sister sample of Sample C grown on GaN, showing a single InGaN peak at 34 ° and a GaN substrate peak at 34.6 °.

From Figure 6.6a) can be seen that the indium mole fraction in the samples increases to sample C when decreasing the time for the metalorganic pulse. This same situation is not

observed in MBE [142], where the decrease of the metal pulse didn't affect the alloy composition. The pulse times in ref. [142] were decreased from 10 s to 4 s and this didn't change substantially the alloy composition. However, CVD metalorganic delivery is much more complex than the direct flux delivery of an MBE system. Optimally we would hope that the indium to gallium ratio would remain much the same with a change of the metalorganic pulse time, but the decomposition rates of the metalorganics may be different, also delivery of molecules to the sample surface may change with time due to the weight of molecules in what is otherwise a nitrogen flow. There may also be some loss of the indium from the sample surface due to desorption, as the indium can desorb at a lower temperature compared to gallium. This might be explained by some loss resulting from an increased residence time for the indium atoms on the growth surface, since fewer of them will desorb at 540 °C if the pulse time is shorter. The indium composition was found to be 9 % for Sample A and was determined from the contribution of the main XRD peak where a large tail is observed in the base, perhaps indicating composition fluctuations mainly due to the low solubility of InN in GaN. For Sample B two peaks were present with one phase having 23 % indium and the second with 29 %. Further increases in the amount of indium was found for sample C, again with two phases present on the XRD spectrum – one at 28 % and the other at 38 %. A single peak of InGaN with slightly decreased indium concentration (27 %) was observed for the InGaN grown with 3.5 seconds MO flow (D), showing a more homogeneous compositional distribution. The two distinct separate phases observed in B and C can be attributed to strain effects between the InGaN and the sapphire substrate. This can also be inferred from the XRD spectrum of the sister sample of Sample C grown on GaN buffer layer, where a single InGaN phase with 17% indium content was present (Figure 6.6b)). The indium

composition for the sample grown on sapphire is increased by strain relaxation, which can be related to the compositional pulling effect observed in other reports [146]. The epitaxial growth of InGaN on sapphire leads to strain in the InGaN layer due to the large lattice mismatch with the sapphire. If the layer thickness is less than a certain critical layer thickness, the film is pseudomorphically strained. After exceeding the critical layer thickness, the strain is relaxed through the introduction of extended defects and the magnitude of strain decreases. A TEM image is presented in Figure 6.7 for InGaN grown directly on sapphire showing the presence of threading dislocations and stacking faults, among other defects, related to the lattice mismatch between the sapphire and the InGaN.

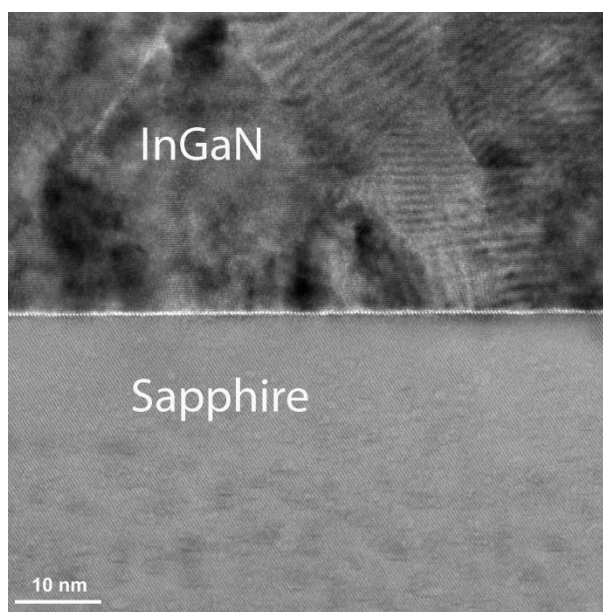


Figure 6.7 TEM cross-sectional image of a 100 nm thick InGaN grown on sapphire

The increase of indium amount was further confirmed by the optical absorption spectra which showed a decreasing energy bandgap. The bandgap determined from the optical absorption spectra is plotted against the metalorganic pulse length in Figure 6.8a). The measured bandgaps for A, B, and C are very low for the corresponding indium mole fraction, determined from the XRD parameters measured for the main peak, which could

be attributed to the presence of a second In-rich phase of the InGaN. The point for Sample D shows an increased energy bandgap in comparison with the other three samples, and a part of this increase may be due to the presence of slight free carrier absorption observed at wavelengths above 2500 nm from the optical transmission spectrum (Figure 6.8b), which may indicate the presence of a Moss-Burstein effect. Sample D showed the highest carrier concentration among the rest of the samples in the growth series which was in the order of  $10^{20}/\text{cm}^3$ . A part of the high carrier concentration may be due interface effects, as the layer was only 70 nm thick, but the absorption at high wavelengths clearly indicates also relatively high electron concentration in the bulk. Moss-Burstein effect has been observed for degenerate InN films [119], as well as in GaN [147] and for indium rich InGaN layers grown by MARE [148,149]. However the presence of Moss-Burstein effect is only an assumption in this work because no additional theoretical study was done. This theoretical study includes determination of parameters connected with the energy band gap of InGaN and due to this reason the study goes beyond the scope of this dissertation. The carrier concentrations and mobilities for the studied samples are presented in Table 6.1. Hall effect measurements for sample A couldn't be performed because of the powder formation on the surface and its non-homogeneity but it showed some conductivity at room temperature.

Table 6.1 Hall Effect data for Samples A, B, C, and D.

Sample ID	Carrier Concentration	Mobility
A	N/A	N/A
B	-1.57E+19	2.18
C	-2.36E+19	4.94
D	-1.63E+20	1.29

As a result of the decreased pulse length the indium incorporation increased by decreasing the residence time of the indium atoms on the surface to an optimum value around 5 seconds and then began to decrease again. Incorporation of more indium led to improved quality of the layers grown on sapphire and to reduced phase segregation.

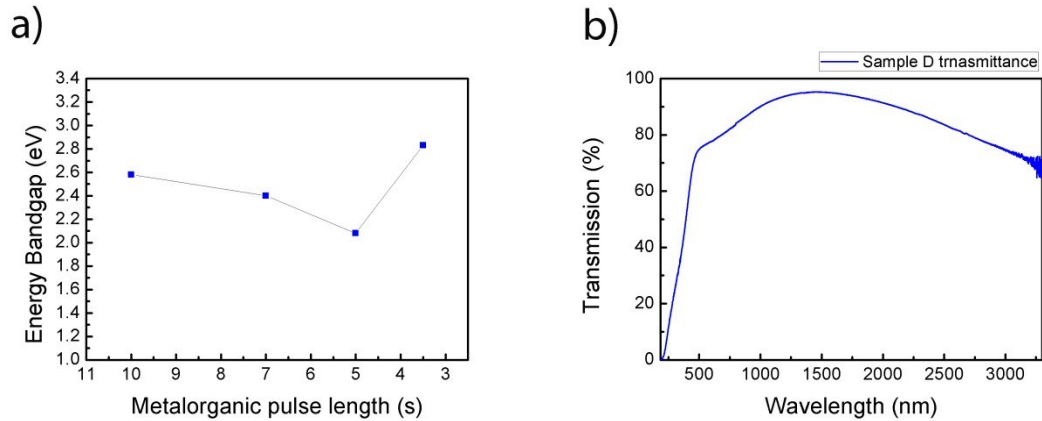


Figure 6.8 a) The variation of the optical bandgap with the MO pulse length, and b) optical transmission for Sample D.

### 6.3 The effect of growth temperature

Many observations have shown that the indium composition in InGaN is very sensitive to the growth temperature [137,150,151]. The typical growth temperature range for the binary compounds in the MEAgrow reactor can start from temperatures as low as 290 °C at which temperature nitrogen rich InN is grown and reach up to 520 °C for metal rich InN films, while GaN is grown typically at about 660 °C.

The growth of 100 – 300 nm thick MEAgrow InGaN samples was studied in the temperature range of 400 – 540 °C. The upper temperature limit was selected because MEAgrow grown InN was previously found to largely decompose and evaporate above a

growth temperature of 550 °C (see Chapter 5). A comparison is presented here for samples grown at 405, 450, and 540 °C to study the structural, optical and electrical properties as a function of the composition variation.

The growth at high temperatures results in a loss of the indium metal due to desorption and decomposition processes. For samples grown at 540 °C, the composition variation under different growth conditions was  $0.03 \leq x \leq 0.34$ . As discussed in the previous section, phase segregation was observed for samples with  $x > 0.2$  at this temperature. Only three samples of higher indium content resulted in single but still very broad XRD peaks.

In contrast, the InGaN grown at 405 °C had better crystalline quality for increased indium content, showing single peaks on the  $\omega$ -2 $\theta$  x-ray diffraction scans (Figure 6.9). At 460 °C an intermediate composition was achieved which varied between 15 and 30 % indium mole fraction. The results are presented in Figure 6.10, where the dependence of the InGaN composition is plotted against the energy bandgap which was obtained from the optical absorption edge. The error bars for the indium content were calculated from the full width at half maximum of the x-ray diffraction spectra. The error bars that spread below zero indium content are due to strain broadening of the diffraction spectra of the samples having composition close to GaN. In this graph the black squares represent the samples grown at 405 °C, the green triangles are the data for the samples grown at 540 °, the blue triangles show the data for 460 °C. The red dots represent the samples that showed the presence of free carrier absorption on the optical transmission spectra related to the presence of a Moss-Burstein effect. These samples are shown separately as they

would show an absorption edge above the expected optical bandgap. The phase segregated samples were removed from the data in Figure 6.10.

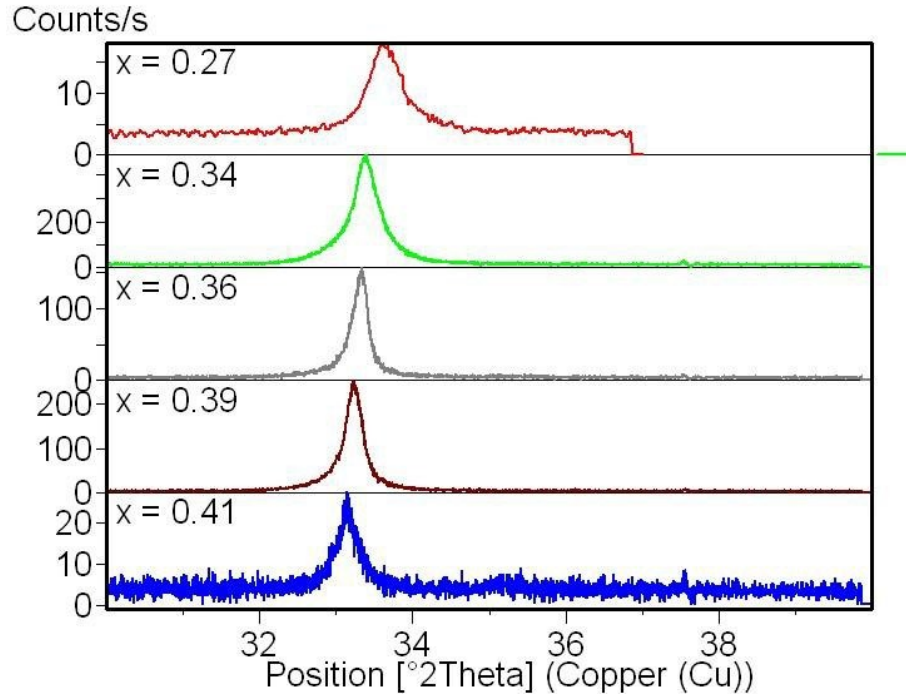


Figure 6.9 X-ray diffraction of InGaN grown at 405 °C on sapphire.

From 6.10 the temperature dependence for the indium incorporation is strongly evident. The crystal quality of the layers increased with increasing indium content of the films. An example of the trend for the XRD FWHM as a function of the composition is presented in Figure 6.11 for samples grown at 405 °C, where it can be seen that the quality drastically improves with increasing  $x$  but degrades when  $x$  reaches 0.4 probably due to strain. The connecting lines in Figure 6.11 are drawn only to show the trend. Degraded crystal quality was reported for InGaN samples with composition between 0.4 and 0.6 and was explained with the large strain arising with composition far from the two binaries [152]. A better crystal quality is expected at growth temperatures close to the decomposition temperature of InN, as was observed for MEAgrow InN grown under metal rich

conditions, but the indium incorporation efficiency in InGaN at this temperature was very low and a large phase separation was observed under similar growth conditions.

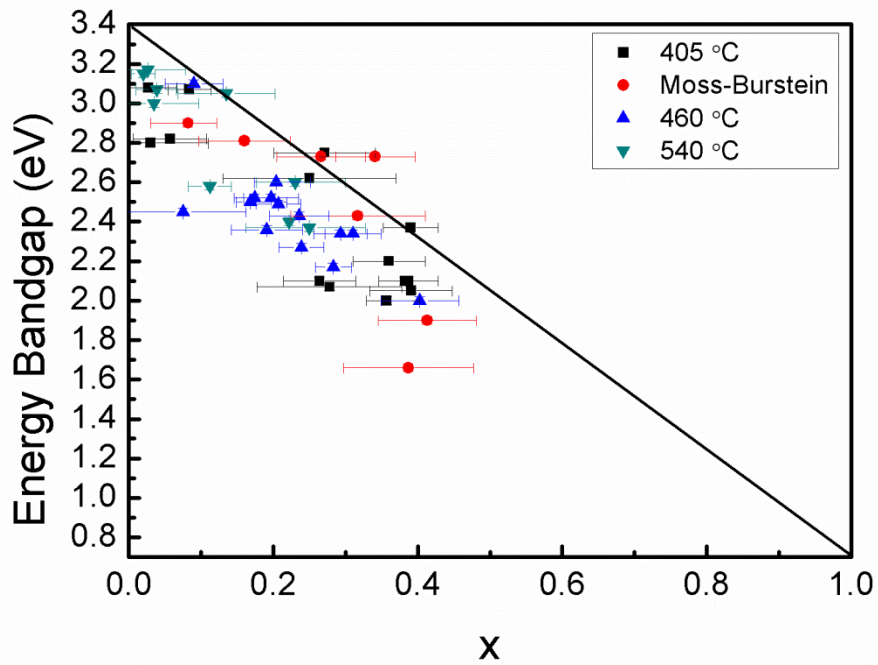


Figure 6.10 Temperature dependence of the InGaN composition as a function of the absorption edge for MEAglow InGaN.

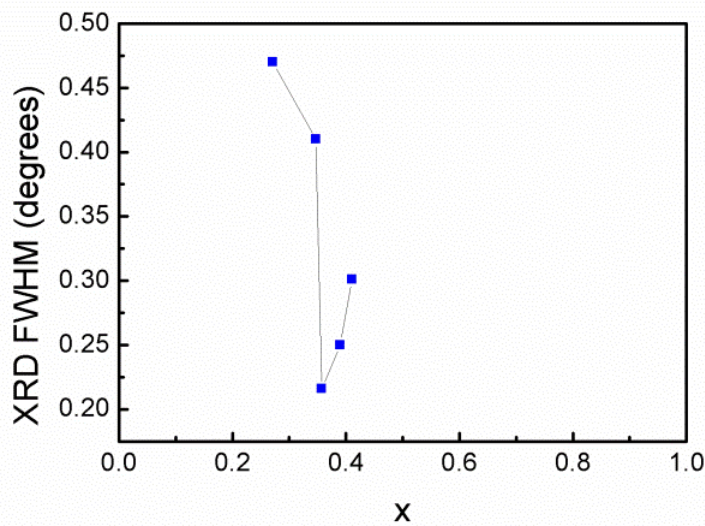


Figure 6.11 Variation of the FWHM with the composition for samples grown at 405 °C.

The variation of the energy bandgap of InGaN with the composition is very important parameter for designing device heterostructures and has been widely studied theoretically and experimentally [153] For pseudomorphically strained layers, the dependence of the energy bandgap on the indium composition is linear and is determined by the following relationship [136]:

$$E_g = E_{g0} + a\epsilon$$
(1)

where  $E_{g0}$  is the unstrained energy bandgap,  $a$  is deformation potential for the specific direction of the strain and  $\epsilon$  is the biaxial strain produced by the lattice mismatch.

The range of the studied films does not allow a direct determination of the bowing of the bandgap. The bandgap of relaxed unstrained layers follows Vegard's law and is typically expressed by the following relationship [154]:

$$E_g = b + (1-b)x$$
(2)

where  $b$  is the bowing parameter. Various values have been reported in the literature for the bowing parameter from experiments and theory [153]. However, the relaxation value of the lattice constant and the exact origin of the optical transitions have to be known in

order to accurately determine the dependence of the energy bandgap on the alloy composition. Usually the strain is avoided by growing thick films but this deteriorates the crystal quality and results in phase segregation. The range of the reported values for the bowing parameter is large. Values have been reported from 1 to 6 eV [154]. Possibility for the observed variation of the bowing parameter to be due to the lack of consideration for electron localization, was suggested by Alexandrov, based on theoretical studies [144].

The behaviour of the energy bandgap at higher gallium content is in agreement with the behaviour for the MEAgrow GaN samples discussed in Chapter 4. As can be seen from the plot, the energy bandgap for the samples with composition close to GaN decreases with decreased temperature, suggesting the presence of the same stoichiometry related defect which lowers the energy bandgap of the low temperature MEAgrow grown GaN. This is evident from the absorption coefficient squared plot, presented in Figure 6.12 for the samples which were examined with SIMS, presented in Section 4.1, Chapter 4 (referred to there as A and B). The sharp decrease in the energy bandgap with the composition suggests a large scatter on the composition, although it is hard to conclude due the large scatter in the experimental data and the lack of data for  $x > 0.5$ . The behaviour of the absorption edge in the indium rich side of the alloy is complex as the absorption edge for InN has previously been found to strongly depend on the growth temperature, which in turn determines the presence of various point defects and the stoichiometry of the layers [155]. A large bowing parameter for some of the samples is evident from Figure 6.10, perhaps related to metal-nitrogen stoichiometry issues.

## Absorption Coefficient Square data

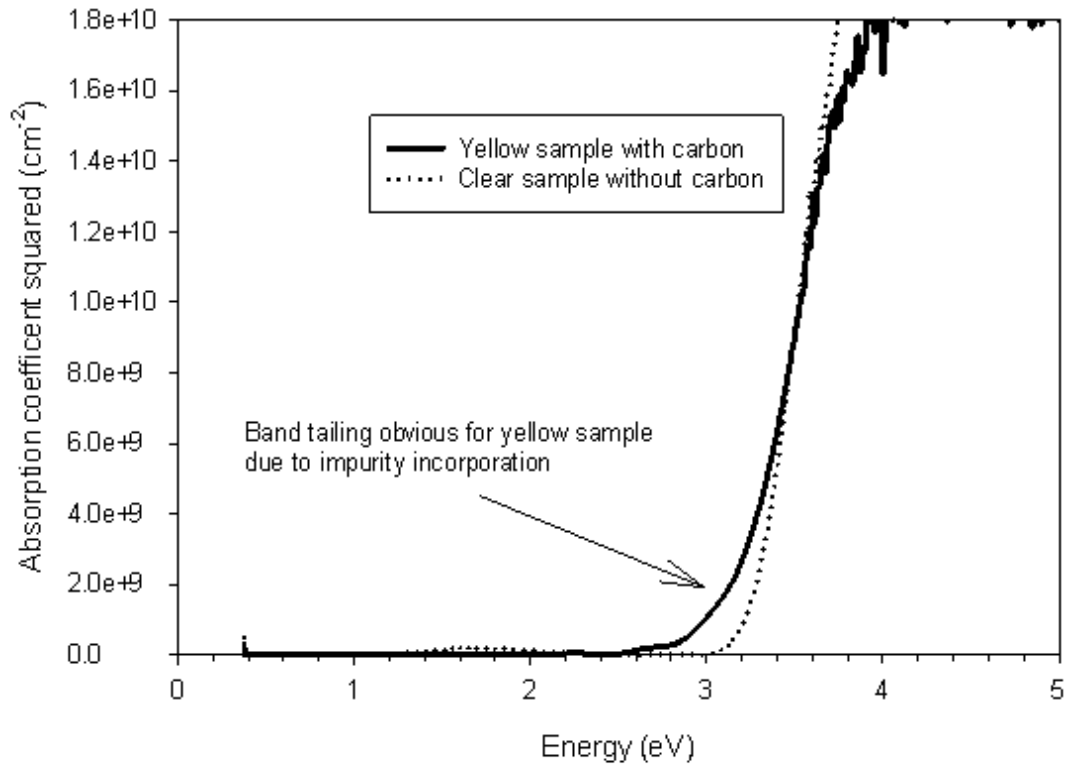


Figure 6.12 Absorption edge for MEAglow GaN sample containing high level of background carbon impurities (Sample A, Chapter 4), compared to stoichiometric MEAglow GaN (Sample B, Chapter 4).

Photoluminescence tests were performed with a HeCd laser but a spectrometer was unavailable to record the spectra. Visual observations were taken. The InGaN samples grown at 405 °C showed worse PL than the InGaN grown at 540 °C, having similar indium content in the film, and little or no photoluminescence was observed from these samples. This could possibly be related to point defects formed by excess metal in the layers, grown under metal rich conditions, which act as non-radiative centres. Similarly the Georgia group didn't observe any photoluminescence from their samples with similar

indium composition presented in ref. [142] grown under MME [156], this was regardless of the fact that those samples were grown on GaN buffer layers and had good crystal quality. It is well known that samples grown on GaN buffer layers exhibit much better optical properties than InGaN grown directly on sapphire [33]. Since some luminescence was observed in the MEAgrow samples, these samples indicate some device potential for layers grown directly on sapphire in combination with the advantage of smooth surfaces achieved with the metal rich growth. The poor optical properties for some of the samples is further confirmed by the lower than expected optical bandgap for samples grown with high gallium content, which is related to the absorption spectrum in Figure 6.12 and the related discussion provided above.

The growth at low temperatures affects the decomposition of the metalorganic precursors. Trimethylindium is found to decompose under pyrolysis at 340 °C [157], while trimethylgallium starts decomposing at 500 °C in a nitrogen ambient with complete decomposition occurring above 600 °C [71]. Growth at lower temperatures than 600 °C would result in certain degree of incorporation of carbon and CH in the film. Since the InGaN layers were grown below 600 °C in metal rich conditions it is suspected that a considerable amount of carbon has incorporated which affects the electrical properties. A high level of compensation of the inherent background electron concentration was observed particularly for the samples grown at 405 °C, i.e. they had a high resistivity. Carbon is known to act as deep acceptor in GaN [158] and is suggested as a possible cause for the semi-insulating character of the samples. A background electron concentration is typically present in both MOCVD grown GaN and InN [10]. The exact origin for the electron concentration is still unknown for InN. For GaN the most probable

background impurity dopant is oxygen, which acts as a shallow donor, but there are existing reports for hydrogen, and silicon. Native defects such as nitrogen vacancies have also been considered as a source of the background electron concentration for both GaN and InN. InN has a lot higher background electron concentration than GaN, for which, again, many possible sources are reported (see Chapter 4).

In Figure 6.13 the carrier concentration is presented as a function of the composition for samples grown at 540 °C and 405 °C. The electron concentration for samples grown at 405 °C didn't exceed  $5 \times 10^{19} / \text{cm}^3$  for InGaN having indium content between 30 and 40 %, while the carrier concentration for samples grown at 540 °C with indium content larger than 20 % increased drastically. This is believed to be due to the more efficient decomposition of the MO precursors at higher temperature releasing the gallium methyl species which are responsible for the high resistivity for the samples having low indium content. The mobilities of all InGaN samples, grown here on sapphire, as measured by Hall effect didn't exceed  $20 \text{ cm}^2/\text{V}\cdot\text{s}$ . Similar low mobilities have been observed for MOCVD samples grown on AlN/sapphire templates in the compositional range between  $0.2 \leq x \leq 0.8$  (see Figure 2 in ref [152] and have been attributed to scattering by dislocations, grain boundaries, and impurities.

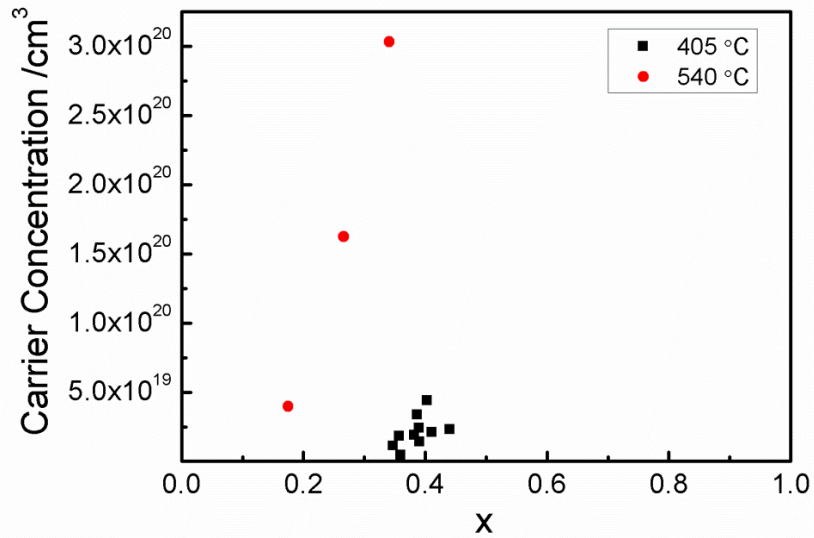


Figure 6.13 The variation of the carrier concentration for samples grown at 405 and 540 °C with composition.

#### 6.4 InGaN grown on GaN buffer layers as compared to the growth of InN on GaN under similar conditions

InGaN alloys with higher indium content have a larger lattice mismatch with sapphire and this results in increased defect densities caused by strain relaxation. The lattice mismatch between the sapphire and InN is about 29 % [159], while the mismatch with GaN is about 13.8 % [160]. Growth in similar metal rich conditions for InN and InGaN at 540 °C on commercially available GaN templates and their sister samples grown on sapphire was compared. SEM micrographs of the surfaces of InGaN and InN layers grown on top of the GaN templates are presented in Figure 6.14. The InGaN layer was grown on top of commercially available 2 μm p-GaN template and the InN layer was grown on top of 2 μm unintentionally doped GaN template. It is obvious that for InN samples the onset of crystal coalescence is present, whereas the surface of the InGaN sample has small closely packed crystallites, which indicates a polycrystalline structure. The polycrystallinity of

the InGaN samples grown at these temperatures probably relates to large defect densities introduced by the low miscibility of InN with GaN as the In atom has larger radius than the gallium atom which introduces additional strain in the layers. Another reason for the degraded quality can be roughening caused from the p-GaN template used for the InGaN samples, since p-GaN templates were observed to have larger AFM RMS surface roughness and poorer surface morphology than the unintentionally doped MOCVD GaN templates. In addition, polycrystalline growth was observed for MEAgrow homoepitaxial growth of GaN on commercially available 2  $\mu\text{m}$  thick GaN templates, so the inclusion of gallium may have affected the crystal quality, as well .

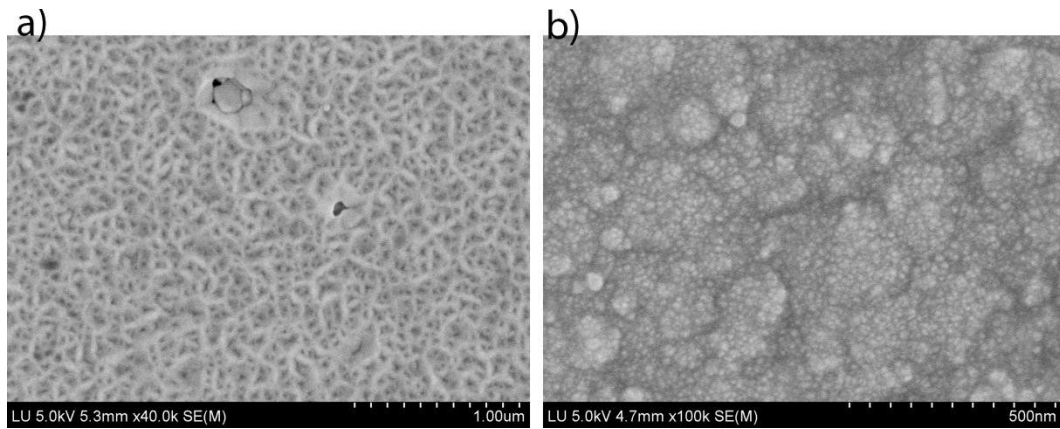


Figure 6.14 Surfaces of a) InN grown metal rich at 540 °C, and b) InGaN grown under similar conditions.

The metal rich growth of InGaN samples on sapphire substrates at 540 °C resulted in better uniformity than the growth of InN on sapphire under similar conditions. This can be evidenced by the cross-sectional images presented in Figure 6.15. The InN samples grown on sapphire were observed to fall apart after growth and peel off the substrate. It is suspected that too much indium causes large strain at the beginning of the growth process. On the other hand, the InGaN grown on sapphire at these temperatures resulted in bigger size crystals and better uniformity.

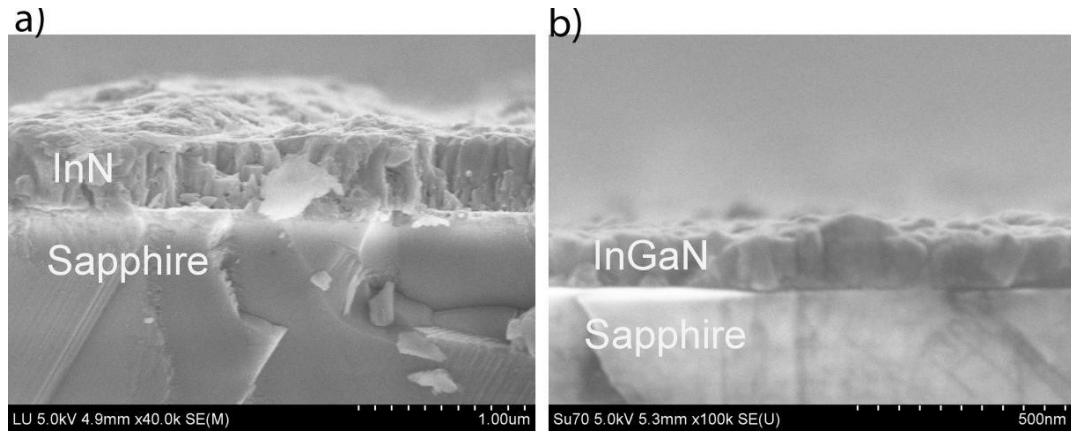


Figure 6.15 Cross-sectional images of a) metal rich InN grown on sapphire and b) InGaN grown on sapphire under similar conditions at 540 °C.

In conclusion, MEAgrow growth under MME technique was studied for InGaN samples grown on sapphire and GaN templates. The basic material properties and the various causes for occurrence of phase segregation were examined as related to the growth temperature. It was observed that the quality of the layers having composition  $0 \leq x \leq 0.3$  improves with increasing the indium incorporation for temperature range 405 – 540 °C and this was attributed to the poor decomposition of the gallium methyl groups from the metalorganic precursor in a combination with metal rich growth regime.

## Chapter 7. Conclusion

GaN, InN and InGaN films have been grown by a novel growth method called MEAgrow. The MEAgrow technique transfers the migration-enhanced epitaxy method into a plasma-based CVD environment. The technology is in its early development and could be further developed for commercial production of group III-nitrides, because it employs growth at relatively low temperatures and scalability for large area deposition. In addition, the use of hazardous materials, such as ammonia, commonly used in CVD systems, is avoided.

The GaN films have been grown directly on sapphire substrates at temperatures of approximately 660 °C in the metal rich regime. Different growth series were carried out to study the impact of the various growth parameters on the crystalline structure, optical and electrical properties of the films. The initial results for the GaN films grown at the above-stated temperatures resulted in very non-stoichiometric polycrystalline films. The elemental analysis showed the presence of high levels of background impurities incorporated in those early growths. The observed variation of the absorption edge towards low energies in these samples was attributed to the presence of defect centres, related to film stoichiometry, which was confirmed as an increase in the c lattice constant in the x-ray diffraction spectra with the increase of the metal flow. These samples showed high resistivity which is unusual for stoichiometric GaN films, as they normally show background electron concentration. The growth conditions were further optimized and more stoichiometric layers were achieved having absorption edge of 3.38 eV, which is in a good agreement with the reported value for wurtzite GaN.

The growth optimization process was related to studies of the MME (metal modulated epitaxy) method as it applies in a low-pressure CVD reactor. This required a study of the effect of the growth pressure on the semiconductor properties, as the MME method had only been used for MBE growth to this point, where there the growth occurs under vacuum. The pressure dependence was mapped to an established surface phase diagram [65] to achieve an intermediate regime, free of metal droplets though still in metal rich conditions. This is considered the optimal regime for low temperature GaN film growth. Calculations for the number of nitrogen collisions in the gas phase were performed to a first approximation. This allowed a greater understanding of processes and better control over the growth regime.

Thin InN films were grown in the metal rich regime on commercial GaN buffers, and Ga<sub>2</sub>O<sub>3</sub>, and high quality epitaxial layers were achieved on these substrates, whereas the samples grown directly on sapphire substrates under the same conditions remained largely polycrystalline. The samples grown directly on sapphire sometimes peeled off the substrate and this was attributed to a large strain induced from the incorporation of excess indium metal in the layers. The good crystal quality of the layers grown on Ga<sub>2</sub>O<sub>3</sub> was confirmed from x-ray rocking curves and SEM measurements. The achieved epitaxial growth on top of thin Ga<sub>2</sub>O<sub>3</sub> buffer layers indicates some potential for their use in InN film growth and device applications.

InN films grown at very low temperatures (<400 °C), suggesting nitrogen rich film stoichiometry [121], were annealed after growth to study the limiting process for the nitrogen removal in nitrogen rich InN. It was noted that for the defect removal in already

grown layers diffusion is the limiting process, which is less important during growth when the defect species are closer to the surface.

InGaN films were grown by MEA glow up to indium composition of  $x = 0.4$ . The indium surface segregation was shown to be successfully eliminated in the metal rich growth regime by flushing out the growth chamber with nitrogen gas. The growth temperature dependences of indium incorporation in this growth method were studied and phase segregation, commonly observed for this material, for samples grown directly on sapphire substrates was successfully reduced. The growth temperature dependence on the bowing parameter was studied and samples grown at different temperatures showed variations possibly related to their stoichiometry. The effect of the growth temperature on the crystalline quality of the films compared to InN films grown at similar temperatures was further examined for samples grown on various substrates. It was found that at temperatures closer to decomposition temperature of InN under metal rich conditions, the growth of InGaN on sapphire results in better crystalline quality than the growth of InN under the same conditions, while the growth on GaN templates resulted in better InN than InGaN grown on the same substrates.

## Appendix A XPS fitting procedure and results

The results from the XPS analysis of the GaN films are presented in this appendix. The curve fitting was performed using the CasaXPS software. The atomic sensitivity factors that were used were selected from the software libraries according to the Kratos Axis systems. The fitting was performed by selecting a common FWHM for all the components in all the high resolution spectra, as the samples were measured under the same conditions. The line shapes were product of 30% Lorentzian to Gaussian and the selected method for background subtraction was Shirley. The quantitative analysis was performed by calculating the atomic percentage for the Auger contribution in the N 1s high resolution spectra and subtracting the same percentage from the area of the nitrogen component on the survey spectra. The relatively high percentages obtained for the nitrogen peaks perhaps may be due to nitrogen surface species resulting from the termination of the surface with plasma, as was discussed in Chapter 4. The high percentages of carbon on the surface for some of the samples are related to the surface roughness of the films.

The data for the nitrogen and carbon high resolution spectra for the studied samples is shown in the two Figures below along with the report for the atomic percentages shown in Table A1.

Table A1 Relative atomic percentages calculated from the CasaXPS

Element	Sample 3	Sample 4	Sample 5A	Sample 5B	Sample 6
C 1s	29.33	27.12	66.9	62.67	39.65
O 1s	13.68	13.16	17.58	12.58	14.04
Ga 2p	18.35	17.41	1.88	6.22	14.96
N 1s	38.63	42.30	66.9	62.67	31.35
Al 2p			6.89		

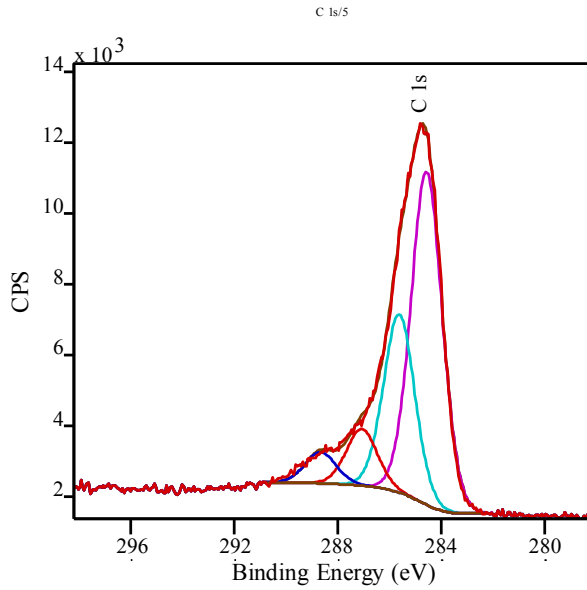


Figure A.1 High resolution XPS spectrum of C 1s core level for Sample 5A

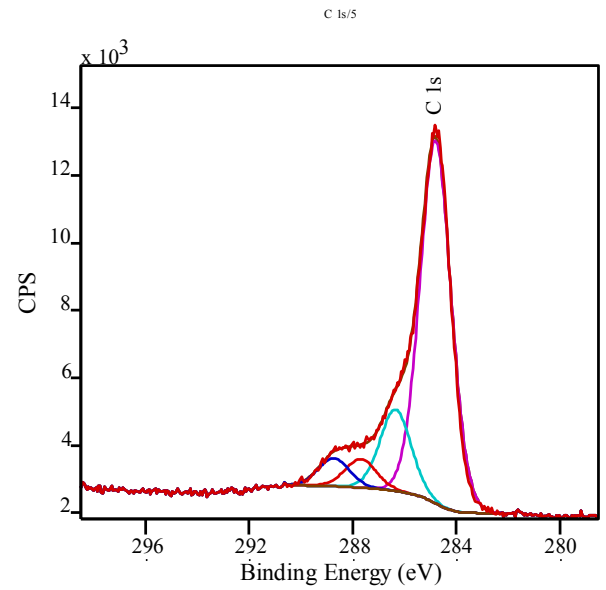


Figure A.2 High resolution XPS spectrum of C 1s core level for Sample 5B

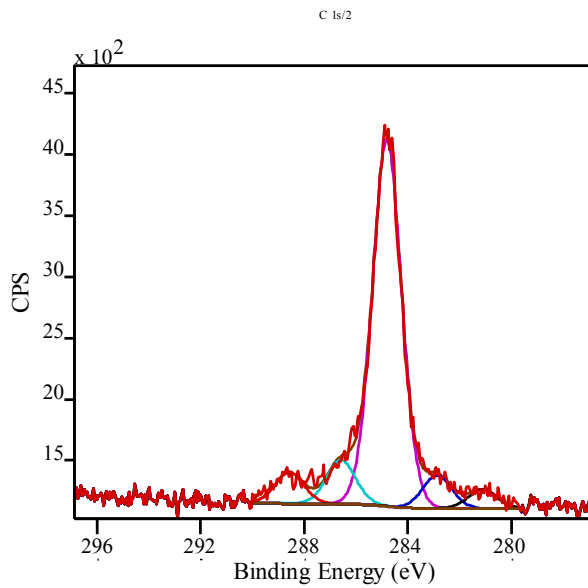


Figure A.3 High resolution XPS spectrum of C 1s core level for Sample 6

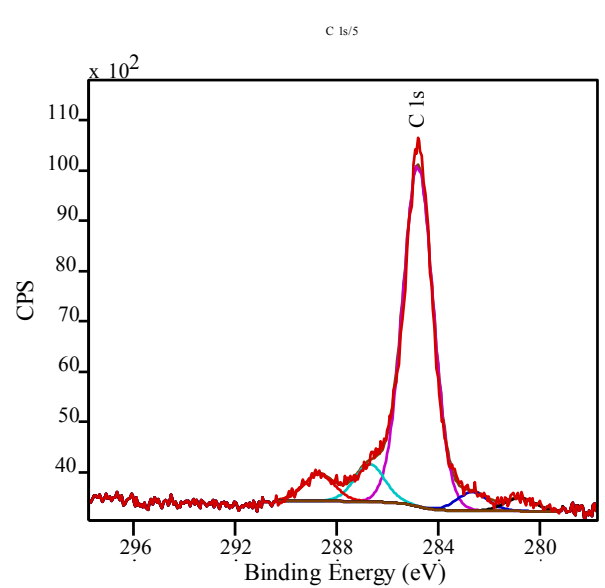


Figure A.4 High resolution XPS spectrum of C 1s core level for Sample 3

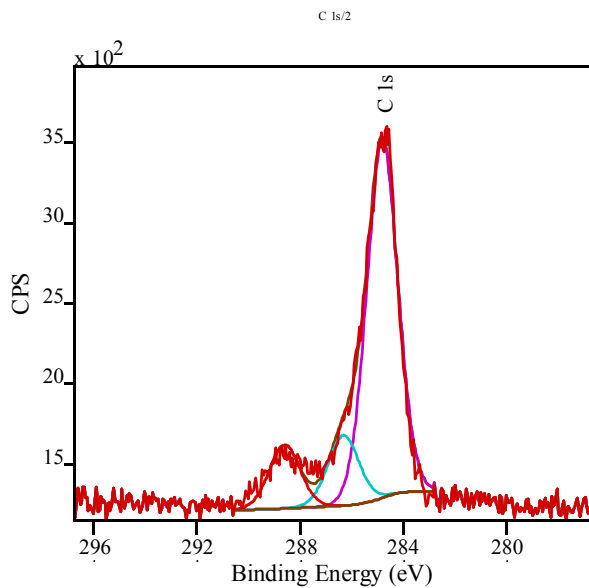


Figure A.5 High resolution XPS spectrum of C 1s core level for Sample 4

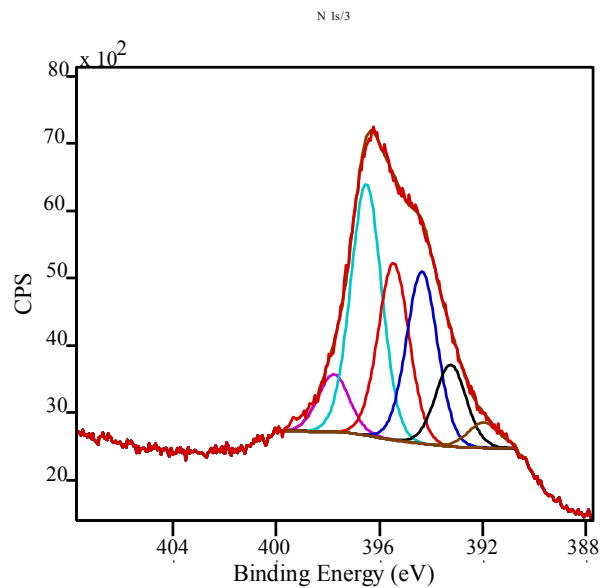


Figure A.6 High resolution XPS spectrum of N 1s core level for Sample 4

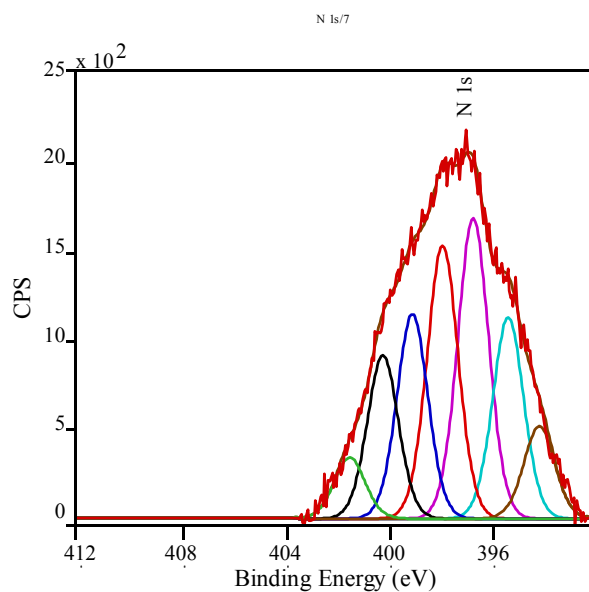


Figure A.7 High resolution XPS spectrum of N 1s core level for Sample 5A

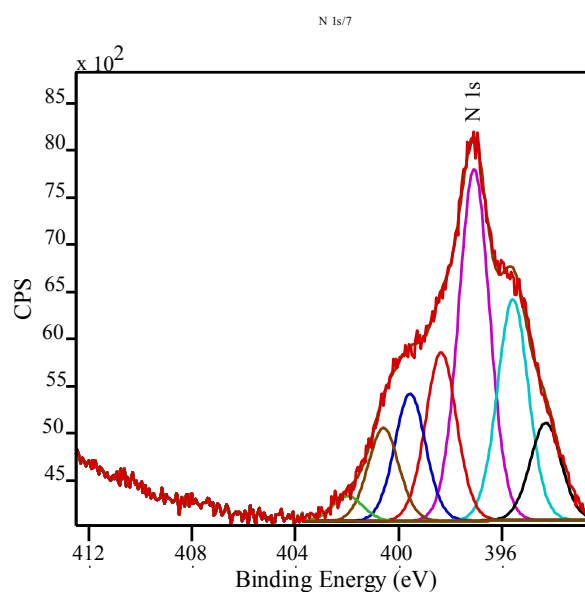


Figure A.8 High resolution XPS spectrum of N 1s core level for Sample 5B

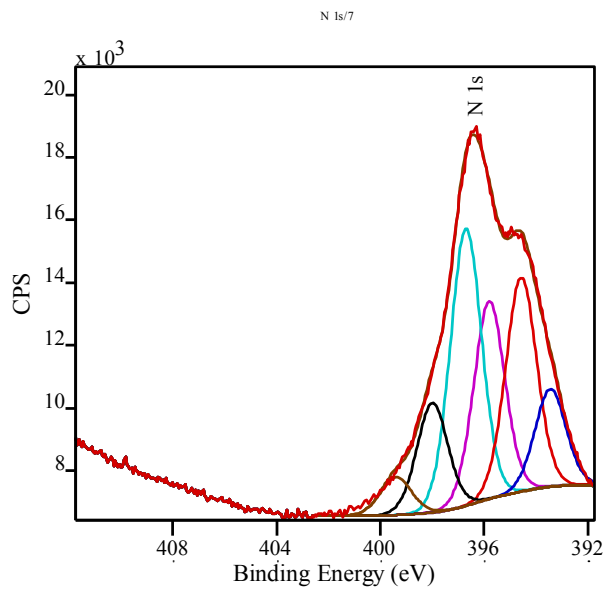


Figure A.9 High resolution XPS spectrum of N 1s core level for Sample 3

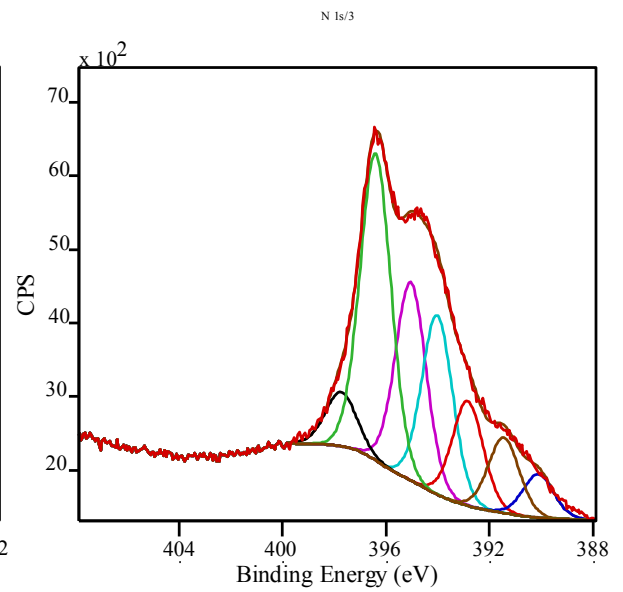


Figure A.10 High resolution XPS spectrum of N 1s core level for Sample 6

## REFERENCES

- [1] H. Yamashita, K. Fukui, S. Misawa, and S. Yoshida, "Optical properties of AlN epitaxial thin films in the vacuum ultraviolet region", *J. Appl. Phys.*, **50**, 896 (1979).
- [2] H. P. Maruska and J. J. Tietjen, "The preparation and properties of vapor-deposited single-crystalline GaN", *Appl. Phys. Lett.*, **15**, 327 (1969).
- [3] J. Wu, W. Walukiewicz, K. M. Yu, J. W. Ager III, E. E. Haller, H. Lu, W. J. Schaff, Y. Saito, Y. Nanishi, "Unusual properties of the fundamental band gap of InN", *Appl. Phys. Lett.*, **80**, 3967 (2002).
- [4] J. Wu, W. Walukiewicz, K. M. Yu, W. Shan, J. W. Ager III, E. E. Haller, H. Lu, W. J. Schaff, W. K. Metzger, S. Kurtz, "Superior radiation resistance of In<sub>1-x</sub>Ga<sub>x</sub>N alloys: Full solar-spectrum photovoltaic material system", *J. Appl. Phys.*, **94**, 6477 (2003).
- [5] H. Hamzaoui, A. S. Bouazzi, B. Rezig, "Theoretical possibility of In<sub>x</sub>Ga<sub>1-x</sub>N tandem PV structures" *Solar Energy Materials and Solar Cells*, **87**, 595 (2005).
- [6] E. Trybus, O. Jani, S. Burnham, I. Ferguson, C. Honsberg, M. Steiner, and W. A. Doolittle, "Characteristics of InGaN designed for photovoltaic applications", *Phys. Status Solidi C*, **5**, 1843 (2008).
- [7] E. Trybus, G. Namkoong, W. Henderson, S. Burnham, W. A. Doolittle, M. Cheung, and A. Cartwright, "InN: A material with photovoltaic promise and challenges", *J. Cryst. Growth*, **288**, 218 (2006).

- [8] M. Razeghi and A. Rogalski, "Semiconductor ultraviolet detectors", *J. Appl. Phys.*, **79**, 7433 (1996).
- [9] H. Morkoc, S. S. G. B. Gao, M. E. Lin, B. Sverdlov, and M. Burns, "Large-bandgap SiC, III-V nitride, and II-IV ZnSe-based semiconductor device technologies", *J. Appl. Phys.*, **76**, 1363 (1994).
- [10] S. Strite and H. Morkoc, "GaN, AlN, and InN: A review", *J. Vac. Sci. Technol. B*, **10**, 1237 (1992).
- [11] M. Khan, R. A. Skogman, J. M. V. Hove, D. T. Olson, and J. N. Kuznia, "Atomic layer epitaxy of GaN over sapphire using switched metalorganic chemical vapor deposition", *Appl. Phys. Lett.*, **60**, 1366 (1992).
- [12] B. Gelmont, K. Kim, and M. Shur, "Monte Carlo simulation of electron transport in gallium nitride", *J. Appl. Phys.*, **74**, 1818 (1993).
- [13] I. Akasaki and H. Amano, "Recent progress in crystal growth, conductivity control and light emitters in group III nitride semiconductors", *Tech. Dig. Int. Electron Devices Meet.*, **96**, 231 (1996).
- [14] F. Barkusky, C. Peth, A. Bayer, K. Mann, J. John, and P. E. Malinowski, "Radiation damage resistance of AlGaIn detectors for applications in the extreme ultraviolet spectral range", *Rev. Sci. Instrum.*, **80**, 093102 (2009).
- [15] S. Nakamura, "The role of structural imperfections in InGaIn-based blue light-emitting diodes and laser diodes", *Science*, **281**, 956 (1998).

- [16] H. Morkoc, "Handbook of nitride semiconductors and devices", pp. 1-2, WILEY-VCH Verlag GmbH & Co. KGaA (2008).
- [17] G. Koblmuller, R. Averbeck, H. Riechert, and P. Pongratz, "Direct observation of different equilibrium Ga adlayer coverages and their desorption kinetics on GaN (0001) and (000 $\bar{1}$ ) surfaces", *Phys Rev. B*, **69**,035325 (2004).
- [18] H. Morkoc, "Handbook of nitride semiconductors and devices", pp. 586-587, WILEY-VCH Verlag GmbH & Co. KGaA (2008).
- [19] M. Higashiwaki, T. Matsui, "Estimation of band gap energy of intrinsic InN from photoluminescence properties of undoped and Si-doped InN films grown by plasma-assisted molecular beam epitaxy", *J. Cryst. Growth*, **269**, 162 (2004).
- [20] V. Yu. Davydov, A. A. Klochikhin, V. V. Emtsev, S. V. Ivanov, F. Bechstedt, J. Furthmuller, H. Harima, A. V. Mudryi, J. Aderhold, O. Semchinova, J. Graul, "Absorption and emission of hexagonal InN. Evidence of narrow fundamental bandgap.", *Phys. Status Solidi B*, **229**, R1 (2002).
- [21] T. Inushima, V. V. Mamutin, V. A. Vekshin, S. V. Ivanov, T. Sakon, M. Motokawa, S. Ohoya, "Physical properties of InN with the bandgap energy of 1.1 eV", *J. Cryst. Growth*, **227**, 481 (2001).
- [22] M. Sparvoli, R. D. Mansano, J. F. D. Chubaci, "Study of indium nitride and indium oxynitride bandgaps", *Materials Research*, **16**, 850 (2013).

- [23] S. Shrestha, H. Timmers, K. S. A. Butcher, M. Wintrebert-Fouquet, “Accurate stoichiometric analysis of polycrystalline indium nitride films with elastic recoil detection”, *Current Appl. Phys.*, **4**, 237 (2004).
- [24] W. Paszkowicz, “X-ray powder diffraction data for indium nitride”, *Powder Diffraction*, **14**, 258 (1999).
- [25] S. N. Mohammad, H. Morkoc, “Progress and prospects of group III-nitride semiconductor”, *Prog. Quant. Electr.*, **20**, 361 (1996).
- [26] V. W. Chin, T. L. Tansley, and T. Osotchan, “Electron mobilities in gallium, indium, and aluminium nitrides”, *J. Appl. Phys.*, **75**, 7365 (1994).
- [27] C. H. Swartz, R. P. Tomkins, T. H. Myers, H. Lu, W. J. Schaff, “Demonstration of nearly non-degenerate electron conduction in InN grown by molecular beam epitaxy”, *Phys. Status Solidi C*, **2**, 2250 (2005).
- [28] O. Ambacher, “Growth and applications of group III-nitrides”, *J. Phys. D: Appl. Phys.*, **31**, 2653 (1998).
- [29] S. Nakamura, T. Mukai, M. Senoh, “In situ monitoring and Hall measurements of GaN grown with GaN buffer layers”, *J. Appl. Phys.*, **71**, 5543 (1992).
- [30] M. Tanaka, S. Nakahata, K. Sogabe, “Morphology and x-ray diffraction peak widths of aluminum nitride single crystals prepared by the sublimation method”, *J. J. Appl. Phys.*, **36**, L1062 (1997).
- [31] I. Akasaki, “Key inventions in the history of nitride-based blue LED and LD”, *J. Cryst. Growth*, **300**, 2 (2007).

- [32] S. Nakamura, T. Mukai, and M. Senoh, “Candela-class high brightness InGaN/AlGaIn double-heterostructure blue light-emitting diodes”, *Appl. Phys. Lett.*, **64**, 1687 (1994).
- [33] S. Nakamura, “InGaN-based blue/green/ LEDs and laser diodes”, *Advanced Materials*, **8**, 689 (1996).
- [34] S. Nakamura, “GaIn growth using GaIn buffer layer”, *J. J. Appl. Phys.*, **30**, L1705 (1991).
- [35] G. T. Thaler, D. D. Koleske, S. R. Lee, K. H. A. Bogart, M. H. Crawford, “Thermal stability of thin InGaIn films on GaIn”, *J. Cryst. Growth*, **312**, 1817 (2010).
- [36] H. Komaki, T. Nakamura, R. Katayama, K. Onabe, M. Ozeki, T. Ikari, “Growth of In-rich InGaIn films on sapphire via GaIn layer by RF-MBE
- [37] C. Adelman, R. Langer, G. Feuillet, and B. Daudin, “Indium incorporation during the growth of InGaIn by molecular-beam epitaxy studied by reflection high-energy electron diffraction intensity oscillations”, *Appl. Phys. Lett.*, **75**, 3518 (1999).
- [38] I. Ho and G. B. Stringfellow, “Solid phase immiscibility in GaInN”, *Appl. Phys. Lett.*, **69**, 2701 (1996).
- [39] T. Matsuoka, “Progress in nitride semiconductors from GaIn to InN – MOVPE growth and characteristics”, *Superlattices and Microstructures*, **37**, 19 (2005)
- [40] J. W. Ager III, R. E. Jones, D. M. Yamaguchi, K. M. Yu, W. Walukiewicz, S. X. Li, E. E. Haller, H. Lu, and W. J. Schaff, “P-type InN and In-rich InGaIn”, *Phys. Stat. Solidi B*, **244**, 1820 (2007).

- [41] K. S. A. Butcher and T. L. Tansley, “InN, latest development and a review of the band-gap controversy”, *Superlattices and Microstructures*, **38**, 1 (2005).
- [42] M. Oseki, K. Okubo, A. Kobayashi, J. Ohta, H. Fujioka, “Field-effect transistors based on cubic indium nitride”, *Scientific Reports*, **4**, 3951 (2014).
- [43] R. Brazis, R. Raguotis, Ph. Moreau, M. R. Siegrist, “Enhanced third-order nonlinearity in semiconductors giving rise to 1 THz radiation”, *Int. J. Inf. Millim. Waves*, **21**, 593 (2000).
- [44] E. Starikov, P. Shiktorov, V. Gruzinskis, L. Reggiani, L. Varani, J. C. Vaissiere, J. H. Zhao, “Monte Carlo simulation of terahertz generation in nitrides”, *J. Phys. Condens. Matter*, **13**, 7159 (2001).
- [45] E. Starikov, P. Shiktorov, V. Gruzinskis, L. Reggiani, L. Varani, J. C. Vaissiere, J. H. Zhao, “Monte Carlo calculations of THz generation in wide gap semiconductors”, *Physica B*, **314**, 171 (2002).
- [46] S. Nakamura, T. Mukai, and M. Senoh, “High brightness InGaN/AlGaN double-heterostructure blue-green-light-emitting-diodes”, *J. Appl. Phys.*, **76**, 8189 (1994)
- [47] S. Nakamura, M. Senoh, S. Nagahama, N. Iwasa, “Blue InGaN-based laser diodes with an emission wavelength of 450 nm”, *Appl. Phys. Lett.*, **76**, 22 (2000).
- [48] M. Asif Khan, J. N. Kuznia, A. R. Bhattarai, and D. T. Olson, “Metal semiconductor field effect transistor based on single crystal GaN”, *Appl. Phys. Lett.* **62**, 1786 (1993).
- [49] S. Keller, S. P. DenBaars, “Metalorganic chemical vapor deposition of group III-nitrides – a discussion of critical issues”, *J. Cryst. Growth*, **248**, 479 (2003).

- [50] H. Morkoc, "Handbook of nitride semiconductors and devices" Vol. 1, p. 396, WILEY-VCH Verlag GmbH & Co. KGaA (2008).
- [51] C. Yuan, T. Salagaj, A. Gurary, P. Zavadski, C. S. Chen, W. Kroll, R. A. Stall, Y. Li, M. Schurman, C. Y. Hwang, W. E. Mayo, Y. Lu, S. J. Pearton, S. Krishnankutty, and R. M. Kolbas, "High quality p-type GaN deposition on c-sapphire substrates in a multi wafer rotating-disk reactor", *J. Electrochem. Soc.*, **142**, L163 (1995).
- [52] S. Nakamura, Y. Harada, and M. Seno, "Novel metalorganic chemical vapor deposition system for GaN growth", *Appl. Phys. Lett.*, **58**, 2021 (1991).
- [53] Q. Fareed, R. Gaska, J. Mickevicius, G. Tamulaitis, M. S. Shur, M. Asif Khan, "Migration-enhanced metalorganic chemical vapor deposition of AlN/GaN/InN based heterostructures", *Semiconductor Device Research Symposium (2003) International p.* 402-403.
- [54] A. G. Bhuiyan, A. Hashimoto, and A. Yamamoto, "Indium nitride (InN): A review on growth, characterization and properties", *J. Appl. Phys.*, **94**, 2279 (2003).
- [55] H. Morkoc, "Handbook of nitride semiconductors and devices" Vol. 1, p. 416, WILEY-VCH Verlag GmbH & Co. KGaA (2008).
- [56] R. P. Parikh and R. A. Adomaitis, "An overview of gallium nitride growth chemistry and its effect on reactor design: Application to a planetary radial-flow CVD system", *J. Cryst. Growth*, **286**, 259 (2006).

- [57] R. L. Puurunen, "Surface chemistry of atomic layer deposition: A case study for the trimethylaluminium/water process", *J. Appl. Phys.*, **97**, 121301 (2005).
- [58] C. Ozgit-Akgun, E. Goldenberg, A. K. Okyay, and N. Biyikli, "Hollow-cathode plasma-assisted atomic layer deposition of crystalline AlN, GaN and  $\text{Al}_x\text{Ga}_{1-x}\text{N}$  thin films at low temperatures", *J. Mater. Chem. C*, **2**, 2123 (2014).
- [59] Y. Horikoshi, "Advanced epitaxial growth techniques: atomic layer epitaxy and migration-enhanced epitaxy", *J. Cryst. Growth* **201**, 150 (1998).
- [60] T. Yamaguchi, D. Muto, T. Araki, N. Maeda, and Y. Nanishi, "Novel InN growth method under In-rich condition on GaN/Al<sub>2</sub>O<sub>3</sub> (0001) templates", *Phys. Status Solidi C*, **6**, S360 (2009).
- [61] C. Poblenz, P. Waltereit, and J. S. Speck, "Uniformity and control of surface morphology during growth of GaN by molecular beam epitaxy", *J. Vac. Sci. Technol. B*, **23**, 1379 (2005).
- [62] N. Teraguchi, A. Suzuki, Y. Saito, T. Yamaguchi, T. Araki, Y. Nanishi, "Growth of AlN films on SiC substrates by RF-MBE and RF-MEE", *J. Cryst. Growth*, **230**, 392 (2001).
- [63] H. Lu, W. J. Schaff, J. Hwang, H. Wu, W. Yeo, A. Pharkya, L. F. Eastman, "Improvement on epitaxial grown of InN by migration-enhanced epitaxy", *Appl. Phys. Lett.* **77**, 2548 (2000).
- [64] S.D. Burnham PhD thesis, "Improved understanding and control of magnesium-doped gallium nitride by plasma assisted molecular beam epitaxy", p.93 (2007).

- [65] E. Trybus, W. A. Doolittle, M. Moseley, W. Henderson, D. Billingsley, G. Namkoong, and D. C. Look, "Extremely high hole concentrations in c-plane GaN" *Phys. Status Solidi C*, 6, S788 (2009).
- [66] K. S. A. Butcher, D. Alexandrov, P. Terziyska, V. Georgiev, and D. Georgieva, "Initial experiments in the migration-enhanced afterglow growth of gallium and indium nitride", *Phys. Status Solidi C*, 9, 1070 (2012).
- [67] K. S. A. Butcher, Patent application US 20100210067A1, "Migration and plasma-enhanced chemical vapor deposition", (2010).
- [68] K. S. A. Butcher, D. Alexandrov, P. Terziyska, V. Georgiev, D. Georgieva, and P. W. Binsted, "InN grown by migration-enhanced afterglow (MEAglow)", *Phys. Status Solidi A* 209, 41(2012).
- [69] K. S. A. Butcher, B. W. Kemp, I. B. Hristov, P. Terziyska, P. W. Binsted, and D. Alexandrov, "Gallium nitride film growth using a plasma based migration-enhanced afterglow chemical vapor deposition system", *J. J. Appl. Phys.* 51, 01AF02 (2012).
- [70] K. S. A. Butcher, Afifuddin, P. P.-T. Chen, and T. L. Tansley, "Studies of the plasma related oxygen contamination of gallium nitride grown by remote plasma enhanced chemical vapor deposition", *Phys. Status Solidi C*, 0, 156 (2002).
- [71] S. Shogen, Y. Matsumi, M. Kawasaki, and I. Toyoshima, "Pyrolytic and photolytic dissociation of trimethylgallium on Si and Au substrates", *J. Appl. Phys.*, 70, 462, (1991).
- [72] J. C. Vickerman, I. S. Gilmore, "Surface analysis, The principle techniques" WILEY, p. 58 (2009).

- [73] J. C. Vickerman, I. S. Gilmore, "Surface analysis, The principle techniques" WILEY, pp. 113- 256 (2009).
- [74] B. D. Cullity Elements of x-ray diffraction, Addison-Wesley Publishing Company, p. 84, 1956.
- [75] B. D. Cullity, Elements of x-ray diffraction, Addison-Wesley Publishing Company, p. 309, 1956.
- [76] M. Birkholz, "Thin film analysis by x-ray scattering", WILEY-VCH, p. 211 (2006).
- [77] K. S. A. Butcher, M. Wintrebert-Fouquet, P. P.-T. Chen, H. Timmers, S. K. Shrestha,"Detailed analysis of absorption data for indium nitride", Materials Science in Semiconductor Processing 6, 351 (2003).
- [78] P. P.-T. Chen, K. S. A. Butcher, E. M. Goldys, T. L. Tansley, K. E. Prince, "High energy Urbach characteristic observed for gallium nitride amorphous surface oxide", Thin Solid Films, 496, 342 (2006).
- [79] A. R. Hind, L. Chomette, "The determination of thin film thickness using reflectance spectroscopy", Application note, Agilent Technologies Inc, 2003, Publication Number SI-A-1205 (2011).
- [80] AFM Almanac – Imaging Modes, published in Agilent Technologies
- [81] L. J. Van der Pauw, "A method of measuring specific resistivity and Hall effect of discs of arbitrary shape", Phillips Res. Repts., 13,1, (1958).

[82] J. D. Mackenzie, C. R. Abernathy, J. D. Stewart, G. T. Muhr, "Growth of group III nitrides by chemical beam epitaxy", *J. Cryst. Growth*, 164, 143 (1996).

[83] J. F. Moulder, W. F. Stickle, P. E. Sobol, and K. D. Bomben, "Handbook of x-ray photoelectron spectroscopy", edited by J. Chastain, p. 22, Perkin Elmer Corporation, Physical electronics division, Eden Prairie (1992).

[84] S. Shogen, Y. Matsumi, M. Kawasaki, and Isamu Toyoshima, "Pyrolytic and photolytic dissociation of trimethylgallium on Si and Au substrates", *J. App. Phys.*, 70, 462 (1991).

[85] J. F. Moulder, W. F. Stickle, P. E. Sobol, and K. D. Bomben, "Handbook of x-ray photoelectron spectroscopy", edited by J. Chastain, p. 216, Perkin Elmer Corporation, Physical electronics division, Eden Prairie (1995).

[86] S. Kumar, K. S. A. Butcher, and T. L. Tansley, "X-ray photoelectron spectroscopy characterization of radio frequency reactively sputtered carbon nitride thin films", *J. Sci. Vac. Technol. A*, 14, 2687 (1996).

[87] V. D. Wheeler PhD thesis, "Structure and properties of epitaxial dielectrics on GaN", p 50 (2009).

[88] A. V. Blant, S. V. Novikov, T. S. Cheng, L. B. Flannery, I. Harrison, R. P. Campion, D. Korakakis, E. C. Larkins, Y. Kribes, C. T. Foxon, "Ga-metal inclusions in GaN grown on sapphire", *J. Cryst. Growth*, 203, 349 (1999).

- [89] J. A. Schreifels, J. E. Deffeyes, L. D. Neff, and J. M. White, "An x-ray photoelectron spectroscopic study of the adsorption of N<sub>2</sub>, NH<sub>3</sub>, NO, and N<sub>2</sub>O on dysprosium", *J. Electron Spectrosc. Relat. Phenom.*, 25, 191 (1982).
- [90] K. S. A. Butcher, A. J. Fernandes, P. P.-T. Chen, M. W. Fouquet, H. Timmers, S. K. Shrestha, H. Hirshy, R. M. Perks, B. F. Usher, "The nature of nitrogen related point defects in common forms of InN", *J. Appl. Phys.*, 101, 123702 (2007).
- [91] N. C. Saha and H. G. Tompkins, "Titanium nitride oxidation chemistry: An x-ray photoelectron spectroscopy study", *J. Appl. Phys.*, 72, 3072 (1992).
- [92] K. S. A. Butcher, H. Timmers, Affifudin, P. P.-T. Chen, T. D. M. Weijers, E. M. Goldys, T. L. Tansley, R. G. Elliman, J. A. Freitas, "Crystal size and oxygen segregation for polycrystalline GaN", *Jr, J. Appl. Phys.* 92, 3397 (2002) .
- [93] E. J. Tarsa, B. Heying, X. H. Wu, P. Fini, S. P. DenBaars, and J. S. Speck, "Homoepitaxial growth of GaN under Ga-stable and N-stable conditions by plasma-assisted molecular beam epitaxy", *J. Appl. Phys.*, 82, 5472 (1997).
- [94] H. Morkoc, "Handbook of nitride semiconductors and devices" Vol. 1, p. 456, WILEY-VCH Verlag GmbH & Co. KGaA (2008).
- [95] P. T. Terziyska, K. S. A. Butcher, D. Gogova, D. Alexandrov, P. Binsted, G. Wu, "InN nanopillars grown from In-rich conditions by migration-enhanced afterglow technique", *Materials Letters*, 106, 155 (2013).

- [96] K. S. A. Butcher, Afifuddin, P. P.-T. Chen, M. Godlewski, A. Szczerbakow, E. M. Goldys, T. L. Tansley, J. A. Freitas Jr., "Recrystallization prospects for freestanding low-temperature GaN grown on ZnO buffer layers", *J. Cryst. Growth*, 246, 237 (2002).
- [97] H. Lu, W. J. Schaff, J. Hwang, H. Wu, G. Koley, and L. F. Eastman, "Effect of an AlN buffer layer on the epitaxial growth of InN by molecular-beam epitaxy", *Appl. Phys. Lett.* 79, 1489 (2001).
- [98] M. Moseley, B. Gunning, J. Lowder, W. A. Doolittle, G. Namkoong, "Structural and electrical characterization of InN, InGaN, and p-InGaN grown by metal modulated epitaxy", *J. Vac. Sci. Technol. B* 31, 03C104 (2013).
- [99] R. Gergova, K. S. A. Butcher, P. W. Binsted, D. Gogova, "Initial results for epitaxial growth of InN on gallium oxide and improved Migration-Enhanced Afterglow Epitaxy growth on gallium nitride", *J. Vac. Sci. Technol. B* 32, 031207 (2014).
- [100] A. Yamamoto, M. Tsujino, M. Ohkubo, A. Hashimoto "Nitridation effects of substrate surface on the metalorganic chemical vapor deposition growth of InN on Si and  $\alpha$ -Al<sub>2</sub>O<sub>3</sub> substrates", *J. Cryst. Growth*. 137, 415 (1994).
- [101] P. P.-T. Chen, K. S. A. Butcher, M. Wintrebert-Fouquet, R. Wuhler, M. R. Phillips, K. E. Prince, H. Timmers, S. K. Shrestha, B. F. Usher, "Apparent band-gap shift in InN films grown by remote-plasma-enhanced CVD", *J. Cryst. Growth* 288, 241 (1998).
- [102] H. Wang, Y. Huang, Q. Sun, J. Chen, J. J. Zhu, L. L. Wang, Y. T. Wang, H. Yang, M. F. Wu, Y. H. Qu, D. S. Jiang, "Depth dependence of structural quality in InN grown by metalorganic chemical vapor deposition", *Materials Letters* 61, 516 (2007).

- [103] C. H. Swartz, R. P. Tompkins, N. C. Giles, T. H. Myers, H. Lu, W. J. Schaff, L. F. Estman, "Investigation of multiple carrier effects in InN epilayers using variable magnetic field Hall measurements", *J. Cryst. Growth* 269, 29 (2004).
- [104] M. Higashiwaki, K. Sasaki, A. Kuramata, T. Masui, S. Yamakoshi, "Development of gallium oxide power devices", *Phys. Status Solidi A* 211, 21 (2014).
- [105] G. Wagner, M. Baldini, D. Gogova, M. Schmidbauer, R. Schewski, M. Albrecht, Z. Galazka, D. Klimm, R. Fornari, "Homoepitaxial growth of  $\beta$ -Ga<sub>2</sub>O<sub>3</sub> layers by metal-organic vapor phase epitaxy", *Phys. Status Solidi A* 211, 27 (2014).
- [106] D.-W. Choi, K.-B. Chung, J.-S. Park, "Low temperature Ga<sub>2</sub>O<sub>3</sub> atomic layer deposition using gallium tri-isopropoxide and water", *Thin Solid Films* 546, 31 (2013).
- [107] P. W. Binsted, K. S. A. Butcher, D. Alexandrov, P. Terziyska, D. Georgieva, R. Gergova, V. Georgiev, "InN on GaN heterostructures growth by migration-enhanced epitaxial afterglow (MEAglow)", *Mat. Res. Soc. Symp. Proc.*, 1396, 255 (2012).
- [108] P. P.-T. Chen, K. S. A. Butcher, M. Wintrebert-Fouquet, and K. E. Prince, "Properties of InN grown by remote plasma enhanced chemical vapor deposition", *IEEE COMMAD-04*, 85 (2005).
- [109] F. Tuomisto, A. Pelli, K. M. Yu, W. Walukiewicz, and W. J. Schaff, "Compensating point defects in 4He<sup>+</sup>-irradiated InN", *Phys. Rev. B* 75, 193201 (2007).
- [110] T. V. Shubina, S. V. Ivanov, V. N. Jmerik, M. M. Glazov, A. P. Kalvarskii, M. G. Tkachmann, A. VAsson, J. Leymarie, A. Kavokin, H. Amano, I. Akasaki, K. S. A.

Butcher, Q. Guo, B. Monemar, and P. S. Kop'ev, "Optical properties of InN with stoichiometry violation and indium clustering", *Phys. Status Solidi A* **202**, 377 (2005).

[111] F. Reurings, F. Tuomisto, C. S. Gallinat, G. Koblmuller, and J. S. Speck, "In vacancies in InN grown by plasma-assisted molecular beam epitaxy", *Appl. Phys. Lett.* **97**, 251907 (2010).

[112] K. P. Biju, and M. K. Jain, "Annealing studies on InN thin films grown by modified activated reactive evaporation", *J. Cryst. Growth* **311**, 2542 (2009).

[113] D. H. Kuo, and C. H. Shih, "Native defects and their effects on properties of sputtered InN films", *Appl. Phys. Lett.* **93**, 164105 (2008).

[114] H. Shinoda, and N. Mutsukura, "Structural and optical properties of InN films prepared by radio frequency magnetron sputtering", *Thin Solid Films* **503**, 8 (2006).

[115] N. C. Zoita, and C. E. A. Grigorescu, "Influence of growth temperature and deposition duration on the structure surface morphology and optical properties of InN/YSZ (100)", *Appl. Surf. Sci.* **258**, 6046 (2012).

[116] D. W. Jenkins, J. D. Dow, "Electronic structures and doping of InN,  $\text{In}_x\text{Ga}_{1-x}\text{N}$ , and  $\text{In}_x\text{Al}_{1-x}\text{N}$ ", *Phys. Rev. B* **39**, 3317 (1989).

[117] C. Stampfl, and C. G. Van de Walle, "Native defects and impurities in InN: First-principles studies using the local-density approximation and self-interaction and relaxation-corrected pseudopotentials", *Phys. Rev. B* **61**, R7846 (2000).

- [118] X. M. Duan, and C. Stampfl, “Vacancies and interstitials in indium nitride: Vacancy clustering and molecular bondlike formation from first principles”, *Phys. Rev. B*, **79**, 174202 (2009).
- [119] T. L. Tansley, and C. P. Foley, “Infrared absorption in indium nitride”, *J. Appl. Phys* **60**, 2092 (1986).
- [120] M. Sato, “Carrier density of epitaxial InN grown by plasma-assisted metalorganic chemical vapor deposition”, *Jpn. J. Appl. Phys.*, **36**, L658 (1997).
- [121] K. S. A. Butcher, P. P.-T. Chen, and J. E. Downes, “Low activation energy for the removal of excess nitrogen in nitrogen rich indium nitride”, *Appl. Phys. Lett.*, **100**, 011913 (2012).
- [122] P. P.-T. Chen PhD dissertation, “RPECVD Growth and Characterization of polycrystalline InN thin films”, p. 151 (2011).
- [123] K. S. A. Butcher, H. Hirshy, R. M. Perks, M. Wintrebert-Fouquet, P. P.-T. Chen, “Stoichiometry effects and the Moss-Burstein effect for InN”, *Phys. Status Solidi A*, **203**, 66 (2006).
- [124] K. S. A. Butcher, M. Wintrebert-Fouquet, P. P.-T. Chen, K. E. Prince, H. Timmers, S. K. Shrestha, T. V. Shubina, S. V. Ivanov, R. Wuhrer, M. R. Phillips, and B. Monemar, “Non-stoichiometry and non-homogeneity in InN”, *Phys. Status Solidi C*, **7**, 2263 (2005).
- [125] M. R. Ranade, F. Tessier, A. Navrotsky, R. Marchand, “Calorimetric determination of the enthalpy of formation of InN and comparison with AlN and GaN”, *J. Matter. Res.*, **16**, 2824 (2001).

- [126] W. L. Chen, R. L. Gunshor, J. Han, K. Higashimine, N. Otsuka, “Growth of InN by MBE”, *MRS Internet J. Nitride Semicond. Res.*, **5S1**, W3.30 (2000).
- [127] Motlan, E. M. Goldys, T. L. Tansley, “Optical and electrical properties of InN grown by radio-frequency reactive sputtering”, *J. Cryst. Growth.*, **241**, 165 (2002).
- [128] L. C. Chen, W. H. Lan, R. M. Lin, H. T. Shen, H. C. Chen, “Optical properties of In<sub>2</sub>O<sub>3</sub> oxidized from InN deposited by reactive magnetron sputtering”, *Appl. Surf. Sci.*, **252**, 8438 (2006).
- [129] S. Kumar, L. Mo, Motlan, T. L. Tansley, “Elemental composition of reactively sputtered indium nitride thin films”, *Jpn. J. Appl. Phys.*, **35**, 2261 (1996).
- [130] Y.-K. Kuo, T.-H. Wang, and J.-Y. Chang, “Advantages of blue InGaN light-emitting diodes with InGaN-AlGaIn-InGaIn barriers”, *Appl. Phys. Lett.*, **100**, 031112 (2012).
- [131] G. Verzellesi, D. Saguatti, M. Meneghini, F. Bertazzi, M. Goano, G. Meneghesso, and E. Zanoni, “Efficiency droop in InGaIn/GaIn blue light-emitting diodes: Physical mechanisms and remedies”, *J. Appl. Phys.*, **114**, 071101 (2013).
- [132] O. Jani, C. Honsberg, A. Asghar, D. Nicol, I. Ferguson, A. Doolittle, and S. Kurtz, 31st IEEE Photovoltaic Specialists Conf. pp 37–42, (2005).
- [135] A. G. Bhuiyan, K. Sugita, A. Hashimoto, and A. Yamamoto, “InGaIn Solar Cells: Present State of the Art and Important Challenges”, *IEEE J. Photovolt.* **3** 276–93, (2012).
- [134] S. Nakamura, M. Senoh, and T. Mukai, “High power InGaIn/GaIn double heterostructures violet light-emitting diodes”, *Appl. Phys. Lett.*, **62**, 2390, (1993).

- [135] S. Nakamura, "III-V nitride-based light-emitting diodes", *Diamond and Related Materials*, **5**, 496, (1996).
- [136] G. B. Stringfellow, "Microstructures produced during the epitaxial growth of InGaN alloys", *J. Cryst. Growth*, **312**, 735, (2010).
- [137] N. Yoshimoto, T. Matsuoka, T. Sasaki, A. Katsui, "Photoluminescence of InGaN films grown at high temperature by metalorganic vapor phase epitaxy", *Appl. Phys. Lett.*, **59**, 2251, (1991).
- [138] O. Brandt, P. Waltereit, U. Jahn, S. Dhar, and K. H. Ploog, "Impact of In bulk and surface segregation on the optical properties of (In,Ga)N/GaN multiple quantum wells", *Phys. Status Solidi A*, **192**, 5, (2002).
- [139] S. Yu. Karpov, and Yu. N. Makarov, "Surface segregation in group III-nitride MBE", *Phys. Status Solidi A*, **188**, 611, (2001).
- [140] S. Choi, T.-H. Kim, S. Wolter, A. Brown, H. O. Everitt, M. Losurdo, and G. Bruno, "Indium adlayer kinetics on the gallium nitride (0001) surface: Monitoring indium segregation and precursor-mediated absorption", *Phys. Rev. B*, **77**, 115435, (2008).
- [141] H. Chen, R. M. Feenstra, J. E. Northrup, T. Zywietz, J. Neugebauer, D. W. Greve, "Surface structures and growth kinetics of InGaN (0001) grown by molecular beam epitaxy", *J. Vac. Sci. Technol. B*, **18**, 2284, (2000).
- [142] M. Moseley, J. Lowder, D. Billingsley, and W. A. Doolittle, "Control of surface adatom kinetics for the growth of high-indium content InGaN throughout the miscibility gap", *Appl. Phys. Lett.*, **97**, 191902, (2010).
- [143] K. S. A. Butcher, T. L. Tansley, *Superlattices and Microstructures*, **38**, 1, (2005).
- [Dimiter] D. Alexandrov, "Excitons of the structure in wurtzite  $\text{In}_x\text{Ga}_{1-x}\text{N}$  and their properties", *J. Cryst. Growth*, **246**, 325 (2002).

- [144] D. Alexandrov, "Excitons of the structure in  $\text{In}_x\text{Ga}_{1-x}\text{N}$  and their properties", J. Cryst. Growth 246, 325(2002)
- [145] D. Alexandrov, private communication.
- [146] Y. Kawaguchi, M. Shimizu, K. Hiramatsu, N. Sawaki, "The composition pulling effect in InGaN growth on GaN and AlGaIn epitaxial layers grown by MOVPE", Mat. Res. Symp. Proc., **449**, 89 (1997).
- [147] H. Teisseyre, P. Perlin, T. Suski, I. Grzegory, S. Porowski, J. Jun, A. Pietraszko, T. D. Moustakas, "Temperature dependence of the energy gap in GaN bulk single crystals and epitaxial layer" J. Appl. Phys. **76**, 2429 (1994).
- [148] S. R. Meher, A. Subrahmanyam, M. K. Jain, "Composition-dependent structural, optical, and electrical properties of  $\text{In}_x\text{Ga}_{1-x}\text{N}$  ( $0.5 \leq x \leq 0.93$ ) thin films grown by modified activated reactive evaporation", J. Mater. Sci. **48**, 1196 (2013).
- [149] S. R. Meher, K. P. Biju, M. K. Jain, "Growth of indium rich nanocrystalline indium gallium nitride thin films by modified activated reactive evaporation", International Journal of Nanoscience **10**, 141 (2011).
- [150] K. Kushi, H. Sasamoto, D. Sugihara, S. Nakamura, A. Kikuchi, K. Kishino, "High speed growth of device quality GaN and InGaIn by RF-MBE", Mater. Sci. Eng. B, **59**, 65, (1999).
- [151] B. N. Pantha, J. Li, J. Y. Lin, H. X. Jiang, "Single phase  $\text{In}_x\text{Ga}_{1-x}\text{N}$  ( $0.25 \leq x \leq 0.63$ ) synthesized by metal organic chemical vapor deposition", Appl. Phys. Lett., **93**, 182107, (2008).
- [152] B. N. Pantha, H. Wang, N. Khan, J. Y. Lin, and H. X. Jiang, "Origin of background electron concentration in  $\text{In}_x\text{Ga}_{1-x}\text{N}$  alloys", Phys. Rev. B, **84**, 075327, (2011).

- [153] Z. Dridi, B. Bouhafs, and P. Ruterana, "First principle investigation of lattice constants and bowing parameters in wurtzite  $\text{Al}_x\text{Ga}_{1-x}\text{N}$ ,  $\text{In}_x\text{Ga}_{1-x}\text{N}$ , and  $\text{In}_x\text{Al}_{1-x}\text{N}$  alloys", *Semicond. Sci. Technol.*, **18**, 850, (2003).
- [154] F. K. Yam, Z. Hassan, "InGaN: An overview of growth kinetics, physical properties and emission mechanisms", *Superlattices and Microstructures*, **43**, 1, (2008). [155] P. P.-T. Chen, K. S. A. Butcher, M. Wintrebert-Fouquet, R. Wuhler, M. R. Phillips, K. E. Prince, H. Timmers, S. K. Shrestha, B. F. Usher, "Apparent band-gap shift in InN films grown by remote-plasma-enhanced CVD", *J. Cryst. Growth*, **288**, 241, (2006).
- [156] A. M. Fischer, Y. O. Wei, F. A. Ponce, M. Moseley, B. Gunning, A. Doolittle, "Highly luminescent, high-indium-content InGaN film with uniform composition and full misfit-strain relaxation", *Appl. Phys. Lett.* **103**, 131101 (2013)
- [157] G. A. Hebner, K. P. Killeen, "Measurement of atomic indium during metalorganic chemical vapor deposition", *J. Appl. Phys.*, **67**, 1598, (1990).
- [158] J. L. Lyons, A. Janotti, and C. G. Van de Walle, "Effects of carbon on the electrical and optical properties of InN, GaN, and AlN", *Phys. Rev. B*, **89**, 035204, (2014).
- [159] C. J. Lu, L. A. Bendersky, H. Lu, W. Schaff, "Threading dislocations in epitaxial InN thin films grown on (0001) sapphire with a GaN buffer layer", *Appl. Phys. Lett.*, **83**, 2817, (2003).
- [160] S. J. Pearton, *GaN and Related Materials*, Volume 2, p. 73, (1997).